

Applications of Nanomaterials in Multifunctional Polymer Nanocomposites

Guest Editors: Bin Li, Nazanin Emami, Guan Gong, and Weidong Song





Applications of Nanomaterials in Multifunctional Polymer Nanocomposites

Applications of Nanomaterials in Multifunctional Polymer Nanocomposites

Guest Editors: Bin Li, Nazanin Emami, Guan Gong,
and Weidong Song



Copyright © 2016 Hindawi Publishing Corporation. All rights reserved.

This is a special issue published in "Journal of Nanomaterials." All articles are open access articles distributed under the Creative Commons Attribution License, which permits unrestricted use, distribution, and reproduction in any medium, provided the original work is properly cited.

Editorial Board

- Domenico Acierno, Italy
Katerina Aifantis, USA
Nageh K. Allam, USA
Margarida Amaral, Portugal
Martin Andersson, Sweden
Raul Arenal, Spain
Ilaria Armentano, Italy
Vincenzo Baglio, Italy
Lavinia Balan, France
Thierry Baron, France
Andrew R. Barron, USA
Reza Bayati, USA
Hongbin Bei, USA
Daniel Bellet, France
Stefano Bellucci, Italy
E. Bergamaschi, Italy
Samuel Bernard, France
D. Bhattacharyya, New Zealand
Sergio Bietti, Italy
Giovanni Bongiovanni, Italy
T. Borca-Tasciuc, USA
M. Bououdina, Bahrain
Torsten Brezesinski, Germany
C. Jeffrey Brinker, USA
Christian Brosseau, France
Philippe Caroff, Australia
Victor M. Castaño, Mexico
Albano Cavaleiro, Portugal
Bhanu P. S. Chauhan, USA
Shafiqul Chowdhury, USA
Jin-Ho Choy, Republic of Korea
Kwang-Leong Choy, UK
Yu-Lun Chueh, Taiwan
E. Comini, Italy
Giuseppe Compagnini, Italy
David Cornu, France
M. A. Correa-Duarte, Spain
P. Davide Cozzoli, Italy
Shadi A. Dayeh, USA
Luca Deseri, USA
Yong Ding, USA
Philippe Dubois, Belgium
Zehra Durmus, Turkey
Joydeep Dutta, Oman
Ali Eftekhari, USA
- Jeffrey Elam, USA
Samy El-Shall, USA
Ovidiu Ersen, France
Claude Estournès, France
Andrea Falqui, KSA
Matteo Ferroni, Italy
Elena J. Foster, USA
Ilaria Fratoddi, Italy
Alan Fuchs, USA
Miguel A. Garcia, Spain
Siddhartha Ghosh, Singapore
P. K. Giri, India
Russell E. Gorga, USA
Jihua Gou, USA
Jean M. Greneche, France
Smrati Gupta, Germany
K. Hamad-Schifferli, USA
Simo-Pekka Hannula, Finland
Michael Harris, USA
Yasuhiko Hayashi, Japan
F. Hernandez-Ramirez, Spain
Michael Z. Hu, USA
Nay Ming Huang, Malaysia
Shaoming Huang, China
David Hui, USA
Zafar Iqbal, USA
Balachandran Jeyadevan, Japan
Xin Jiang, Germany
Rakesh Joshi, Australia
Jeong-won Kang, Republic of Korea
Hassan Karimi-Maleh, Iran
Antonios Kelarakis, UK
Alireza Khataee, Iran
Ali Khorsand Zak, Iran
Philippe Knauth, France
Ralph Krupke, Germany
Christian Kübel, Germany
Prashant Kumar, UK
Michele Laus, Italy
Eric Le Bourhis, France
Jun Li, Singapore
Meiyong Liao, Japan
Shijun Liao, China
Silvia Licoccia, Italy
Wei Lin, USA
- Nathan C. Lindquist, USA
Zainovia Lockman, Malaysia
Nico Lovergine, Italy
Jim Low, Australia
Jue Lu, USA
Ed Ma, USA
Laura M. Maestro, Spain
Gaurav Mago, USA
Muhamamd A. Malik, UK
Devanesan Mangalaraj, India
Sanjay R. Mathur, Germany
Tony McNally, UK
Yogendra Mishra, Germany
Paulo C. Morais, Brazil
Paul Munroe, Australia
Jae-Min Myoung, Republic of Korea
Rajesh R. Naik, USA
Albert Nasibulin, Russia
Toshiaki Natsuki, Japan
Koichi Niihara, Japan
Natalia Noginova, USA
Sherine Obare, USA
Won-Chun Oh, Republic of Korea
Atsuto Okamoto, Japan
Abdelwahab Omri, Canada
Ungyu Paik, Republic of Korea
P. Pallavicini, Italy
Edward A. Payzant, USA
A. Pegoretti, Italy
Ton Peijs, UK
O. Perales-Pérez, Puerto Rico
Jorge Pérez-Juste, Spain
Alexey P. Popov, Finland
Philip D. Rack, USA
Peter Reiss, France
Orlando Rojas, USA
Marco Rossi, Italy
Ilker S. Bayer, Italy
Cengiz S. Ozkan, USA
Sudipta Seal, USA
Shu Seki, Japan
Vladimir Šepelák, Germany
Huaiyu Shao, Japan
Prashant Sharma, USA
Donglu Shi, USA



Bhanu P. Singh, India
Surinder Singh, USA
V. Sivakov, Germany
Ashok Sood, USA
Adolfo Speghini, Italy
Marinella Striccoli, Italy
Xuping Sun, KSA
A. K. Sundramoorthy, USA
Angelo Taglietti, Italy
Bo Tan, Canada
Leander Tapfer, Italy
Valeri P. Tolstoy, Russia

Muhammet S. Toprak, Sweden
Ramon Torrecillas, Spain
Achim Trampert, Germany
Takuya Tsuzuki, Australia
Tamer Uyar, Turkey
Bala Vaidhyanathan, UK
Luca Valentini, Italy
Rajender S. Varma, USA
Ester Vazquez, Spain
A. Villaverde, Spain
Ajayan Vinu, Australia
Ruibing Wang, Macau

Shiren Wang, USA
Yong Wang, USA
Magnus Willander, Sweden
Ping Xiao, UK
Zhi Li Xiao, USA
Yangchuan Xing, USA
Doron Yadlovker, Israel
Yoke K. Yap, USA
Kui Yu, Canada
William Yu, USA
Michele Zappalorto, Italy
Renyun Zhang, Sweden

Contents

Applications of Nanomaterials in Multifunctional Polymer Nanocomposites

Bin Li, Nazanin Emami, Guan Gong, and Weidong Song

Volume 2016, Article ID 5790194, 1 page

Characteristics and Properties of TiO₂/EP-PU Composite

Chen Yufei, Li Zhichao, Tan Junyan, Zhang Qingyu, and Han Yang

Volume 2015, Article ID 167150, 7 pages

Synthesis and Characterization of Zinc Borate Nanowhiskers and Their Inflaming Retarding Effect in Polystyrene

Pingqiang Gao and Yan Zhang

Volume 2015, Article ID 925060, 6 pages

Epoxy Resin Composite Bilayers with Triple-Shape Memory Effect

Xixi Li, Yaofeng Zhu, Yubing Dong, Meng Liu, Qingqing Ni, and Yaqin Fu

Volume 2015, Article ID 475316, 8 pages

Green Synthesis, Characterization, and Antibacterial Activity of Silver/Polystyrene Nanocomposite

Manal A. Awad, W. K. Mekhamer, Nada M. Merghani, Awatif A. Hendi, Khalid M. O. Ortashi,

Fatimah Al-Abbas, and Nada E. Eisa

Volume 2015, Article ID 943821, 6 pages

Composite Scaffolds Based on Silver Nanoparticles for Biomedical Applications

Jenel Marian Patrascu, Ioan Avram Nedelcu, Maria Sonmez, Denisa Ficai, Anton Ficai,

Bogdan Stefan Vasile, Camelia Ungureanu, Madalina Georgiana Albu, Bogdan Andor,

Ecaterina Andronescu, and Laura Cristina Rusu

Volume 2015, Article ID 587989, 8 pages

Ultradrawing and Ultimate Tenacity Properties of Ultrahigh Molecular Weight Polyethylene Composite Fibers Filled with Nanosilica Particles with Varying Specific Surface Areas

Jen-taut Yeh, Chuen-Kai Wang, Lu-Kai Huang, Chih-Chen Tsai, and Wei-Yu Lai

Volume 2015, Article ID 146718, 16 pages

Editorial

Applications of Nanomaterials in Multifunctional Polymer Nanocomposites

Bin Li,¹ Nazanin Emami,² Guan Gong,³ and Weidong Song⁴

¹Department of Mechanical Engineering, Wichita State University, 1845 Fairmount Street, Wichita, KS 67260-0133, USA

²Department of Engineering Science and Mathematics, Luleå University of Technology, 971 87 Luleå, Sweden

³Swerea SICOMP AB, P.O. Box 271, 941 26 Piteå, Sweden

⁴PD Materials, Boeing Commercial Airplanes, Seattle, WA 98124, USA

Correspondence should be addressed to Bin Li; bin.li@wichita.edu

Received 20 December 2015; Accepted 21 December 2015

Copyright © 2016 Bin Li et al. This is an open access article distributed under the Creative Commons Attribution License, which permits unrestricted use, distribution, and reproduction in any medium, provided the original work is properly cited.

Incorporating functional nanomaterials into polymers is an effective approach to achieving enhanced performances and creating new functionalities for the lightweight material applications. The resulting polymer nanocomposites benefit from advantages of both polymer matrix and nanoreinforcement phase. For the past few decades, polymer nanocomposite has become one of the most attractive research areas drawing magnificent attentions from both academia and industry. It is designed by taking advantage of specific characteristics of components, with intention for broad applications such as lightweight structures and energy and biomedical applications. Selected original research articles were compiled in this special issue reviewing some recent achievement on multifunctional polymer nanocomposites.

P. Gao and Y. Zhang synthesized zinc borate nanowhisker and used it to fabricate fire retardant polystyrene nanocomposites. Meanwhile, the nanowhisker also improved the surface quality (smoothness) and mechanical properties. A similar scenario was also reported by C. Yufei et al. in surface modified titanium dioxide/polyurethane modified epoxy. The improved interfacial interactions and dispersion because of the surfactant on TiO₂ led to the enhancement of both properties.

Y. Fu et al. dispersed nanosilica in epoxy to strengthen the shape memory effects of polymer matrix. The resulting nanocomposites showed both improved triple shape memory effects and the shape fixity properties. Nanocomposite fiber composed of ultrahigh molecular weight polyethylene and

surface modified nanosilica was fabricated by J. Yeh and coworkers. Processing procedures were optimized leading to enhanced mechanical properties which can be attributed to the good dispersion and surface modification of nanosilica.

M. A. Awad et al. reported antibacterial activities of nanosilver modified polystyrene nanocomposites with intended application for food packaging, which can be used against Gram-negative bacteria *Escherichia coli*, *Klebsiella pneumoniae*, and *Salmonella* and Gram-positive bacteria *Staphylococcus aureus*. M. G. Albu et al. prepared nanocomposite scaffolds with nanosilver for biomedical applications, which showed a clear antiseptic activity against *Escherichia coli*.

These original research articles focused on critical issues in polymer nanocomposites including nanoparticle resources and dispersion, polymer/nanoparticle interface, and processing of nanocomposites and their effects on the structural properties and functionalities. We hope to enrich our readers and researchers with the state-of-the-art research by compiling these articles in this special issue.

Bin Li
Nazanin Emami
Guan Gong
Weidong Song

Research Article

Characteristics and Properties of TiO₂/EP-PU Composite

Chen Yufei,^{1,2} Li Zhichao,² Tan Junyan,² Zhang Qingyu,² and Han Yang²

¹Key Laboratory of Engineering Dielectrics and Its Application, Harbin University of Science and Technology, Ministry of Education, Harbin 150080, China

²The College of Material Science & Engineering, Harbin University Science & Technology, Linyuan Road No. 4, Xiangfang District, Harbin, Heilongjiang, China

Correspondence should be addressed to Chen Yufei; chenyufei@hrbust.edu.cn

Received 10 August 2015; Revised 20 November 2015; Accepted 25 November 2015

Academic Editor: Bin Li

Copyright © 2015 Chen Yufei et al. This is an open access article distributed under the Creative Commons Attribution License, which permits unrestricted use, distribution, and reproduction in any medium, provided the original work is properly cited.

Polymer matrix of EP-PU was prepared by epoxy resin which was polyurethane toughened, and TCA201 coupling agent was used to modify nano-TiO₂, and TiO₂/EP-PU composite was synthesized using EP, PU, and TCA201-TiO₂. The results of SEM and TEM showed that the surface of TiO₂ was coated with TCA201 coupling agent through the bonding between the hydroxyl of nano-TiO₂ particle and coupling agent molecules, the interaction would be beneficial to improve compatibility of inorganic and organic phases, and TCA201-TiO₂ would disperse evenly in composite and improve performance of composite materials. The mechanical properties, thermal stability, dielectric properties, and breakdown strength of composites were investigated by electronic tensile machine, TGA, dielectric spectrum, and CS2674C type voltage tester. The results indicated that appropriate amount of TCA201-TiO₂ could improve mechanical properties, the shear strength of 3 wt%-TiO₂/EP-PU reached the maximum value at 27.14 MPa, its thermal decomposition temperature was 397.82°C, enhanced 17.48°C more than that of EP-PU matrix, and its dielectric constant (ϵ) and dielectric loss ($\tan \delta$) showed 4.27 and 0.02, respectively. Its breakdown field strength was 14 kV/mm. Its performance met the requirement of dielectric materials.

1. Introduction

Epoxy resin (EP) is one of the most commonly used thermosetting materials in high voltage apparatus as insulation due to its excellent mechanical, electrical properties and chemical stability. EP adhesive with excellent bonding properties is widely used in aerospace, military, electronics, construction, and many other fields [1]. The main purpose of this study was that polyurethane (PU) and inorganic nano-TiO₂ are used to increase the mechanical strength, thermal stability and improve the dielectric properties of the composites. Polyurethane (PU) was used as the flexibilizer that reinforced toughness of epoxy resin, and the interfacial theory of composite materials was used to analyze the relationship between material structure and properties of composite [2]. Owing to the poor compatibility existing between the interface of organic matrix and inorganic fillers, some efforts were usually necessary to enhance the compatibility between the inorganic fillers and the polymer matrix during the preparation of hybrid materials [3]. To achieve this

objective, TCA201 coupling agent is usually used to modify nano-TiO₂ and the surface of modified nano-TiO₂ has existed in active group (-OH, -COOH), so the relations of inorganic fillers and polymer matrix should be improved and were beneficial to interfacial energy in the formation of hybrid composites. In this research, EP-PU has existed in "island" structure; this structure is in favor of composites toughness [4]. At the same time, the performance of the composites was tested through mechanical properties, thermal stability, and dielectric properties.

2. Experimental

2.1. Materials. The chemicals used in this study such as epoxy resin (EP-51) and methyl tetrahydrophthalic anhydride (MTHPA) were industrial products and were purchased from the Lanxing New Chemical Materials Co., Ltd., China. Polyurethane (PU) was industrial products and obtained from Jindao Material Sci & Tech Co., Ltd., Beijing, China, and imidazole was industrial products and purchased from Jinyan

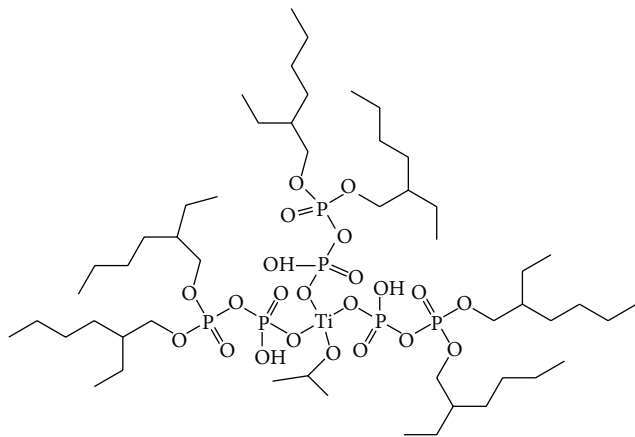


FIGURE 1: The chemical structure of TCA201.

Trading Co., Ltd., Guangzhou, China. The density of TiO_2 is 0.42 g/cm^3 , the size of particle is 25 nm, and the melting point of TiO_2 is $1830\text{--}1850^\circ\text{C}$ and comes from Yicheng Jingrui New Material Co., Ltd., China. Coupling agent of titanate (TCA201) is brought from Jing Tianwei Chemical Co., Ltd., Nanjing, China. The structure of isopropyl tri(dioctylpyrophosphate) titanate (TCA201) was shown in Figure 1.

2.2. Modification of Nano- TiO_2 . TCA201 was dissolving in 17 mL toluene and its concentration was 2.6%. TiO_2 was added into above solution until the system was evenly about 2–4 hours under 80°C and then was leached. TiO_2 was 10 g. Washing modified TiO_2 solution with toluene 3–4 times and leaching, put it into the oven and let it dry for 10 hours at 80°C and get TCA201- TiO_2 .

2.3. Preparation of Material Composites. Technological process of composite materials was described as follows. A certain percentage of the EP-51 and PU were mixed at 80°C until they dispersed evenly, and a certain amount of TCA201- TiO_2 powder was added into above systems. The solution was dissolving in the ultrasonic condition, cooled to 50°C , and added into MTHPA and imidazole until the system was mixed completely. The mixture was degassed to remove air bubbles and pour into preprepared molds for molding in the oven and curing temperature was 80°C for 2 hr, 120°C , 150°C , and 180°C for 1 hr, respectively.

2.4. Measurements. The FT-IR spectra, which were used to study the chemical structure of the polymer matrix, were performed with EQUINOX-55 Fourier transform spectrometer (GER), in the $400\text{--}4000 \text{ cm}^{-1}$ range, and 5 scans were averaged for each spectrum. And it could be seen that there existed the characteristic absorption peaks of material.

The fracture structures of samples were examined on the Hitachi S-4300 scanning electron microscope (SEM, Japan). Samples were deposited on a sample holder with adhesive carbon foil and sputtered with gold.

The state of aggregation and morphology of nano- TiO_2 were tested by JEM-2100 transmission electron microscopy

(TEM, Japan), the test temperature was 18°C , and voltage was 120 kV.

The FT-IR spectra, which were used to study the chemical structure of the polymer matrix, were performed with EQUINOX-55 Fourier transform spectrometer (GER), in the $400\text{--}4000 \text{ cm}^{-1}$ range, and it could be seen that there existed the characteristic absorption peaks of material.

The shearing strength of the composite materials was determined with CSS-44300 electronic testing machine (China) according to a native standard of GB/T7124-1986. Standard tensile shear experiments were performed at room temperature, under a speed of 5 mm/min. For each sample, at least five measurements were made, and the average value was taken.

Thermogravimetric analysis (TGA), which could not only investigate the state of a material and the process of decomposition but also provide useful information about the thermal stability of material, was recorded on a Perkin-Elmer 6 series thermal analysis system. Samples were heated from 200°C to 800°C at a heating rate of $20^\circ\text{C}/\text{min}$ in a nitrogen atmosphere and weight of sample was about 10–15 mg.

The dielectric constant (ϵ) and dielectric loss ($\tan \delta$) of composite materials were measured with Agilent-4294A precision impedance analyzer (Japan) in the frequency of 50 Hz at room temperature according to GB/T 1409-89.

CS2674C pressure tester (GER) was used to test the breakdown strength of the composites.

3. Results and Discussions

3.1. FT-IR Spectral Analysis. FT-IR spectra of nano- TiO_2 were presented in Figure 2. The curves ((a) and (b)) were designated as unmodified TiO_2 and TCA201- TiO_2 , respectively.

It was seen from Figure 2 that the curve of TCA201- TiO_2 was different from the curve of unmodified TiO_2 . The peak of curve (b) at 2864 cm^{-1} and 2934 cm^{-1} was due to the stretching vibration of C–H in TCA201, and the peak at 1039 cm^{-1} was the characteristic peak of P–O–P [5]. The peak at 1724 cm^{-1} was the absorption band of P–O–H, and the peak at 1464 cm^{-1} was the characteristic peak of P=O. It could prove that TCA201 has been grafted to the surface of TiO_2 . Chemical interaction of $-\text{OCH}(\text{CH}_3)_2$ in titanate coupling TCA201 and polar group for nano- TiO_2 would form organic active monolayer, and this could help to facilitate two-phase action between inorganic and organic phase and improve the properties of composites.

3.2. Analysis of SEM Patterns. SEM was always used to analyze microscopic structure of the composite material, and the microstructures of nano- TiO_2 and composites were shown in Figure 3.

Figures 3(a) and 3(b) show microtopography of unmodified nano- TiO_2 , TCA201- TiO_2 and Figures 3(c) and 3(d) show fracture SEM picture of 3 wt% (TCA201- TiO_2)/EP-PU and 7 wt% (TCA201- TiO_2)/EP-PU, respectively. Unmodified TiO_2 particles had an irregular shape but uniformly disperse. TiO_2 particles were of nanoscale and the white area was relatively big, so the clusters phenomenon existed (see Figure 4(a)). The surface that TCA201- TiO_2 was uniformly

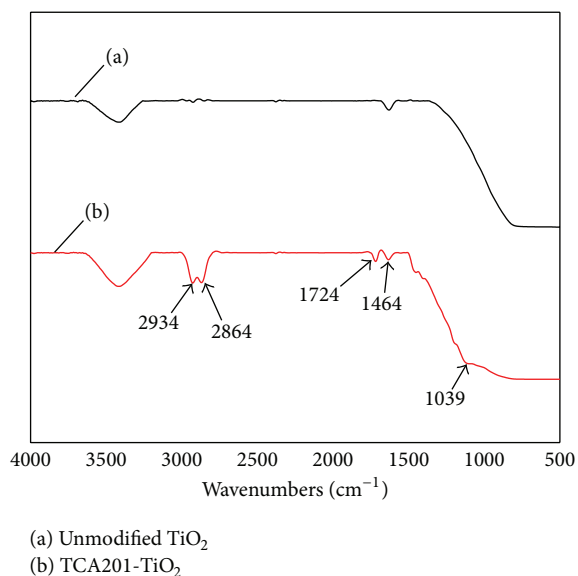


FIGURE 2: FT-IR spectra of nano-TiO₂.

coated by coupling agent had relatively flat, smooth, and small spherical particles, and white areas were more dispersed in Figure 3(b). Agglomeration tendency was weakened; the interaction between the particles was reduced and uniformly dispersed. It also indicated that particle size decreased, and the surface area increased [6–8]. Figures 3(c) and 3(d) showed that the relatively flat area was EP matrix, which was continuous phase, and PU molecule had uniformly formed “island structure” in EP matrix. Inorganic particles were dispersing phase and were evenly dispersed in EP-PU matrix, and the interaction of inorganic components and PU matrix was very strong and they were distributed in PU matrix “island structure” in Figures 3(c) and 3(d), and the inorganic particles in “island structure” were of nanoscale. Nanoparticles had a larger surface area [9], and the surface of modified nanoparticles had active groups and compatibility with organic phase, to promote the mutual penetration of the two-phase interface; the interpenetration could help to improve the mechanical properties.

3.3. Analysis of TEM Patterns. The morphology of TCA201-TiO₂ was investigated by TEM in order to observe the effect of modification and verified the result of FT-IR in Figure 4.

Figure 4 shows the TEM images of TCA201-TiO₂; Figures 4(a) and 4(b) were magnified to 4×10^4 times and 8×10^4 times, respectively. In the picture, it would be seen that TCA201-TiO₂ dispersed evenly, and the particle size was in the nanosized and modified nano-TiO₂ uniformly connected at both ends of the coupling agent, which demonstrated that the interaction of the active group in TiO₂ molecular and the active group in TCA201 was existing. The interaction could be intermolecular cross-linking, inhibit reuniting of TiO₂, and improve the interaction of two phases, titanate made the epoxy resin and nano-TiO₂ surface connection strengthen, and organic functional groups of titanate and the epoxy resin should produce chemical bonding, so the nano-TiO₂ well dispersed in an epoxy resin and TCA201-TiO₂

could greatly improve and enhance their overall performance. Transmission electron microscopy showed how nano-TiO₂ and TCA201 connected.

3.4. Mechanical Properties. The diagram of the shear strength of TCA201-TiO₂/EP-PU composite was shown in Figure 5.

With the increase of TCA201-TiO₂ filler, the shear strength of the composites gradually increased and then declined. The shear strength of 3 wt% TCA201-TiO₂/EP-PU composite was the maximum value for 27.14 MPa. The content of TCA201-TiO₂ was more than 3 wt% and the shear strength of composite materials decreased but still was higher than that of pure polymer matrix EP-PU.

Generally, TCA201-TiO₂ modified by coupling agent was not simply physically blending with polymer matrix. TCA201-TiO₂ and polymer matrix could form chemical bonds through coupling agent; as the surface of TCA201-TiO₂ has existed in much active groups, these groups could improve fracture energy and adhesive strength of the composites [10]. The structure of coupling agent had two kinds of functional group; one was active group and the other was nonactive group; this structure would play the role of a bridge which associated with the nano-TiO₂ and the epoxy matrix. The function enhanced the interfacial adhesion and consumed more energy; thereby mechanical properties of composites were improved [11].

Nanoparticles had large specific surface area and high superficial energy; it could help to improve interactions with epoxy matrix. When the content of nanoparticles was more excessive, the interactions of inorganic particles could be enhanced, but the interactions of polymer matrix and inorganic component would weaken, and inorganic TiO₂ would be reunion and the dispersion of two phases would be much difficult. The phenomenon of agglomeration occurred, which resulted in stress concentration point, and the mechanical properties of composites could decrease, but the shear strength of composites was still higher than that of pure epoxy resin matrix [12, 13].

3.5. Heat Resistance Properties. Thermal degradation behaviors of composites were evaluated by thermogravimetric analysis (TGA). TGA curves of composite materials were shown in Figure 6. The results demonstrated that T_d of TCA201-TiO₂/EP-PU was firstly increased and then decreased with the increase of TCA201-TiO₂ doping. When the amount of TCA201-TiO₂ was 3 wt%, T_d that reached up to 397.82°C was higher 17.48°C than that of pure materials. The main reasons were that firstly heat resistance of inorganic TCA201-TiO₂ was stronger and to increase its content in the polymer matrix was bound to enhancing the heat resistance of the composite. Secondly, there were active groups in the TCA201-TiO₂ particles structure, and there were a large number of hydroxyl groups in the organic phase; the two kinds of active groups could have contact with cross-linking agent and exist in strong interactions. This interaction enhanced fracture energy of composites and became beneficial to the heat resistant properties of composite [14, 15]. Thirdly, inorganic TCA201-TiO₂ particles possessed a large specific surface area, contacting area of organic matrix was larger,

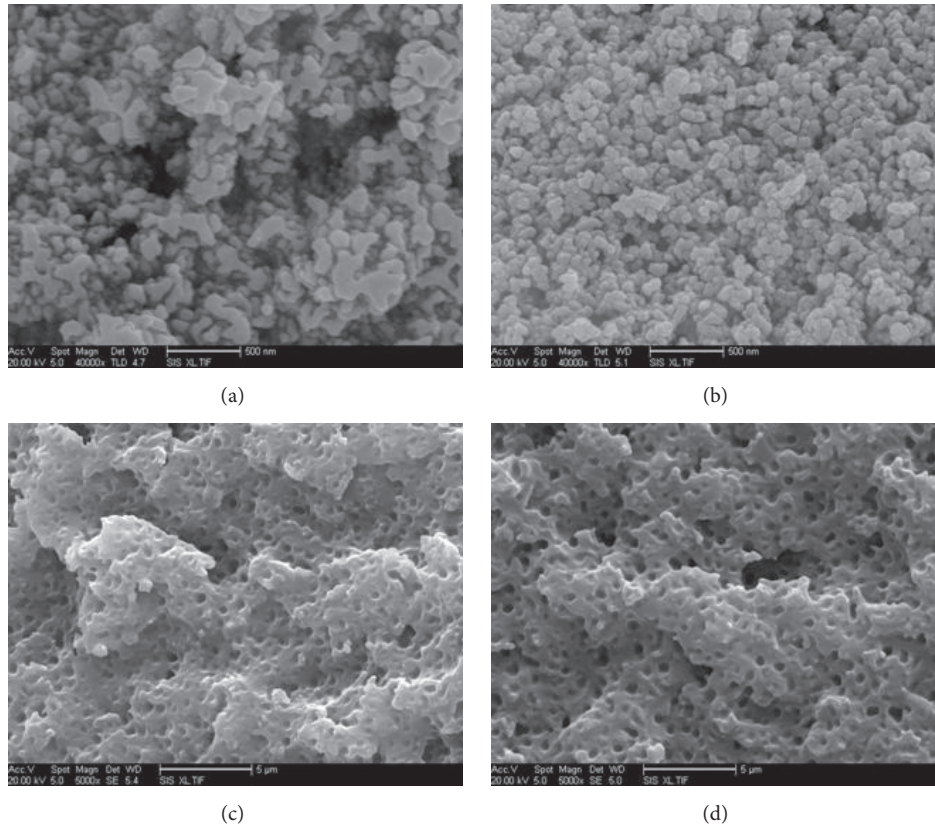


FIGURE 3: SEM photos of TiO_2 and TCA201- TiO_2 /EP-PU composite.

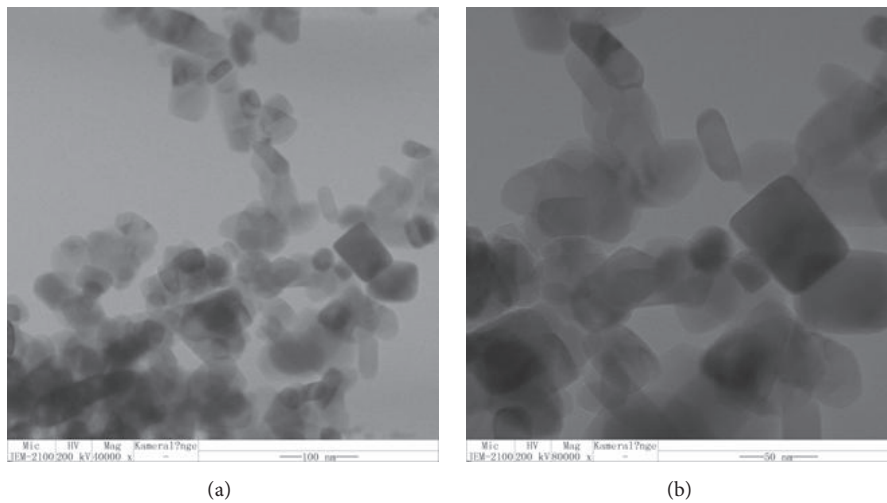


FIGURE 4: TEM patterns of TCA201- TiO_2 .

and there were nanoeffects. So the thermal stability of composites is enhanced. Fourthly, when the content of inorganic component was excessive, the interaction forces of inorganic particles would be enhanced and dispersion of two phases weakened and easily led to agglomeration in the epoxy resin.

Figure 7 shows SEM patterns for the breakdown point of 7 wt% TCA201- TiO_2 /EP-PU. Figures 7(a), 7(b), and 7(c) show back breakdown point of composite and Figure 7(d) shows face breakdown point of composite.

It was seen that a large number of inorganic components were separated (in Figures 7(a), 7(b), and 7(c)). This was because electrical energy would transform into heat energy in the breakdown processing; the heat energy caused epoxy resin matrix to decompose and inorganic component of composite was separated [16, 17]. And the heat energy of back breakdown could not spread rapidly; therefore, it would produce thermal loss. The produced heat energy during face breakdown of composite radiated its heat away into space and

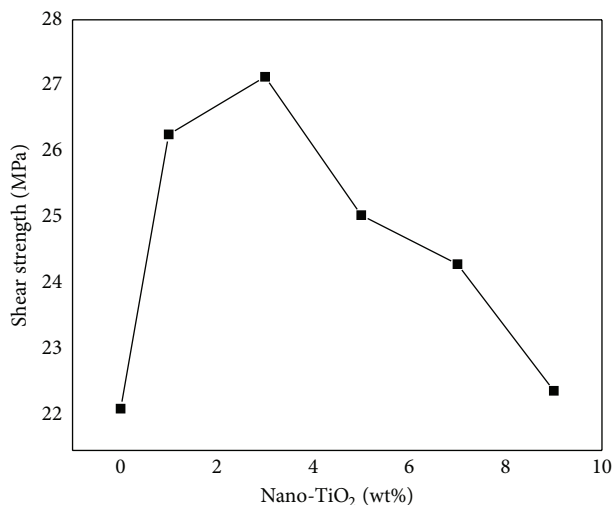


FIGURE 5: Shear strength curve of TCA201-TiO₂/EP-PU.

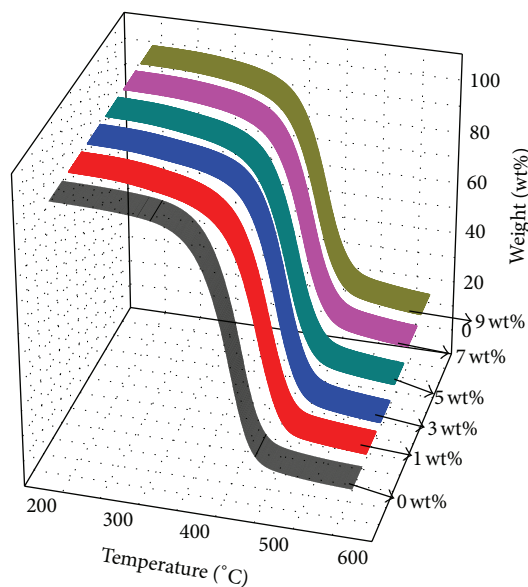


FIGURE 6: TG curve of TCA201-TiO₂/EP-PU.

could not make two-phase inorganic and organic component separate in Figure 7(d).

3.6. Dielectric Properties. Figure 8 shows the dielectric constant and dielectric loss curve of TCA201-TiO₂/EP-PU composites. It was noted that dielectric constant of TCA201-TiO₂/EP-PU increased with the increasing of amount of TCA201-TiO₂. As polar functional groups increased, it would result in the degree of polarization of the composite material to enhance and led to the increase of the dielectric constant eventually. At the same time, because nano-TiO₂ particles in epoxy resin had a good surface effect, other polarization also could occur in the two-phase interface of composite and led to increasing the degree of polarization of the composite [18].

Dielectric loss ($\tan \delta$) curve in Figure 8 displayed that $\tan \delta$ increased, too, with the increase of TCA201-TiO₂ filler. There could be two reasons; one was electrical conductivity loss of polar functional groups and the other was the relaxation loss of the polar functional groups. From the above analysis, conclusions were obtained that the polar functional groups of the composite materials were driven by electric field strength to generate strong polarization. And the content of TCA201-TiO₂ in composite increased and the number of the conductive carriers increased, too. Under the influence of an external electric field, it made the carrier bring about the directional movement phenomenon of the heat loss of dielectric material, ultimately.

3.7. Breakdown Field Strength. Breakdown strength of insulating material generally generates thermal breakdown and electrical breakdown at the breakdown point, and simultaneously electric energy was changed to thermal energy, so breakdown phenomenon would happen and the composite is destroyed. Though the modified nanoparticles and the organic polymer could be compatible well, and there were certain defects between the inorganic phase and the organic phase interface. It was seen in Figure 9 that the breakdown field strength of TCA201-TiO₂/EP-PU composite was reduced with the content of TCA201-TiO₂. Because insulating materials might release heat and convert part of the electrical energy into heat under an external electric field, the dielectric loss happened and the energy was lost. Therefore, the increase of dielectric loss gave the media issue more heat and enhanced temperature, which would break the balance of heating and cooling. In addition, TiO₂ had the semiconductor, so the conductivity of composites improved rapidly with the increase of temperature. This resulted in the decline of material breakdown strength [19].

It would aggravate the second reunion of nanoparticles in the composite curing process, which caused deformities of the electric field and made the temperature at test point of the local area slightly higher than the others. And this part of heat could not be well distributed out and make the thermal breakdown occur in this region. Secondly, there were some compatibility issues between the two-phase interfaces when inorganic particles and the epoxy matrix were mixed, at which some tiny bubbles and trap appeared in composite materials, and the defects also increased with the increase of TiO₂. These factors brought about the decline of breakdown field strength of composite material. Breakdown field strength of 3 wt%-TCA201-TiO₂/EP-PU composite was 14 kV/mm; it met the requirement of insulating material.

4. Conclusions

The results of FT-IR, TEM, and SEM demonstrated that TCA201 coupling agent had connected with TiO₂ particle through chemical cross-linking, and TCA201-TiO₂ could disperse well in EP-PU matrix. This would improve the properties of composite. When the amount of TCA201-TiO₂ was 3 wt%, shear strength gained maximum value for 27.14 MPa, the thermal decomposition temperature reached

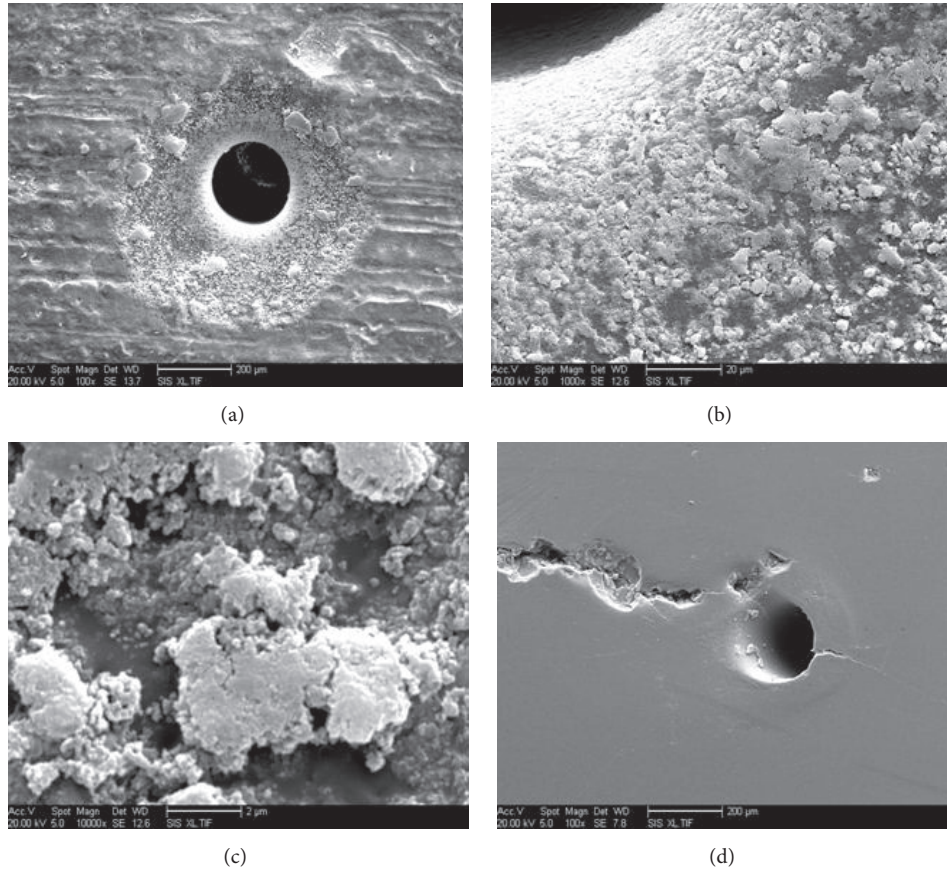


FIGURE 7: SEM of TCA201-TiO₂/EP-PU breakdown point.

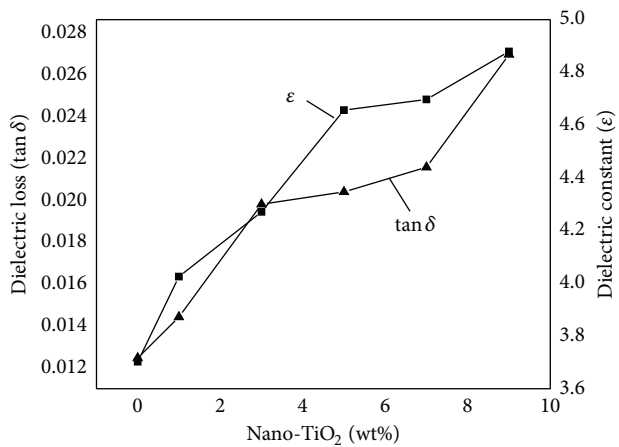


FIGURE 8: Dielectric constant and dielectric loss curves of TCA201-TiO₂/EP-PU.

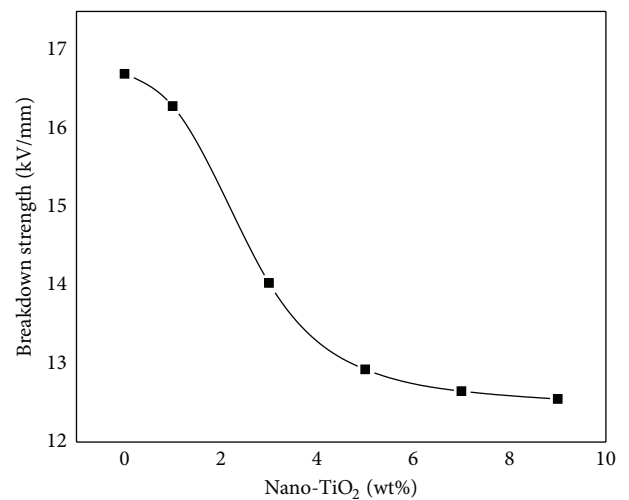


FIGURE 9: Breakdown strength curve of TCA201-TiO₂/EP-PU.

up to 397.82°C, which was higher 17.48°C than pure polymer matrix, breakdown field strength of composite was 14 kV/mm, and the performances could meet the requirement of insulating material.

Conflict of Interests

The authors declare that there is no conflict of interests regarding the publication of this paper.

Acknowledgment

The authors would like to express their appreciation to project supported by the Harbin Technology Bureau Subject Leader (2015RAXXJ029).

References

- [1] S. Sahila and L. S. Jayakumari, "Development of in situ generated graphene/benzoxazine-epoxy nanocomposite for capacitor applications," *Polymer Composites*, vol. 36, no. 1, pp. 1–7, 2014.
- [2] Q. Ren, H. Zou, and M. Liang, "The preparation and properties study of methoxy functionalized silicone-modified epoxy resins," *Journal of Applied Polymer Science*, vol. 131, no. 9, Article ID 40212, 2014.
- [3] S. C. Zunjarrao and R. P. Singh, "Characterization of the fracture behavior of epoxy reinforced with nanometer and micrometer sized aluminum particles," *Composites Science and Technology*, vol. 66, no. 13, pp. 2296–2305, 2006.
- [4] C. Wang and J. Jia, "Damping and mechanical properties of polyol cross-linked polyurethane/epoxy interpenetrating polymer networks," *High Performance Polymers*, vol. 26, no. 2, pp. 240–244, 2014.
- [5] H. A. Al-Turaif, "Effect of TiO₂ surface treatment on the mechanical properties of cured epoxy resin," *Journal of Coatings Technology Research*, vol. 8, no. 6, pp. 727–733, 2011.
- [6] D. V. Bavykin, J. M. Friedrich, and F. C. Walsh, "Protonated titanates and TiO₂ nano-structured materials: synthesis, properties, and applications," *Advanced Materials*, vol. 18, no. 21, pp. 2807–2824, 2006.
- [7] C.-C. Wu and S. L.-C. Hsu, "Preparation of epoxy/silica and epoxy/titania hybrid resists via a Sol-Gel process for nanoimprint lithography," *Journal of Physical Chemistry C*, vol. 114, no. 5, pp. 2179–2183, 2010.
- [8] Q. W. Shi, W. X. Huang, Y. B. Zhang, Y. Zhang, Y. Xu, and G. Guo, "Curing of polyester powder coating modified with rutile nano-sized titanium dioxide studied by DSC and real-time FT-IR," *Journal of Thermal Analysis and Calorimetry*, vol. 108, no. 3, pp. 1243–1249, 2012.
- [9] B. Wetzels, P. Rosso, F. Hauptert, and K. Friedrich, "Epoxy nanocomposites—fracture and toughening mechanisms," *Engineering Fracture Mechanics*, vol. 73, no. 16, pp. 2375–2398, 2006.
- [10] A. Mirmohseni and S. Zavareh, "Modeling and optimization of a new impact-toughened epoxy nanocomposite using response surface methodology," *Journal of Polymer Research*, vol. 18, no. 4, pp. 509–517, 2011.
- [11] A. J. Kinloch and A. C. Taylor, "The mechanical properties and fracture behaviour of epoxy-inorganic micro- and nanocomposites," *Journal of Materials Science*, vol. 41, no. 11, pp. 3271–3297, 2006.
- [12] P. Jyotishkumar, J. Koetz, B. Tiersch et al., "Complex phase separation in poly (acrylonitrile-butadiene-styrene)-modified epoxy/4,4'-diaminodi-phenylSulfone blends: generation of new micro- and nano-substructures," *Journal of Physical Chemistry B*, vol. 113, no. 16, pp. 5418–5430, 2009.
- [13] S.-R. Lu, Y.-M. Jiang, and C. Wei, "Preparation and characterization of EP/SiO₂ hybrid materials containing PEG flexible chain," *Journal of Materials Science*, vol. 44, no. 15, pp. 4047–4055, 2009.
- [14] Y.-F. Chen, Q.-W. Dai, C.-W. Lin, and T. Feng, "Characteristics and properties of SiO₂-Al₂O₃/EP-PU composite," *Journal of Central South University*, vol. 21, no. 11, pp. 4076–4083, 2014.
- [15] X. Wu, Y. Wang, L. Xie, J. Yu, F. Liu, and P. Jiang, "Thermal and electrical properties of epoxy composites at high alumina loadings and various temperatures," *Iranian Polymer Journal (English Edition)*, vol. 22, no. 1, pp. 61–73, 2013.
- [16] Y. Zheng, B. Zou, and L. Yuan, "Structure and properties of novel epoxy resins containing naphthalene units and aliphatic chains," *Iranian Polymer Journal*, vol. 22, no. 5, pp. 325–334, 2013.
- [17] H. Zhang, R. Qi, M. Tong, Y. Su, and M. Huang, "In situ solvothermal synthesis and characterization of transparent epoxy/TiO₂ nanocomposites," *Journal of Applied Polymer Science*, vol. 125, no. 2, pp. 1152–1160, 2012.
- [18] S.-W. Kou, S.-H. Yu, R. Sun, and H.-P. Yang, "Preparation and dielectric properties of the three-phase composites of graphite oxide/barium titanate/epoxy resin," *Journal of Inorganic Materials*, vol. 29, no. 1, pp. 71–76, 2014.
- [19] J. Jiao, L. Wang, P. Lv, Y. Cui, and J. Miao, "Improved dielectric and mechanical properties of silica/epoxy resin nanocomposites prepared with a novel organic-inorganic hybrid mesoporous silica. POSS-MPS," *Materials Letters*, vol. 129, no. 15, pp. 16–19, 2014.

Research Article

Synthesis and Characterization of Zinc Borate Nanowhiskers and Their Inflaming Retarding Effect in Polystyrene

Pingqiang Gao and Yan Zhang

College of Chemistry and Chemical Engineering, Yulin University, No. 4 Chong Wen Road, Yulin, Shaanxi 719000, China

Correspondence should be addressed to Pingqiang Gao; gpqzy2013@sina.com

Received 4 February 2015; Revised 17 March 2015; Accepted 19 March 2015

Academic Editor: Weidong Song

Copyright © 2015 P. Gao and Y. Zhang. This is an open access article distributed under the Creative Commons Attribution License, which permits unrestricted use, distribution, and reproduction in any medium, provided the original work is properly cited.

Zinc borate nanowhiskers $4\text{ZnO}\cdot\text{B}_2\text{O}_3\cdot\text{H}_2\text{O}$ were in situ successfully synthesized via one-step precipitation reaction. A set of experiments was performed to evaluate the influence of reaction temperature. Increasing the temperature up to 70°C led to the high purity of zinc borate nanowhiskers with a monoclinic crystal structure measuring 50 nm to 100 nm in diameter and approximately $1\ \mu\text{m}$ in length. However, higher temperature decreases the crystallization due to the emergence of other styles of zinc borate. Flame-resistant nanocomposites of polystyrene and zinc borate nanowhiskers were also successfully synthesized. The samples were investigated by XRD, FESEM, FTIR, and TG. The mechanical properties of the composites were also tested. The incorporation of zinc borate nanowhiskers improved the thermal and mechanical properties for polystyrene. FESEM images show that zinc borate nanowhiskers increased the smoothness of composites. The composites presented good responsive behavior in relation to LOI (limiting oxygen index) allowing them to be suitable for green flame retardants.

1. Introduction

Zinc borate is a commonly used material in a variety of industries. It is used as a lubricating oil additive and in refractory ceramic materials, nonlinear optical materials, and solid electrode materials, but its use in fire retardants is its most typical application [1–3]. Zinc borate is naturally occurring but it is also easily synthesized and is used as an inorganic fire retardant material because of its high surface area and its good mechanical properties.

The addition of zinc borate has been demonstrated to improve the fire retardant properties of polymers [4]. The effect of zinc borate has been attributed to the formation of a glassy char at the polymer surface which protects the bulk from the combustion zone. In addition, zinc borate has been recognized for its ability to suppress smoke and afterglow, which often occur during the burning of a polymer composite or wood [5, 6]. The compounds $2\text{ZnO}\cdot 3\text{B}_2\text{O}_3\cdot 3.5\text{H}_2\text{O}$, $2\text{ZnO}\cdot 3\text{B}_2\text{O}_3\cdot 3\text{H}_2\text{O}$, $2\text{ZnO}\cdot 3\text{B}_2\text{O}_3\cdot 7\text{H}_2\text{O}$, and $4\text{ZnO}\cdot \text{B}_2\text{O}_3\cdot \text{H}_2\text{O}$ are widely used as fire retardants. Among these, $4\text{ZnO}\cdot \text{B}_2\text{O}_3\cdot \text{H}_2\text{O}$ is the most important as it can be incorporated into polymers at much

higher temperatures due to its exceptionally high dehydration temperature (about 415°C).

Nanomaterials have unique properties due to their small size and as a result they have found applications in many industries [7, 8]. Researchers have become increasingly interested in nanoreinforcement of polymer matrices as it has been suggested that in general nanocomposites show improved properties when compared to similar microsized systems [9]. Nanowhiskers in particular have enhanced performance resulting from their high surface area and good mechanical properties [10–15]. Thus, there has been a growing interest in synthesizing nanowhiskers as nanoreinforcement for polymer matrices [16]. In these studies, fire retardant performance and mechanical properties of polymer matrices are improved by controlling the morphology and size of nanowhisker additives.

Recently, Zheng et al. [17] synthesized $4\text{ZnO}\cdot \text{B}_2\text{O}_3\cdot \text{H}_2\text{O}$ nanowhiskers and demonstrated their ability to increase the thermal stability of polyethylene. However, the application of zinc borate nanowhiskers to other polymers has not been explored. In this study, zinc borate nanowhiskers

($4\text{ZnO}\cdot\text{B}_2\text{O}_3\cdot\text{H}_2\text{O}$) were synthesized and their flame retardant behavior in polystyrene matrix was characterized. The effect of reaction temperature on the nanowhiskers formation is investigated by XRD and FESEM. The effects of the nanowhiskers on the thermal stability and mechanical performance of the polymer matrix were also evaluated. These results and the LOI provide information which allow for promising applications of this material.

2. Experimental Procedure

2.1. Materials. All chemicals in the synthesis process of this experiment, namely, $\text{Zn}(\text{NO}_3)_2\cdot 6\text{H}_2\text{O}$ (99.5 wt.% purity), $\text{Na}_2\text{B}_4\text{O}_7\cdot 10\text{H}_2\text{O}$ (99.5 wt.% purity), sodium dodecylbenzenesulfonate (SDBS) (99.5 wt.% purity), polystyrene, NaOH (96 wt.% purity), absolute ethanol, and cyclohexane, were bought from Tianjin Reagent Factory (Tianjin, China) and used as reactants without further purification. Distilled water was used during the treatment and synthesis processes.

2.2. Synthesis of Zinc Borate Nanowhiskers. In a typical procedure, 1.91 g of $\text{Na}_2\text{B}_4\text{O}_7\cdot 10\text{H}_2\text{O}$ and 0.5 g of sodium dodecylbenzenesulfonate (SDBS) are dissolved in 50 mL of distilled water at room temperature in a 1 L constant temperature water bath reactor equipped with a reflux condenser and a mechanical stirrer operating at 300 rpm. The reactor is placed in a water jacket to control the reaction temperature. The slurry is then heated at constant temperature for 30 min. Subsequently, a solution of 5.95 g $\text{Zn}(\text{NO}_3)_2\cdot 6\text{H}_2\text{O}$ in 10 mL of distilled water is added and stirred at 600 rpm. NaOH solution is used to adjust the pH to 7.0. The resulting solution is stirred for 7 h. The resulting precipitate is separated via centrifugation, washed with absolute ethanol and distilled water to remove adsorbed ions, and dried in a vacuum oven at 80°C for 12 h giving zinc borate nanowhiskers as a white powder.

2.3. Synthesis of Polystyrene/Zinc Borate Nanowhiskers. 15 g polystyrene is dissolved in 100 mL of cyclohexane in a 250 mL three-neck round-bottom flask equipped with a mechanical stirrer. The solution is stirred at 800 rpm until homogeneous. Zinc borate nanowhiskers are then added to polystyrene solution over the course of 2 h. Pouring the mixture onto a piece of clean glass gives the final polystyrene/zinc borate nanowhiskers composites.

2.4. Characterizations. Powder X-ray diffraction (XRD) measurements were carried out using a Bruker AXS GmbH Bruker D8 FOCUS automatic X-ray diffractometer to identify the crystal structure of the samples using Ni-filtered and graphite-monochromated $\text{Cu K}\alpha$ radiation ($\lambda = 1.5406 \text{ \AA}$, 40 kV, and 40 mA) with a step size of 0.02° . The registrations were performed in the 5° – 80° (2θ) range. HITACHI X-650 field-emission scanning electron microscope (FESEM) was used to characterize the morphology and size of the product (before SEM imaging, the sample was coated with thin layers of gold). Fourier transform infrared (FT-IR) spectroscopy of the samples as powder-pressed KBr pellets was examined

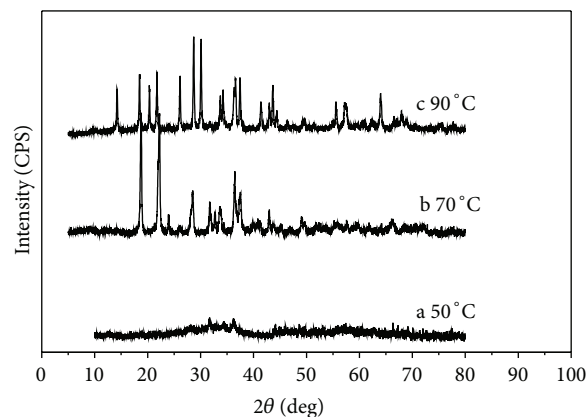


FIGURE 1: XRD patterns of samples obtained at different reaction temperature. (a) Reaction temperature: 50°C . (b) Reaction temperature: 70°C . (c) Reaction temperature: 90°C .

in the wave number range from 4500 to 400 cm^{-1} with a PerkinElmer 2000 spectrophotometer. The thermal gravimetric analysis (TG) was carried out on NETZSCH STA 409 instruments under N_2 atmosphere at a heating rate of $10^\circ\text{C min}^{-1}$. Mechanical property of composite samples was studied in a AG-10KNA Material Machine and the method was followed ASTM638 standard. LOI data of all products were obtained at room temperature with an oxygen index instrument (DRK304) (Jinan Drick Instruments Co., Ltd., China) produced by Jinan Drick Instruments Co., Ltd., according to ASTM D2863-77 standard. The dimensions of all samples are $120 \text{ mm} \times 7.0 \text{ mm} \times 3.0 \text{ mm}$.

3. Results and Discussion

3.1. XRD Spectra of Zinc Borate. The samples with a sort of stable white powders were obtained at room temperature. The XRD of zinc borate synthesized at different reaction temperature (50°C , 70°C , and 90°C) is illustrated in Figure 1. The data reveal that as the reaction temperature increases the resulting nanowhiskers become more crystalline. When the reaction temperature is set to 50°C , XRD of the resulting product shows only low intensity reflections demonstrating that the sample is largely amorphous (Figure 1, a). In contrast, when the reaction temperature is increased to 70°C , high-intensity peaks are observed at $2\theta = 16.40^\circ$, 20.35° , and 36.35° (Figure 1, b), indicating that the organized microporous framework in the sample is composed of a structure which is in good agreement with the crystal structure of zinc borate [18]. Additionally, when compared to the sample synthesized at 50°C , the microporous ordering is significantly improved in samples synthesized at 70°C . Increasing the reaction temperature to 90°C , however, results in the observation of many extra peaks (Figure 1, c). Some of the peaks, at about 34.45° and 56.63° , correspond to pure zinc oxide and other peaks to a different structure of zinc borate. This result indicates that when the reaction temperature is too high, zinc oxide reacts incompletely and can generate an undesirable form of zinc borate. Therefore, the optimal reaction temperature for $4\text{ZnO}\cdot\text{B}_2\text{O}_3\cdot\text{H}_2\text{O}$ nanowhiskers is 70°C .

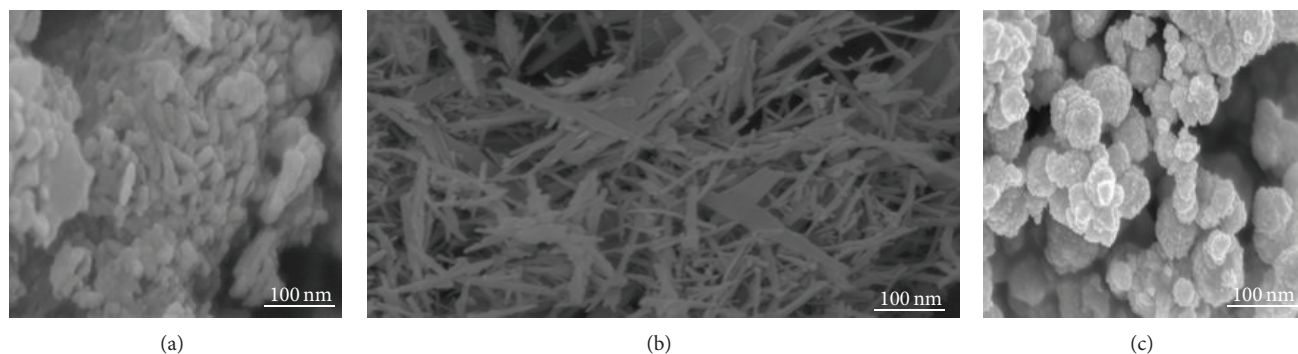


FIGURE 2: FESEM images of samples obtained at different reaction temperature. (a) Reaction temperature: 50°C. (b) Reaction temperature: 70°C. (c) Reaction temperature: 90°C.

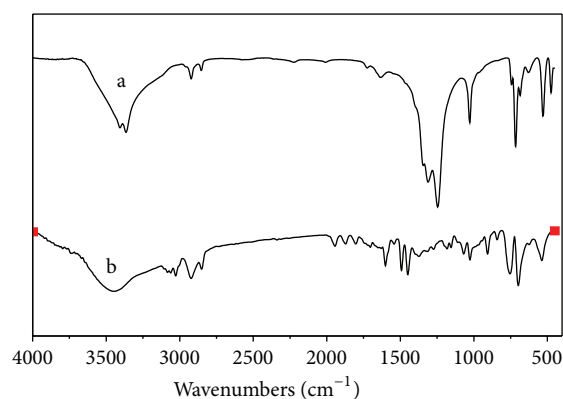


FIGURE 3: FT-IR images of the samples. (a) Zincborate nanowhiskers. (b) Polystyrene/zinc borate nanowhiskers composite materials.

3.2. FESEM Micrograph of Zinc Borate. The effects of reaction temperature on the zinc borates morphology were evaluated using SEM. Figure 2 shows the SEM images of zinc borate synthesized at 50°C, 70°C, and 90°C. The material synthesized at 50°C has small-sized whiskers with many disordered blocks. In contrast, the material synthesized at 70°C is composed of relatively uniform whiskers which are 50–100 nm in diameter, demonstrating that increased reaction temperature can promote the formation of ordered whiskers with regular morphology. However, when the temperature was further increased to 90°C, the sample consisted of several tiny-sized particles with irregular morphology. These experimental results show the effects of reaction temperature on the morphology of zinc borate nanowhiskers which are likely caused by changes in growth mechanisms and rates of crystallization.

3.3. FT-IR Spectrum of the Samples. The FTIR spectra of zinc borate nanowhiskers and of polystyrene/zinc borate nanowhiskers composites are shown in Figures 3-a and 3-b, respectively. The intensity of the absorption band at 3480 cm^{-1} , corresponding to the bending vibration of $-\text{OH}$, increases in the spectrum of polystyrene/zinc borate

nanowhiskers composite relative to that of the nanowhiskers alone. Additionally, absorption bands at 3200 cm^{-1} and 3000 cm^{-1} emerge in the composite, implying that the $-\text{OH}$ groups in zinc borate nanowhiskers interact with the polystyrene matrix. The absorption band at 1630 cm^{-1} also indicates interaction between the nanowhiskers and polystyrene. The absorption bands at 1605 cm^{-1} and 1541.87 cm^{-1} in the composite can be attributed to the $\nu\text{C} = \text{C}$ (benzene) and result from the presence of polystyrene. In addition, the absorption at 2922.54 cm^{-1} corresponds to the B-H stretching mode and the peaks at 1213.84 cm^{-1} , 718.26 cm^{-1} , and 537.57 cm^{-1} can be attributed to the B(3)-O stretching vibrations indicating the presence of zinc borate in the composite. Together, the FTIR results show that zinc borate nanowhiskers have been successfully introduced into the framework of the polystyrene.

3.4. FESEM Micrograph of the Composites. Many properties of polymers can be improved by adjusting their morphologies through the use of additives. The effects of the addition of zinc borate nanowhiskers on the morphology of polystyrene were evaluated using SEM. Figure 4 shows the FESEM micrographs of the fractured surface of pure polystyrene (Figure 4(a)) and the polystyrene/nanowhisker composite material (nanowhisker content is 7 wt. % (Figure 4(b))). In the pristine material, there are a number of discontinuous blocks of polymer mixed with large voids, which is undesirable in the macromolecule materials (Figure 4(a)). In comparison, the micrograph of the composite shows a fracture surface which is more homogeneous and continuous (Figure 4(b)). In the composite, no voids or blocks of polystyrene were observed and, interestingly, the interface between the polymer and nanowhiskers is not clear, suggesting that a protective layer has been formed in the composite which could protect the polymer from burning during the combustion process and improve the flame retardant behavior of the composite. This result is consistent with analysis of LOI.

3.5. TG of the Samples. TG is a widespread method used to investigate the thermal decomposition of polymers.

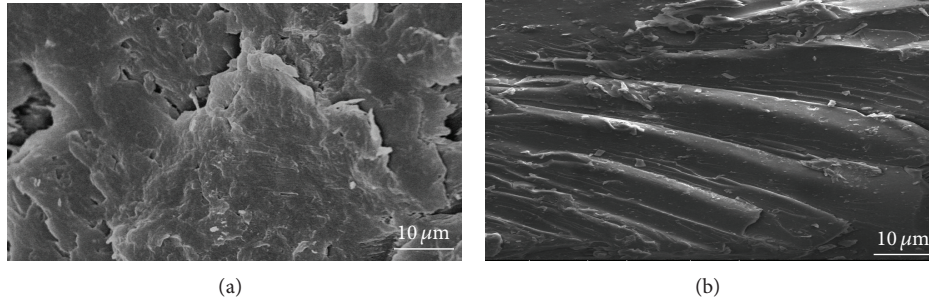


FIGURE 4: FESEM images of the products: (a) pure polystyrene and (b) polystyrene/zinc borate nanowhiskers composite materials (zinc borate nanowhiskers $4\text{ZnO}\cdot\text{B}_2\text{O}_3\cdot\text{H}_2\text{O}$ content is 7 wt.%).

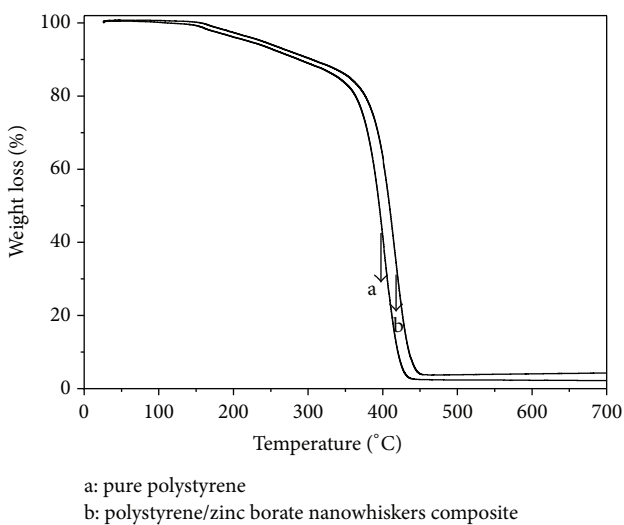


FIGURE 5: TG of the samples: (a) pure polystyrene and (b) polystyrene/zinc borate nanowhiskers composite materials (zinc borate nanowhiskers $4\text{ZnO}\cdot\text{B}_2\text{O}_3\cdot\text{H}_2\text{O}$ content is 7 wt.%).

Figure 5 shows the degradation curves of pure polystyrene (Figure 5, a) and the polystyrene/nanowhiskers composite (nanowhisker content is 7 wt.% (Figure 5, b)). The TG curve of pure polystyrene shows that its weight changes from 200°C to 500°C while the TG curve of the composite shows that dehydration occurs between 220°C and 530°C. The mass remainder ratios of polystyrene and the composite at 350°C were 83.4% and 86.2%, respectively. The difference between the two is probably caused by a few low molecular weight polymers which are less volatile in the polystyrene/zinc borate nanowhiskers composite. Additionally, because they release water into the vapor phase, the zinc borate nanowhiskers can effectively dilute the volatile species emanating from polymer degradation. A notable mass loss was observed when the temperature increased to 400°C, indicating that the nanocomposite has a higher decomposition temperature than pure polystyrene. It is reasonable to assume that the collapse of the nanocomposite structure during combustion forms a phosphate carbonaceous structure on the surface, which acts as a barrier to mass transport and insulates the underlying

polystyrene. Through this mechanism, the addition of zinc borate can improve the thermal stability of polystyrene.

3.6. Mechanical Property of Composite Samples. Figures 6(a) and 6(b) show the effects of zinc borate nanowhiskers loading on the mechanical properties of the composite. These results were obtained from the tensile test on the composites. The trends show that the tensile strength and tensile strain at break both increase with increased loading of zinc borate nanowhiskers until they reach a maximum and decrease with further addition of zinc borate nanowhiskers. When the content of the zinc borate nanowhiskers is 7 wt.%, the tensile strength reaches a maximum with a tensile strain at break of 26.4 MPa. These results indicate that the introduction of zinc borate nanowhiskers improves the tensile properties of polystyrene. The result may be due to the small size of the zinc borate nanowhiskers, resulting in a high surface-to-volume ratio and a large aspect ratio and thus a high-energy surface. The enhanced bonding between the polymer matrix and the nanoparticles with high interfacial energy is the cause of improved mechanical properties in these composites. The decrease in mechanical strength when zinc borate nanowhiskers content is too high probably results from the aggregation of zinc borate nanowhiskers which inhibits the bonding between the polymer matrix and the nanowhiskers.

3.7. LOI of the Composite Samples. Comparison of polystyrene/zinc borate nanowhiskers and polystyrene/commercial ZB2335 composites was accomplished by LOI as shown in Figure 7. The LOI of polystyrene was dramatically enhanced as zinc borate nanowhiskers were loaded up to 7%. It was shown that zinc borate nanowhiskers for polystyrene have a remarkable resistance characteristic. With the filler content improved to 9%, the reduction of LOI is tender. The probable reason is that zinc borate nanowhisker particles do not satisfactorily disperse. The curves show that the flame retardation of polystyrene/zinc borate nanowhiskers composites is exceedingly excellent compared with that of ZB2335 for polystyrene. This result shows that the optimum content of zinc borate nanowhiskers in the nanocomposites had the outstanding capability of inflaming retarding.

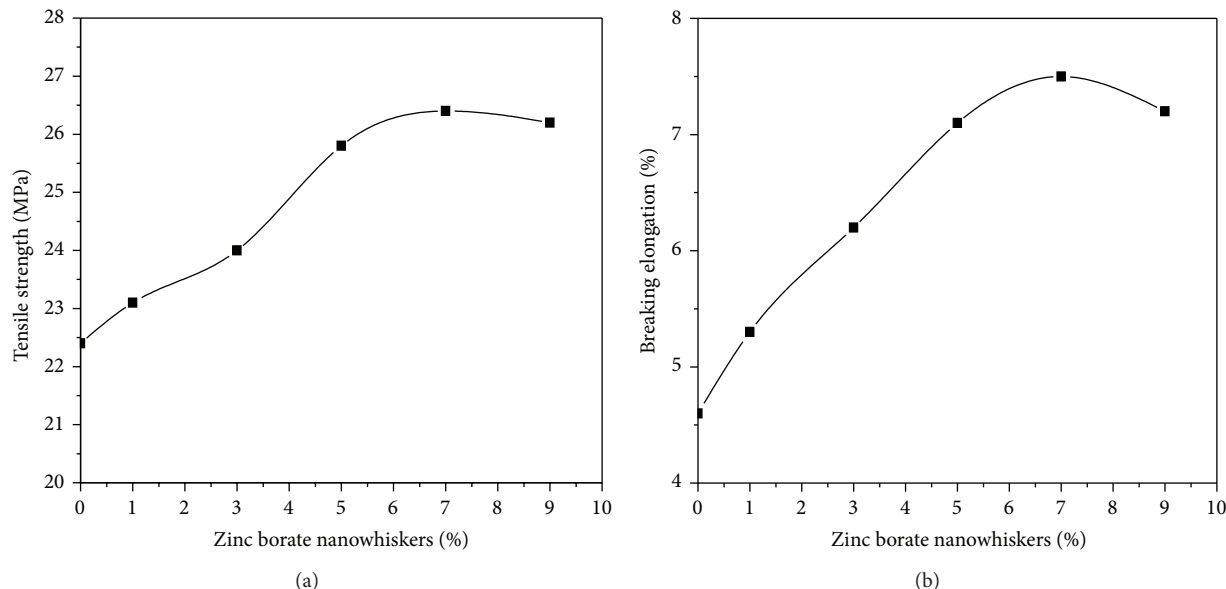


FIGURE 6: Effect of zinc borate nanowhiskers loading on mechanical properties of polystyrene/zinc borate nanowhiskers composites. (a) Effect of zinc borate nanowhiskers loading on tensile strength of polystyrene/zinc borate nanowhiskers composites. (b) Effect of zinc borate nanowhiskers loading on tensile strain at break of polystyrene/zinc borate nanowhiskers composites.

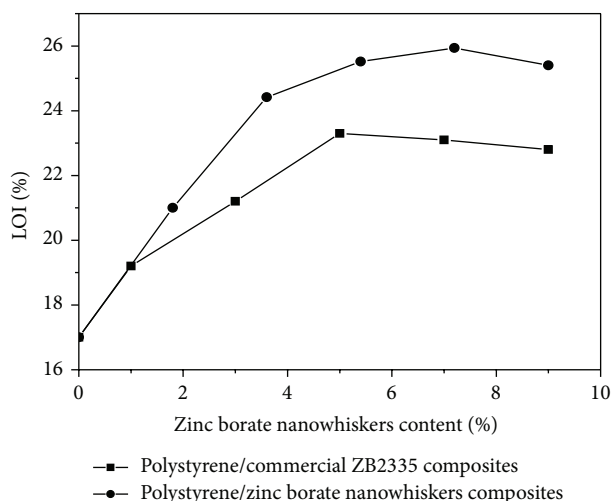


FIGURE 7: LOI of the composites.

4. Conclusions

Zinc borate nanowhiskers were successfully synthesized using the one-step precipitation method with zinc nitrate and borax as raw materials under the optimum temperature (70°C). The morphological analyses results revealed that zinc borate exhibited nanowhiskers morphology with particle sizes of 50 nm to 100 nm. The formed polystyrene/zinc borate nanowhiskers composite was confirmed by FTIR and FESEM data. The TG curve results indicate that the thermal stability of the polystyrene/zinc borate nanowhiskers composite is better than that of pure polystyrene. Improved bonding between the polymer matrix and the reinforcing phase results

in improved mechanical properties. Moreover, zinc borate nanowhiskers mainly improve the flame retardant property of polystyrene. When the dosage of zinc borate in polystyrene reached 7 wt.%, the LOI of the composite was the highest, indicating that the composite has the best flame retardant performance. Therefore, zinc borate nanowhiskers as green flame retardant have wide application in material industry.

Conflict of Interests

The authors declare that there is no conflict of interests regarding the publication of this paper.

References

- [1] T. Chen, L.-C. Deng, L.-S. Wang, Y. Yang, and F. Gang, "Synthesis of a new netlike nano zinc borate," *Materials Letters*, vol. 62, no. 14, pp. 2061–2063, 2008.
- [2] A. Durin-France, L. Ferry, J.-M. Lopez Cuesta, and A. Crespy, "Magnesium hydroxide/zinc borate/talc compositions as flame-retardants in EVA copolymer," *Polymer International*, vol. 49, no. 10, pp. 1101–1105, 2000.
- [3] P.-L. Cong, J. Yu, S. Wu, and X.-F. Luo, "Laboratory investigation of the properties of asphalt and its mixtures modified with flame retardant," *Construction and Building Materials*, vol. 22, no. 6, pp. 1037–1042, 2008.
- [4] C. A. Giúdice and J. C. Benítez, "Zinc borates as flame-retardant pigments in chlorine-containing coatings," *Progress in Organic Coatings*, vol. 42, no. 1-2, pp. 82–88, 2001.
- [5] L. Yang, "Preparation and characterization of fire retardant methyl vinyl silicone rubber based cable covering materials," *Procedia Engineering*, vol. 43, pp. 552–555, 2012.

- [6] X.-T. Qin, S.-Y. Zhu, S.-F. Chen, and K.-Y. Deng, "The mechanism of flame and smoke retardancy of asphalt mortar containing composite flame retardant material," *Construction and Building Materials*, vol. 41, no. 8, pp. 852–856, 2013.
- [7] M. Barral, P. Garmendia, M. E. Muñoz et al., "Novel bituminous mastics for pavements with improved fire performance," *Construction and Building Materials*, vol. 30, no. 5, pp. 650–656, 2012.
- [8] L. Haurie, A. M. Lacasta, A. Ciudad, V. Realinho, and J. I. Velasco, "Addition of flame retardants in epoxy mortars: thermal and mechanical characterization," *Construction and Building Materials*, vol. 42, pp. 266–270, 2013.
- [9] H. Liu, S. Liang, J.-H. Gao et al., "Development of biochars from pyrolysis of lotus stalks for Ni(II) sorption: using zinc borate as flame retardant," *Journal of Analytical and Applied Pyrolysis*, vol. 107, pp. 336–341, 2014.
- [10] H. E. Eltepe, D. Balköse, and S. Ülkü, "Effect of temperature and time on zinc borate species formed from zinc oxide and boric acid in aqueous medium," *Industrial & Engineering Chemistry Research*, vol. 46, no. 8, pp. 2367–2371, 2007.
- [11] Y.-M. Tian, Y.-P. Guo, M. Jiang et al., "Synthesis of hydrophobic zinc borate nanodiscs for lubrication," *Materials Letters*, vol. 60, no. 20, pp. 2511–2515, 2006.
- [12] J.-B. Chang, P.-X. Yan, and Q.-J. Yang, "Formation of borate zinc (ZnB_4O_7) nanotubes," *Journal of Crystal Growth*, vol. 286, no. 1, pp. 184–187, 2006.
- [13] X. X. Shi, M. Li, H. Yang et al., "PEG-300 assisted hydrothermal synthesis of $4ZnO \cdot B_2O_3 \cdot H_2O$ nanorods," *Materials Research Bulletin*, vol. 42, no. 9, pp. 1649–1656, 2007.
- [14] A. V. Shete, S. B. Sawant, and V. G. Pangarkar, "Kinetics of fluid-solid reaction with an insoluble product: zinc borate by the reaction of boric acid and zinc oxide," *Journal of Chemical Technology and Biotechnology*, vol. 79, no. 5, pp. 526–532, 2004.
- [15] Z. Li, D.-Z. Qin, Q.-R. Liu, and G.-X. He, "Biomimetic synthesis and characterisation of ZnS nanoparticles in aqueous solution of lysozyme," *IET Micro & Nano Letters*, vol. 7, no. 2, pp. 115–117, 2012.
- [16] X.-L. Chen, S.-Y. Wei, A. Yadav et al., "Poly(propylene)/carbon nanofiber nanocomposites: ex situ solvent-assisted preparation and analysis of electrical and electronic properties," *Macromolecular Materials and Engineering*, vol. 296, no. 5, pp. 434–443, 2011.
- [17] Y.-H. Zheng, Y.-M. Tian, H.-L. Ma et al., "Synthesis and performance study of zinc borate nanowhiskers," *Colloids and Surfaces A: Physicochemical and Engineering Aspects*, vol. 339, no. 1–3, pp. 178–184, 2009.
- [18] S. Bourbigot, M. Le Bras, R. Leeuwendal, K. K. Shen, and D. Schubert, "Recent advances in the use of zinc borates in flame retardancy of EVA," *Polymer Degradation and Stability*, vol. 64, no. 3, pp. 419–425, 1999.

Research Article

Epoxy Resin Composite Bilayers with Triple-Shape Memory Effect

Xixi Li,¹ Yaofeng Zhu,¹ Yubing Dong,² Meng Liu,¹ Qingqing Ni,² and Yaqin Fu¹

¹Key Laboratory of Advanced Textile Materials and Manufacturing Technology, Ministry of Education, Zhejiang Sci-Tech University, Hangzhou 310018, China

²Faculty of Textile Science and Technology, Shinshu University, 3-15-1 Tokida, Ueda 386-8576, Japan

Correspondence should be addressed to Yaqin Fu; fyq01@zstu.edu.cn

Received 28 April 2015; Revised 9 July 2015; Accepted 4 August 2015

Academic Editor: Bin Li

Copyright © 2015 Xixi Li et al. This is an open access article distributed under the Creative Commons Attribution License, which permits unrestricted use, distribution, and reproduction in any medium, provided the original work is properly cited.

Triple-shape memory epoxy composites with bilayer structures of well-separated glass transition temperatures have been successfully prepared. The different glass transition temperatures of the epoxy composites were obtained by physically incorporating various amounts of nanosilica particles, which were introduced into the epoxy by utilizing polyethylene glycol. A scanning electron microscope and a transmission electron microscope were used to analyze the dispersibility of the nanosilica particles. The effects of nanosilica particles on the mechanical properties as well as on the dual-shape memory effects (DSME) and triple-shape memory effects (TSME) of the nanocomposites were studied. The nanosilica particles were homogeneously dispersed in the matrix and well incorporated into the epoxy matrix. The resulting nanocomposites exhibited excellent TSME, and their shape fixity properties were significantly improved by nanosilica particles.

1. Introduction

Shape memory polymers (SMPs) are smart materials that can fix their deformed temporary shapes and recover their permanent shapes in a defined way upon external stimuli [1–3]. SMPs have attracted considerable attention because of their promising applications in textiles [4–6], adhesives [4, 5], smart coatings [4–9], biomedical devices [4–6, 10], and aerospace structures [6, 10].

In recent years, triple-SMPs (TSMPs) have received even greater attention because shape changes are no longer limited to being unidirectional but could now potentially offer unique opportunities in many applications, including morphing aircrafts, fasteners, and medical devices [1, 11]. Unlike conventional dual-SMPs, which can recover from a temporary shape to a permanent shape, TSMPs can fix two temporary shapes and recover sequentially from one temporary shape to the other and eventually to the permanent shape [12]. TSMPs have either more than one switching thermal transition [1] or a single switching transition with a broad thermal transition range [13]. Triple-shape memory effects

(TSME) can be achieved through many ways, including polymers blends, grafting and blocking copolymers, SMP hybrids, and polymer laminates [14]. Bellin et al. [15] first reported a SMP with a two-step TSME by copolymerizing poly(ethylene glycol) monomethyl ether monomethacrylate with poly(caprolactone) dimethacrylate. The grafting and blocking copolymers of different soft segments result in more than one well-separated multiple phase in a single SMP. Bae et al. prepared SMPU bilayer films of different molecular weights with nanosilica particles acting as multifunctional cross-links and reinforcing fillers [16]. Xie et al. prepared TSMP bilayer epoxy by curing the high T_g epoxy layer on top of the low T_g epoxy layer [1].

Herein, novel triple-shape memory epoxy nanocomposites with two different glass transition temperatures have been prepared through casting nanosilica/epoxy nanocomposites layer by layer. By varying the amounts of polyethylene glycol (PEG) and nanosilica in the epoxy system, we achieved a series of composite layers with different glass transition temperatures. The dispersibility of the nanosilica particles was evaluated via field emission scanning electron microscopy

TABLE 1: Raw material ratios of pure EP and A_{10} , A_{00} , A_{01} , and A_{02} .

	E-51 (g)	PA (g)	Nanosilica (g)	PEG (g)
EP	50	39	0	0
A_{10}	50	39	0	20
A_{00}	50	39	0	10
A_{01}	50	39	1	10
A_{02}	50	39	2	10

(FE-SEM) and transmission electron microscopy (TEM). The effects of the nanosilica particles on the mechanical and shape memory properties of the composites were analyzed and discussed.

2. Experiment

2.1. Materials. Epoxy resin E-51 (WSR618) and the curing agent (PA) were procured from Jinhong Resin Factory, Hangzhou, China. Nanosilica (15 ± 5 nm) was obtained from Aladdin Chemical Reagents Co., Ltd., Shanghai, China. Polyethylene glycol 200 (PEG200) was purchased from Shanghai Putong Gaonan Chemical Plants, China.

2.2. Preparation of SiO_2 /Epoxy Resin Nanocomposites. SiO_2 /epoxy nanocomposites were prepared according to our previous report with a slight modification [17]. Typical procedure was as follows: a known amount of SiO_2 was dispersed in PEG by mechanical stirring for 3 h. Then epoxy resin and curing agent were dissolved in the SiO_2 dispersion under mechanical stirring for another 0.5 h. Subsequently, the mixture solution was degassed placed in a vacuum oven. And then, the mixture solution was poured into a Teflon mold, cured at 60°C for 4 h. Changing the mass ratio of the SiO_2 and PEG in the mixture and according to the above method, the SiO_2 /epoxy nanocomposites were obtained with different mass ratio of 1 wt% and 2 wt%, respectively. Meanwhile, the pure epoxy and the PEG mixed epoxy composites were also prepared in the absence of nanosilica particles via the method described above. The stoichiometric amounts of every material used to prepare the SiO_2 /epoxy nanocomposites have been listed in Table 1.

Bilayer SiO_2 /epoxy nanocomposite was prepared as follows: the mixture solution A_{02} was poured into a Teflon mold, cured at 60°C for 0.5 h. And then the mixture solution A_{10} was poured on top of the A_{02} , cured at 60°C for 3.5 h. Finally, the bilayer SiO_2 /epoxy nanocomposite was obtained with the weight ratio of A_{02} to A_{10} , that is, 2:1, and the sample was designated as B_{21} .

2.3. Characterization. The dispersibility of nanosilica particles dispersed in PEG and the fracture surfaces of some samples were characterized by field emission scanning electron microscope (ZEISS ULTRA55) and transmission electron microscope (TEM, JSM-2100).

Tensile properties of the composites were measured by using a universal testing machine (UTM) (Instron 3367R4415, Canton, MA, USA) at a crosshead of 5 mm/min.

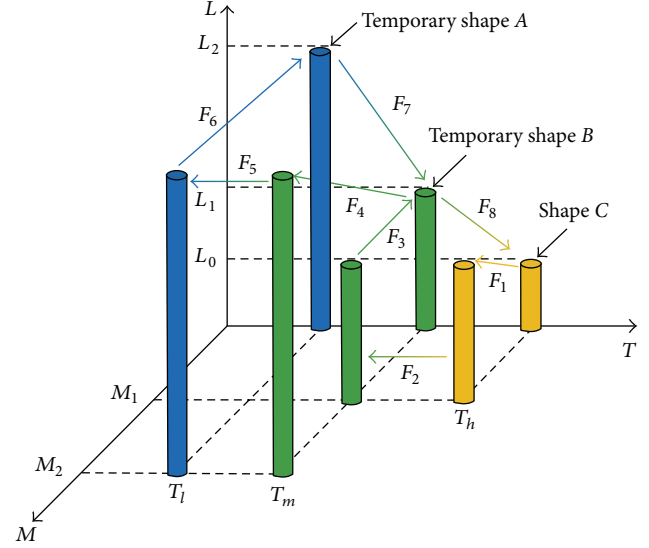


FIGURE 1: Schematic of a temperature (T)-loading stress (M)-length (L) plot showing the eight-step thermomechanical cycle for attaining triple-shape memory effect.

The dimensions of the rectangular film were $50 \text{ mm} \times 5 \text{ mm} \times 2 \text{ mm}$, and the length gripped the sample was 30 mm.

Dynamic mechanical analysis (DMA) was performed with the use of DMA Q800 (TA Instruments, New Castle, USA) in a uniaxial tension mode at 1 Hz and a heating rate of $3^\circ\text{C}/\text{min}$. The dimensions of the rectangular film were $10 \text{ mm} \times 5 \text{ mm} \times 2 \text{ mm}$.

A thermomechanical cycle test was conducted with a UTM with a temperature controlling chamber. To investigate the dual-shape memory effect (DSME), the sample was stretched to the maximum strain (ϵ_m) of 10% at T_{d1} ($T_{d1} > T_g$, where T_g is the glass transition temperature), followed by cooling the sample to T_{d2} ($T_{d2} < T_g$) and maintaining the load for several minutes. And then, the sample was unloaded at T_{d2} with an unloading strain (ϵ_u). The permanent strain (ϵ_p) was reached during the reheating of the sample from T_{d2} to T_{d1} . This completes a thermomechanical cycle and four circles were conducted to examine the shape recovery capacity of the composites. Shape fixity (R_f) and shape recovery (R_r) ratios for the cycle are defined as follows [16, 18]:

$$\text{Shape fixity ratio, } R_f = \frac{\epsilon_u}{\epsilon_m} \times 100\%,$$

$$\text{Shape recovery ratio, } R_r = \frac{\epsilon_r}{\epsilon_m} \times 100\%, \quad (1)$$

where $\epsilon_r = \epsilon_m - \epsilon_p$. T_{d1} and T_{d2} were 42°C and 15°C for A_{10} and A_{00} and 72°C and 42°C for A_{02} and A_{01} , respectively.

The triple-shape memory was performed through eight thermomechanical loading steps using a DMA Q800 in a uniaxial tension mode, as shown in Figure 1 [19]. The analysis was conducted under strain controlled programming and the heating and cooling rates were $3^\circ\text{C}/\text{min}$. At step 1 (F_1), the sample was stretched from L_0 to L_1 at T_h ($T_h > T_{\text{trans}1} > T_{\text{trans}2}$, where $T_{\text{trans}1}$ and $T_{\text{trans}2}$ are two thermal transition temperatures); the corresponding strain was recorded as ϵ_{mB} .

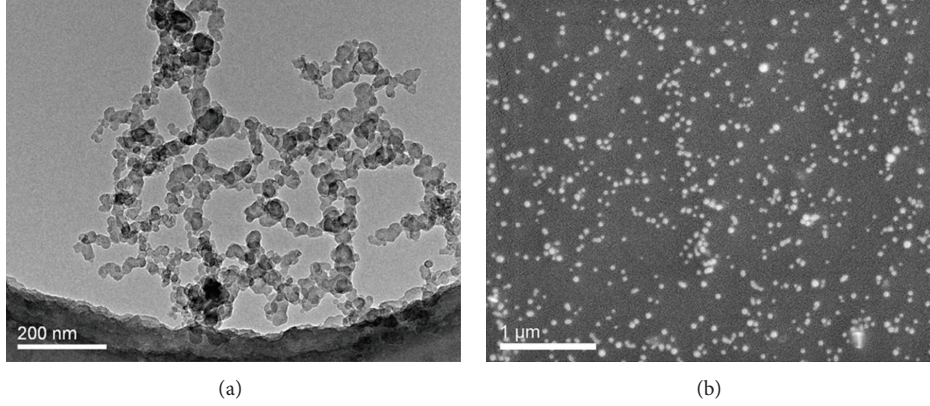


FIGURE 2: (a) TEM and (b) FE-SEM images of nanosilica dispersed in PEG.

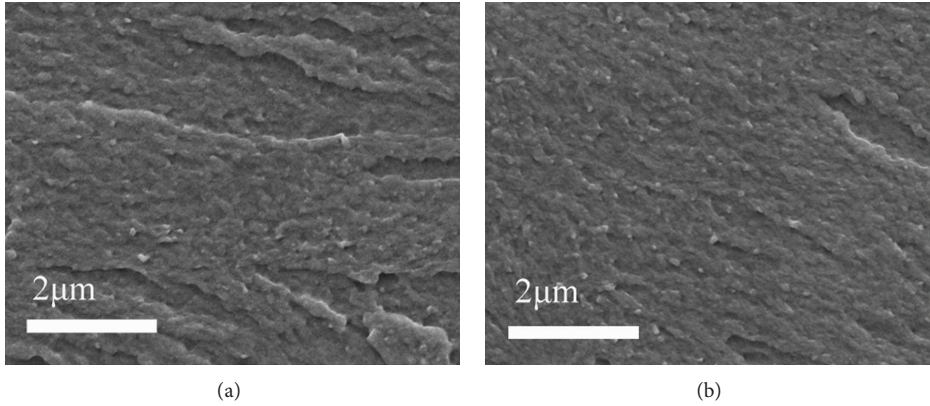


FIGURE 3: Cross section morphology of silica/epoxy nanocomposites: (a) A_{01} and (b) A_{02} .

At step 2 (F_2), the sample was cooled to T_m ($T_{\text{trans1}} > T_m > T_{\text{trans2}}$) and the load was maintained, where A_{10} and A_{02} were glassy and rubbery states, respectively. At step 3 (F_3), the external load was removed, and the sample was fixed at the first temporary shape B , with the strain of ε_{uB} :

$$R_{fB} = \frac{\varepsilon_{uB}}{\varepsilon_{mB}} \times 100\%, \quad (2)$$

where ε_{mB} and ε_{uB} are the maximum and the unloading strains, respectively.

At step 4 (F_4), the sample was further stretched to the strain of ε_{mA} (L_2) at T_m . At step 5 (F_5), the sample was cooled to T_l while keeping the strain at ε_{mA} . At step 6 (F_6), the second temporary shape A with a strain of ε_{uA} was fixed at T_1 after the removal of the external force:

$$R_{fA} = \frac{\varepsilon_{uA} - \varepsilon_{uB}}{\varepsilon_{mA} - \varepsilon_{uB}}, \quad (3)$$

where ε_{mA} and ε_{uA} are the maximum and unloading strains, respectively.

At step 7 (F_7), the sample was reheated to T_m , and it was recovered to the first temporary shape B , with the strain of ε_{pB} . At step 8 (F_8), the sample was recovered to shape C with

the strain of ε_{pC} by heating back to T_h . The recovery ratio of shape band shape C was obtained as follows:

$$R_{rB} = \frac{\varepsilon_{uA} - \varepsilon_{pB}}{\varepsilon_{uA} - \varepsilon_{uB}}, \quad (4)$$

$$R_{rC} = \frac{\varepsilon_{pB} - \varepsilon_{pC}}{\varepsilon_{uB}}.$$

T_l , T_m , and T_h are set to 15°C, 42°C, and 72°C, respectively; $\varepsilon_{mB} = 2.5\%$ and $\varepsilon_{mA} = 5\%$.

3. Results and Discussion

3.1. Morphology of Nanocomposites. Figure 2 shows the morphology evolution of nanosilica dispersed in PEG. Figure 2(a) and Figure 2(b) are the TEM and FE-SEM images of nanosilica dispersed in PEG, respectively. It confirms that the nanosilica particles are well distributed and no agglomerates present in the PEG. The cryofractured cross section of the silica/epoxy nanocomposites was observed by FE-SEM. In Figure 3, the samples A_{01} (Figure 3(a)) and A_{02} (Figure 3(b)) images reveal that the nanosilica particles are also well dispersed in the epoxy matrix. Through the typical process, it is noted that the obtained silica/epoxy nanocomposites

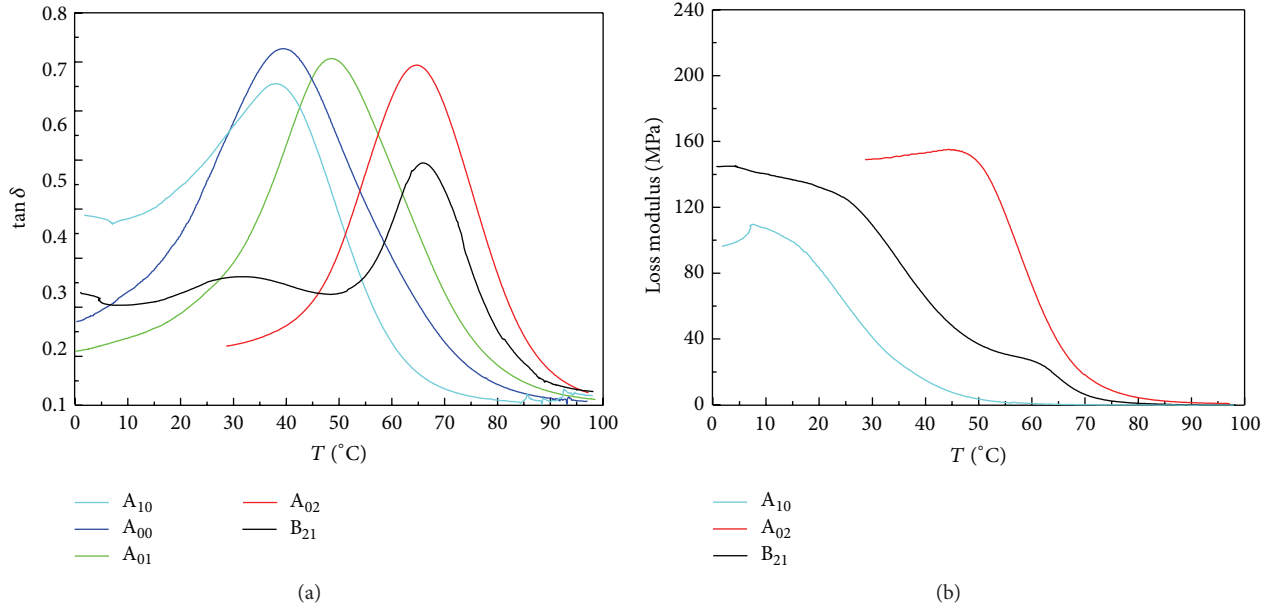


FIGURE 4: DMA curves for the samples.

TABLE 2: Glass transition temperature (T_g) of A₁₀, A₀₀, A₀₁, A₀₂, and B₂₁.

Sample	A ₁₀	A ₀₀	A ₀₁	A ₀₂	B ₂₁
T_g (°C)	36	38	48	65	30, 66

are fully composed of well dispersion of nanosilica particles within epoxy matrix, which may lead to excellent mechanical properties of composites [17].

3.2. Dynamic Mechanical Properties. The dynamic mechanical properties of samples from the DMA test are shown in Figure 4. The samples A₁₀, A₀₀, A₀₁, and A₀₂ prepared in this study possess glass transition temperatures (T_g s) of 36°C, 38°C, 48°C, and 65°C, respectively, based on their tan delta peaks in the DMA curves (as shown in Figure 4(a)), as shown in Table 2. It is also noted that the T_g of sample was increased with the increasing amount of nanosilica and decreased with the increasing amount of PEG, which was attributed to the segmental motion of polymer that was hindered by nanosilica particles and PEG acted as a plasticizer.

In view of the well phase mixing of nanocomposites, A₀₂ and A₀₁ show a relatively narrow switching transition, implying that sufficient chain movement is achieved within that short temperature regime. The tan δ peaks of all of samples are relatively high (higher than 0.6) indicating that the significant difference between viscous and elastic components of SMP in the T_{trans} regime, which is of great benefit to shape recovery ratio of sample [20–22]. Moreover, in Figure 4(a), two tan δ peaks can be clearly observed in the curve of B₂₁, and it is also found that the sample B₂₁ possessed the two well-separated glass transitions, which is

shown in Figure 4(b). This phenomenon could be attributed to the formation of the phase-separated bilayer structure and provided the conditions to achieve TSME.

3.3. Mechanical Properties of the Composites. Figure 5 shows the stress-strain behaviors of the composites at different temperatures. It can be seen from the results of Figures 5(a), 5(c), and 5(e) that the break strength and elongation of the silica/epoxy nanocomposites were improved by the addition of nanosilica particles, except for the sample A₀₀ that has better break elongation than the samples A₀₁ and A₀₂ at 15°C. It may be attributed to the reinforcing function and homogeneous dispersion of the nanosilica particles as observed in the FE-SEM images (Figure 3). Moreover, the samples A₀₁ and A₀₂ also show good strain energy storage capacity which can be obtained from the area under the stress-strain curve, implying that the silica/epoxy nanocomposites may have better shape recovery effect [16, 20]. Meanwhile, the break strength and the elongation of the composites decreased with the increasing amount of PEG, indicating that PEG serves as plasticizer.

The stress-strain behaviors of B₂₁ depend on the temperature as illustrated in Figures 5(b), 5(d), and 5(f). Comparing with the stress-strain behaviors of B₂₁ at 15°C and 72°C, B₂₁ at 42°C exhibits an interesting phenomenon of the stress maintaining almost constant when the strain increased from 31% to 34%. This is mainly because the sample B₂₁ is consisted of two layers, including A₁₀ layer in the rubbery state and A₀₂ layer in the glassy state at 42°C, respectively. Additionally, A₁₀ layer of B₂₁ does not break at the strain of approximately 25%, whereas the sample A₁₀ breaks. This result might be due to the powerful interfacial adhesion of the two layers. For comparison, stress-strain behavior for pure EP at different

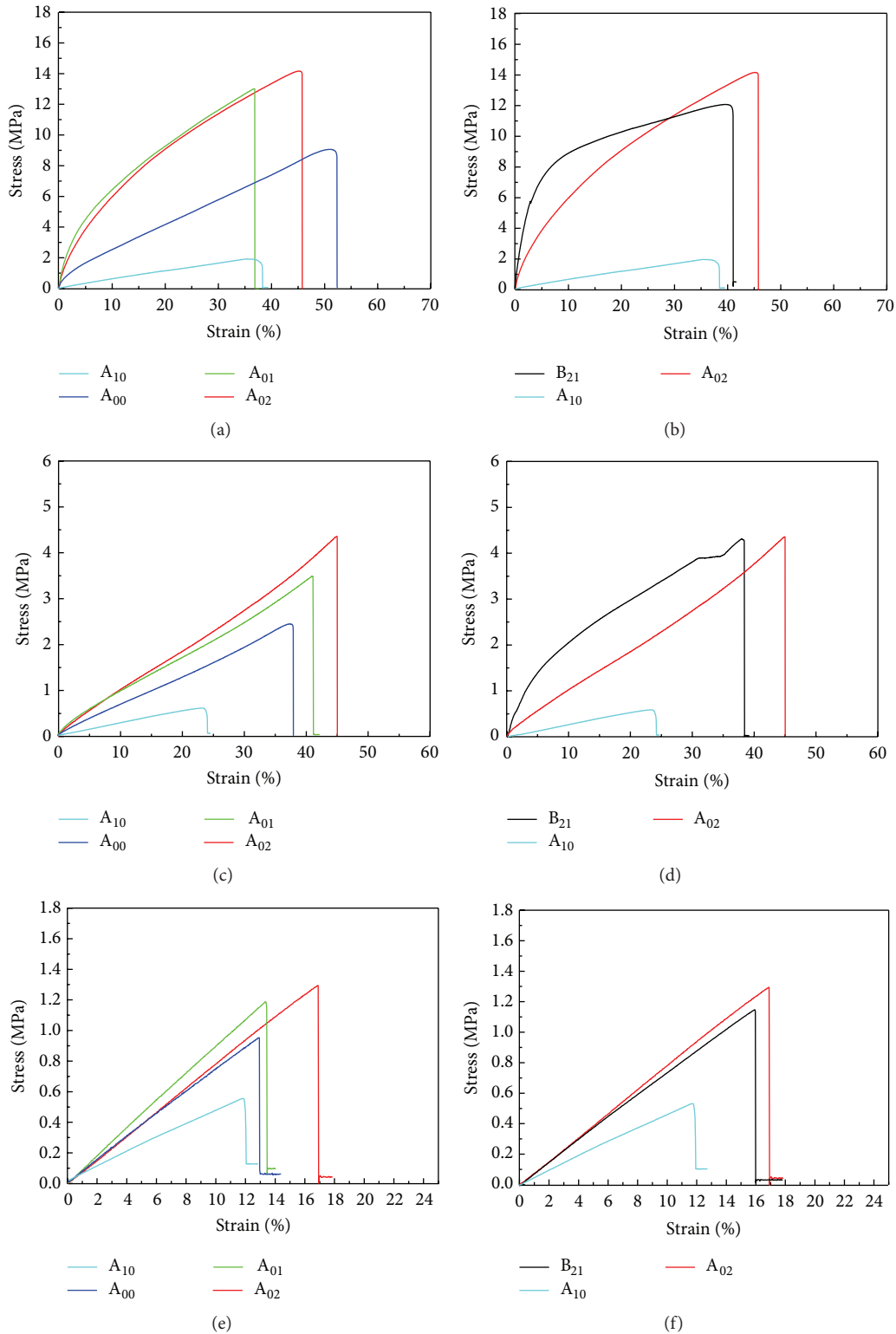


FIGURE 5: Stress-strain behavior of the samples at 15°C (a, b), 42°C (c, d), and 72°C (e, f).

temperatures is displayed in Figure 6. A notable difference between EP composites and pure EP is that the failure strain of EP composites is greatly improved due to the addition of PEG in EP matrix.

3.4. Shape Memory Behavior

3.4.1. DSME. The four cycles of thermomechanical behavior of the composites are shown in Figure 7, and the detailed

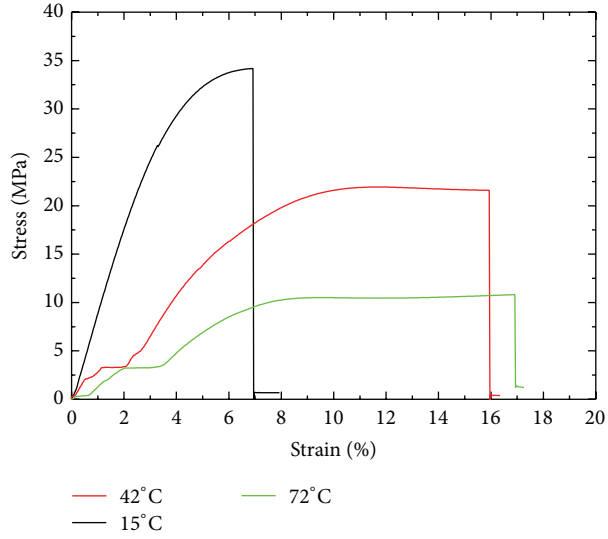


FIGURE 6: Stress-strain behavior of the pure EP at 15°C, 42°C, and 72°C.

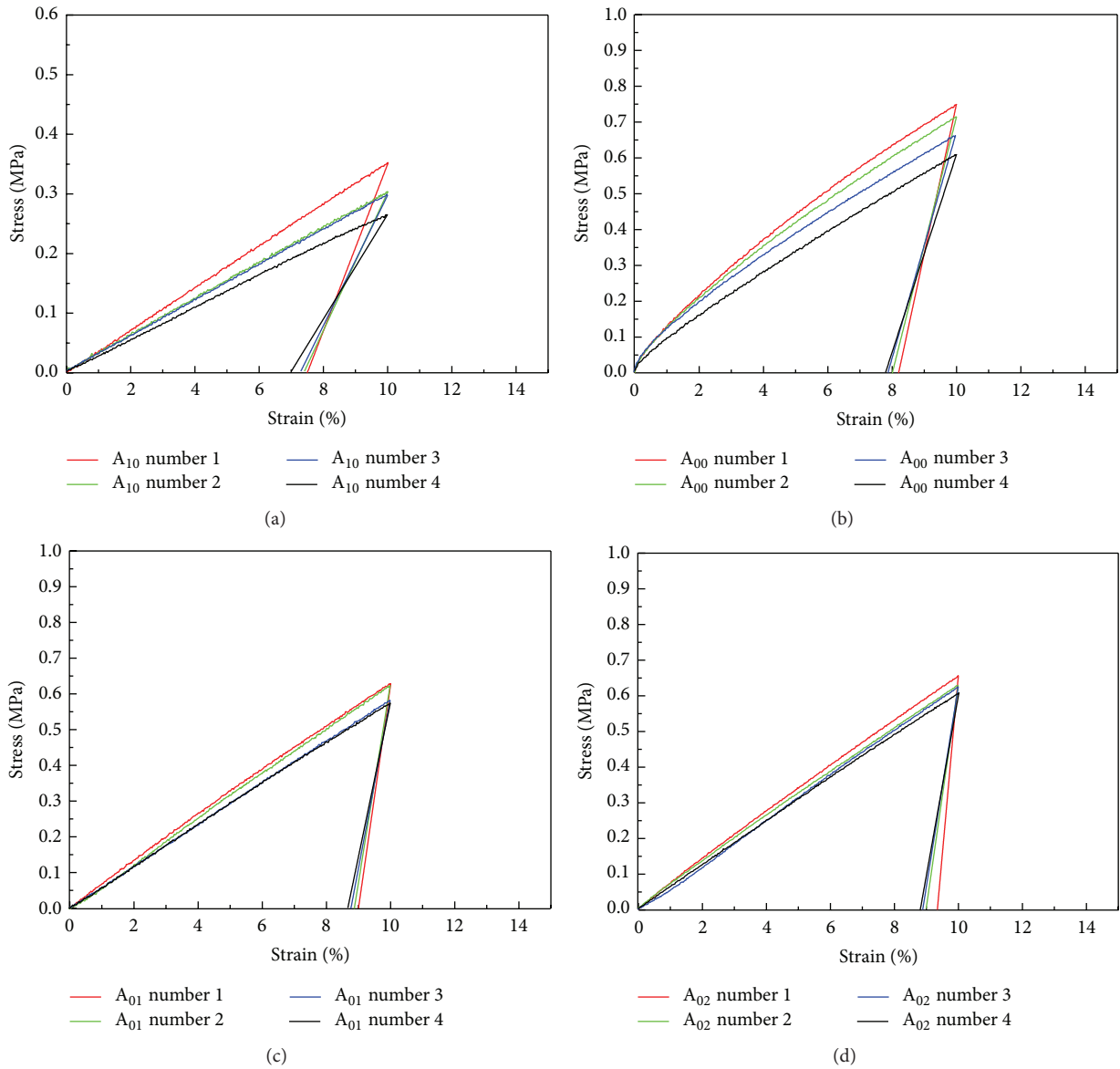


FIGURE 7: Thermomechanical cyclic behavior of (a) A_{10} , (b) A_{00} , (c) A_{01} , and (d) A_{02} .

TABLE 3: Shape fixity and shape recovery of A_{02} , A_{01} , A_{00} , and A_{10} (N = number of thermomechanical cycles).

$N^{(a)}$	Fixity ratio (%)				Shape recovery ratio (%)			
	A_{10}	A_{00}	A_{01}	A_{02}	A_{10}	A_{00}	A_{01}	A_{02}
1	75	82	90	93	98	99	99	99
2	74	80	89	90	98	99	99	99
3	73	79	88	89	98	98	98	99
4	70	78	87	88	96	97	97	97

^(a)Thermomechanical cycle number.

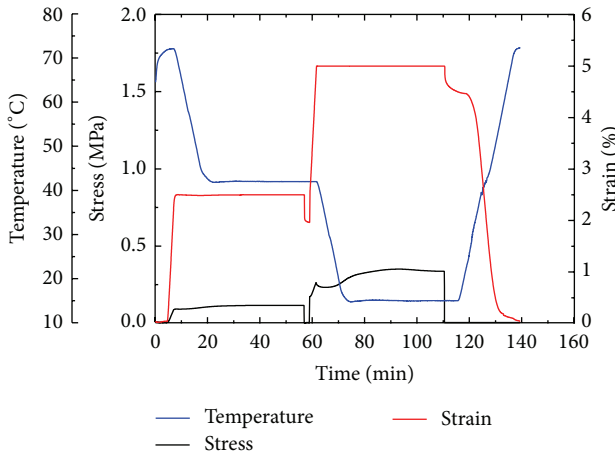


FIGURE 8: Triple-shape memory cycles of the sample for B_{21} .

data are summarized in Table 3. On the basis of DMA curves (Figure 6(a)), the rubbery state and glassy state of the samples A_{02} and A_{01} can be achieved at 72°C and 42°C, and those of the samples A_{00} and A_{10} can be achieved at 42°C and 20°C, respectively. The composites deformed in their rubbery state and generated a decrease in conformational entropy of the constituent polymer network chains. Then, the cooling down of the deformed material triggered vitrification, which kinetically traps the SMP in its low entropy state as a result of a significant reduction in chain mobility. Shape recovery is later initiated by reheating the material under stress-free conditions and allowing for the relaxation of polymer chain segments (with regained mobility) to their original entropically favored conformational state [11]. Additionally, it should be noted that the shape fixities of A_{00} and A_{10} are relatively low while the samples A_{01} and A_{02} display better shape fixities at 87–93% for the four cycles, which may be contributed from the addition of nanosilica particles. Furthermore, The shape recovery effect of all the samples was 96%–99%, especially the sample A_{02} that is better than the others. This finding is coincident with previous analysis.

3.4.2. TSME. The triple-shape memory capability for B_{21} is shown in Figure 8. The sample was first strained to 2.5% at 72°C, which was followed by cooling down to 42°C. After the stress was released, the strain instantaneously shrunk to 1.96%. At this step, the shape fixity was decided by the

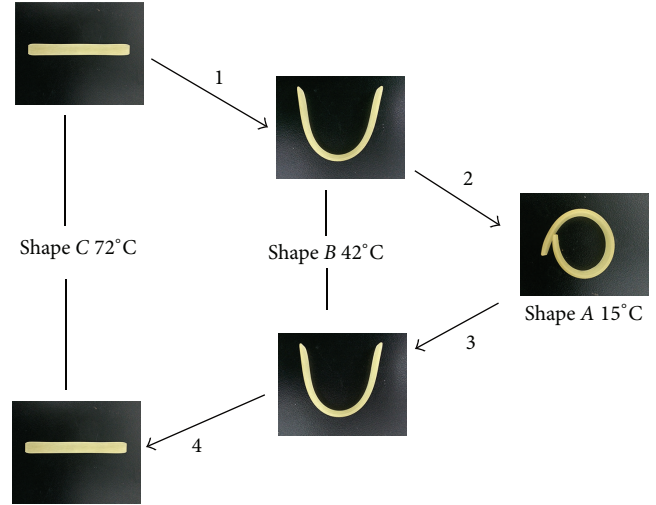


FIGURE 9: Illustration of triple-shape memory effect of B_{21} : shape (C) original shape, shape (B) first temporary shape, and shape (A) second temporary shape.

molecular frozen of A_{02} because rubbery state of A_{10} tended to recoil the sample. At last, the shape fixity ratio R_{fB} of 78% was achieved. Then, the sample was stretched to 5% at 42°C, followed by cooling down to 15°C and the subsequent releasing of the stress, and the strain shrunk from 5% to 4.5%. At 15°C, although both A_{02} and A_{10} were in glassy state, A_{02} had a tendency to keep shape B, resulting in R_{fA} of 84%. Finally, the sample was reheated to 42°C and 72°C; the strain was 2% and 0.04% at 42°C and at 72°C, respectively. $R_{rB} = 97%$ and $R_{rC} = 100%$ were calculated based on (4).

The TSME is further demonstrated visually in Figure 9. B_{21} was cut into a rectangular film of dimensions 50 mm × 5 mm × 2 mm (shape C). Shape C was first heated in an oven at 72°C and then quickly deformed to a “U” shape and quenched in a water bath at 42°C; some minor recovery occurred due to the not so perfect shape fixing ratio, but most of the deformation was kept and fixed at a temporary shape B (progress 1). After this, shape B was transformed into shape A and immersed in a water bath of 15°C; shape A was fixed at the same time (progress 2). Reheating to 42°C and 72°C, shape B and shape C recovered in turn (progress 3 and 4). Shape B and shape C behaved just the corresponding shape at the right temperature due to their excellent shape recovery ratio.

4. Conclusions

A novel bilayer epoxy system shape memory composites with TSME have been successfully synthesized and designed. The triple-shape memory nanocomposites were prepared by casting together two different shape memory composites exhibiting outstanding shape recovery effect. By varying the amount of PEG and nanosilica particles, we prepared a series of nanocomposites layers with different T_g . The dispersibility of the nanosilica particles and the failure strains of the nanocomposites were significantly improved by the addition

of PEG. The mechanical and shape memory fixity properties of the composites were significantly improved by the addition of nanosilica particles.

Conflict of Interests

The authors declare that they do not have any commercial or associative interest that represents a conflict of interests in connection with the work submitted.

Acknowledgment

This work was supported by the National Natural Science Foundation of China (NSFC) (Grant no. 51473147).

References

- [1] T. Xie, X. Xiao, and Y.-T. Cheng, "Revealing triple-shape memory effect by polymer bilayers," *Macromolecular Rapid Communications*, vol. 30, no. 21, pp. 1823–1827, 2009.
- [2] D. Ratna and J. Karger-Kocsis, "Recent advances in shape memory polymers and composites: a review," *Journal of Materials Science*, vol. 43, no. 1, pp. 254–269, 2008.
- [3] Y. Dong, Q.-Q. Ni, L. Li, and Y. Fu, "Novel vapor-grown carbon nanofiber/epoxy shape memory nanocomposites prepared via latex technology," *Materials Letters*, vol. 132, pp. 206–209, 2014.
- [4] T. Pretsch, "Review on the functional determinants and durability of shape memory polymers," *Polymers*, vol. 2, no. 3, pp. 120–158, 2010.
- [5] P. T. Mather, X. Luo, and I. A. Rousseau, "Shape memory polymer research," *Annual Review of Materials Research*, vol. 39, pp. 445–471, 2009.
- [6] J. Li, T. Liu, S. Xia et al., "A versatile approach to achieve quintuple-shape memory effect by semi-interpenetrating polymer networks containing broadened glass transition and crystalline segments," *Journal of Materials Chemistry*, vol. 21, no. 33, pp. 12213–12217, 2011.
- [7] A. Lendlein and S. Kelch, "Shape-memory polymers," *Angewandte Chemie-International Edition*, vol. 41, no. 12, pp. 2035–2057, 2002.
- [8] A. Lendlein, H. Jiang, O. Jünger, and R. Langer, "Light-induced shape-memory polymers," *Nature*, vol. 434, no. 7035, pp. 879–882, 2005.
- [9] T. F. Scott, A. D. Schneider, W. D. Cook, and C. N. Bowman, "Photoinduced plasticity in cross-linked polymers," *Science*, vol. 308, no. 5728, pp. 1615–1617, 2005.
- [10] R. Langer and D. A. Tirrell, "Designing materials for biology and medicine," *Nature*, vol. 428, no. 6982, pp. 487–492, 2004.
- [11] T. Pretsch, "Triple-shape properties of a thermoresponsive poly (ester urethane)," *Smart Materials and Structures*, vol. 19, no. 1, Article ID 015006, 2010.
- [12] X. Luo and P. T. Mather, "Triple-shape polymeric composites (TSPCs)," *Advanced Functional Materials*, vol. 20, no. 16, pp. 2649–2656, 2010.
- [13] T. Xie, "Tunable polymer multi-shape memory effect," *Nature*, vol. 464, no. 7286, pp. 267–270, 2010.
- [14] H. Meng, H. Mohamadian, M. Stubblefield et al., "Various shape memory effects of stimuli-responsive shape memory polymers," *Smart Materials and Structures*, vol. 22, no. 9, Article ID 093001, 2013.
- [15] I. Bellin, S. Kelch, R. Langer, and A. Lendlein, "Polymeric triple-shape materials," *Proceedings of the National Academy of Sciences of the United States of America*, vol. 103, no. 48, pp. 18043–18047, 2006.
- [16] C. Y. Bae, J. H. Park, E. Y. Kim, Y. S. Kang, and B. K. Kim, "Organic–inorganic nanocomposite bilayers with triple shape memory effect," *Journal of Materials Chemistry*, vol. 21, no. 30, pp. 11288–11295, 2011.
- [17] X. Fu, J. Wang, J. Ding, H. Wu, Y. Dong, and Y. Fu, "Quantitative evaluation of carbon nanotube dispersion through scanning electron microscopy images," *Composites Science and Technology*, vol. 87, pp. 170–173, 2013.
- [18] B. K. Kim, S. Y. Lee, and M. Xu, "Polyurethanes having shape memory effects," *Polymer*, vol. 37, no. 26, pp. 5781–5793, 1996.
- [19] Q. Ge, X. Luo, C. B. Iversen et al., "A finite deformation thermomechanical constitutive model for triple shape polymeric composites based on dual thermal transitions," *International Journal of Solids and Structures*, vol. 51, no. 15–16, pp. 2777–2790, 2014.
- [20] D. H. Jung, H. M. Jeong, and B. K. Kim, "Organic-inorganic chemical hybrids having shape memory effect," *Journal of Materials Chemistry*, vol. 20, no. 17, pp. 3458–3466, 2010.
- [21] B. K. Kim, S. H. Lee, and M. Furukawa, "Shape memory effects of multiblock thermoplastic elastomers," in *Handbook of Condensation Thermoplastic Elastomers*, chapter 18, pp. 521–566, Wiley, 2005.
- [22] K. S. S. Kumar, A. K. Khatwa, and C. P. R. Nair, "High transition temperature shape memory polymers (SMPs) by telechelic oligomer approach," *Reactive and Functional Polymers*, vol. 78, no. 1, pp. 7–13, 2014.

Research Article

Green Synthesis, Characterization, and Antibacterial Activity of Silver/Polystyrene Nanocomposite

Manal A. Awad,¹ W. K. Mekhamer,² Nada M. Merghani,³ Awatif A. Hendi,⁴
Khalid M. O. Ortashi,⁵ Fatimah Al-Abbas,² and Nada E. Eisa⁶

¹King Abdullah Institute for Nanotechnology, King Saud University, Riyadh 11321, Saudi Arabia

²Chemistry Department, Faculty of Science, King Saud University, Riyadh 11321, Saudi Arabia

³Central Lab, College of Science, King Saud University, Riyadh 11321, Saudi Arabia

⁴Physics Department, Faculty of Science, King Saud University, Riyadh 11321, Saudi Arabia

⁵Department of Chemical Engineering, King Saud University, Riyadh 11421, Saudi Arabia

⁶Department of Physics, University of Dammam, P.O. Box 1982, Dammam 31441, Saudi Arabia

Correspondence should be addressed to Manal A. Awad; a.manalawad@gmail.com and Awatif A. Hendi; ahindi@ksu.edu.sa

Received 18 April 2015; Revised 3 June 2015; Accepted 22 July 2015

Academic Editor: Bin Li

Copyright © 2015 Manal A. Awad et al. This is an open access article distributed under the Creative Commons Attribution License, which permits unrestricted use, distribution, and reproduction in any medium, provided the original work is properly cited.

A novel, nontoxic, simple, cost-effective and ecofriendly technique was used to synthesize green silver nanoparticles (AgNPs). The AgNPs were synthesized using orange peel extract as a reducing agent for silver nitrate salt (AgNO_3). The particle size distribution of AgNPs was determined by Dynamic Light Scattering (DLS). The average size of silver nanoparticles was 98.43 nm. The stable dispersion of silver nanoparticles was added slowly to polystyrene solution in toluene maintaining the temperature at 70°C. The AgNPs/polystyrene (PS) nanocomposite solution was cast in a petri dish. The silver nanoparticles encapsulated within polymer chains were characterized by X-ray diffraction (XRD) and Scanning Electron Microscopy (SEM) equipped with Energy Dispersive Spectroscopy (EDS) in addition to Transmission Electron Microscopy (TEM). The green AgNPs/PS nanocomposite film exhibited antimicrobial activity against Gram-negative bacteria *Escherichia coli*, *Klebsiella pneumoniae* and *Salmonella*, and Gram-positive bacteria *Staphylococcus aureus*. Thus, the key findings of the work include the use of a safe and simple AgNPs/PS nanocomposite which had a marked antibacterial activity which has a potential application in food packaging.

1. Introduction

The nanomaterials can be synthesized by different methods including chemical, physical, and biological methods. The development of new chemical or physical methods has resulted in environmental contamination, since the chemical procedures involved in the synthesis of nanomaterials generate a large amount of hazardous byproducts [1]. Thus, there is a need for “green nanotechnology” that includes a clean, safe, ecofriendly, and nontoxic method of nanoparticle synthesis, without the use of high pressure, energy, temperature, and toxic chemicals [2]. The biological methods include synthesis of nanomaterials from the extracts of plant, bacterial, fungal species, and so forth [3].

Nanoparticles of silver have been found to exhibit interesting antibacterial activity [4], and the investigation of this phenomenon has gained importance due to the increase of

bacterial resistance to antibiotics, caused by their overuse. Recently, materials have been developed (mainly textiles) containing silver nanoparticles, which exhibit very interesting antimicrobial activity. Antibacterial activity of the plastic-containing silver can be used, for example, in medicines to reduce infections as well as preventing bacteria colonization on plastic devices such as prostheses, catheters, vascular grafts, and dental materials [5]. Under ideal temperature and humidity conditions, plastics can be a good medium for the generation and the propagation of microorganisms which can cause irritations and infections. For these reasons, the polymeric materials must be protected against microorganisms in order to suppress their growth and dissemination. Owing to the high antimicrobial activity, relatively low cost, and easy production in a polymer-embedded form, nanoscopic silver could be a very adequate filler for such a purpose [6].

Silver nanoparticles (AgNPs) have been reported to form composites with polymers such as polyvinyl alcohol, polypyrrole, polyvinylidene fluoride, chitosan, and cellulose. The formation of polymer-silver nanocomposites requires that the size of nanoparticles in the polymer matrix be controllable and that their distribution within the polymer matrix be uniform [7]. Many previous attempts to form polymer-silver nanocomposites have involved mixing of a nanoparticle solution into the polymerization mixture. These polymer-silver nanocomposites can be used in a wide range of biomedical products, such as surgical gloves, antibacterial cloths and towels, and anti-infectious urinary catheters [8]; also they can be incorporated into aseptic coverings for plastic surgery, traumatic wounds, leg ulcers, skin grafts, incisions, and abrasions. Further, they can be used in numerous household applications such as textiles disinfection in water treatment, food storage containers, and home appliances and in medical devices [9].

The idea of the present study was green synthesis of AgNPs by chemical reduction of silver nitrate using orange peel extract as a reducing agent, and the preparation of AgNPs/polystyrene nanocomposite film. In addition, to study the antimicrobial potential of a silver-polystyrene nanocomposite system. To the best of our knowledge, this is the first study describing the preparation of silver nanoparticles using orange peel extract from toluene and their composite with polystyrene polymer.

2. Experimental

2.1. Chemicals Materials. For green synthesis of silver nanoparticles and silver/polystyrene nanocomposite, the reagents used were of analytical grade and were used as received without further purification. Silver nitrate (AgNO_3) was from Techno Pharmchem, India. Polystyrene was supplied by the Saudi Basic Industries Corporation (SABIC) (Saudi Arabia). The brand name for polystyrene is PS 125, with molecular weight, 259000 g/mole. Toluene, $\text{C}_6\text{H}_5\text{CH}_3$, molecular weight (92.14 g/mol), with 99.5% purity provided by (BDH Co).

2.2. Green Synthesis of Silver Nanoparticles. 200 mg of orange peel was crushed to which 20 mL of toluene was added with vigorous stirring for 10 minutes at 60°C to prepare the extract of orange peel. The extract then was centrifuged for 5 minutes at 7000 rpm at room temperature. Then, 1 mmole/mL silver nitrate was dissolved in 20 mL of toluene with vigorous stirring at 70°C for 5 minutes. Thereafter 5 mL of orange peel extract was added to the solution of silver nitrate, the color changed to brown which indicated reduction of Ag ions and the formation of silver nanoparticles.

2.3. Synthesis of Green AgNPs/PS Nanocomposite Film. Various methods are employed to prepare antimicrobial AgNPs/PS nanocomposite [10]. In our study, solution method was used to prepare antimicrobial AgNPs/PS films. 2 g of Polystyrene (PS) was added to the silver nanoparticles that were dispersed in toluene and synthesized as described in the previous section. The solution was stirred under vigorous

stirring at 60°C until PS completely dissolved. Then, the solution was cast in a glass plate and the toluene was allowed to evaporate at room temperature, to produce the nanocomposite film. The film was then removed from the glass plate after 24 hours.

2.4. Antimicrobial Study. The antibacterial activity of AgNPs/PS nanocomposite was evaluated against Gram-negative bacteria, *Escherichia coli* (*E. coli*), *Klebsiella pneumoniae*, and *Salmonella* and Gram-positive, *Staphylococcus aureus*, by disc diffusion method. Nutrient agar medium plates were prepared, sterilized, and solidified. After solidification, bacterial cultures were swabbed on these plates. Then, 0.5×0.5 cm from pure PS, 1% AgNPs-PS nanocomposite film, and 1 mmole/mL silver nanoparticles solution were placed in the nutrient agar plate and kept for incubation at 37°C for 24 hours. Zones of inhibition were measured. The experiments were repeated 3 times for each sample and mean values of zone diameter were determined [10].

2.5. Characterization of AgNPs-PS Nanocomposite Film. Nanocomposite film was characterized spectrophotometrically using X-ray diffraction, Bruker D8 Discover, while the size of synthesized green AgNPs was analyzed through Zetasizer, Nano series, HT Laser, ZEN3600 (Molvern Instrument, UK).

Transmission Electron Microscopy (JEM-1011, JEOL, Japan) was employed to characterize the size, shape, and morphologies of formed green synthesized nanocomposite accelerating voltage of 80 and 100 KV, while Thermo Scientific, Nicolet 6700, FT-IR spectrophotometer was used for recording the infrared (IR) spectrum.

Energy Dispersive Spectroscopy (EDS) analysis was performed for the confirmation of elemental silver. Elemental analysis on single particles was carried out using Oxford Instrument, Incax-act, equipped with Scanning Electron Microscopy using (JEOL-FE SEM, Japan).

3. Results and Discussions

3.1. X-Ray Diffraction Analysis. In this study, we described the characterization of the morphology, crystalline phase, composition, and structure of nanocomposites which was a combination of the silver nanosized powders and the (PS) polymer matrix.

Figure 1 shows XRD pattern of PS and AgNPs and AgNPs/PS nanocomposite. XRD pattern of PS shows that broad peaks appeared at $2\theta \sim 5\text{--}20^\circ$ which corresponds to a mixture of ordered and disordered structure of the amorphous phase of PS [11]. The amorphous halo is caused by the spacing of individual polymer chains.

A comparison between diffraction patterns of PS and AgNPs/PS nanocomposites showed that the peaks corresponding to PS became more broader, suggesting the smaller AgNPs embedded in PS chains [12].

3.2. Particle Average Size Determination by Zetasizer. The results of DLS Zetasizer showed very homogenous distribution of AgNPs with average particle size of 45.55 nm which

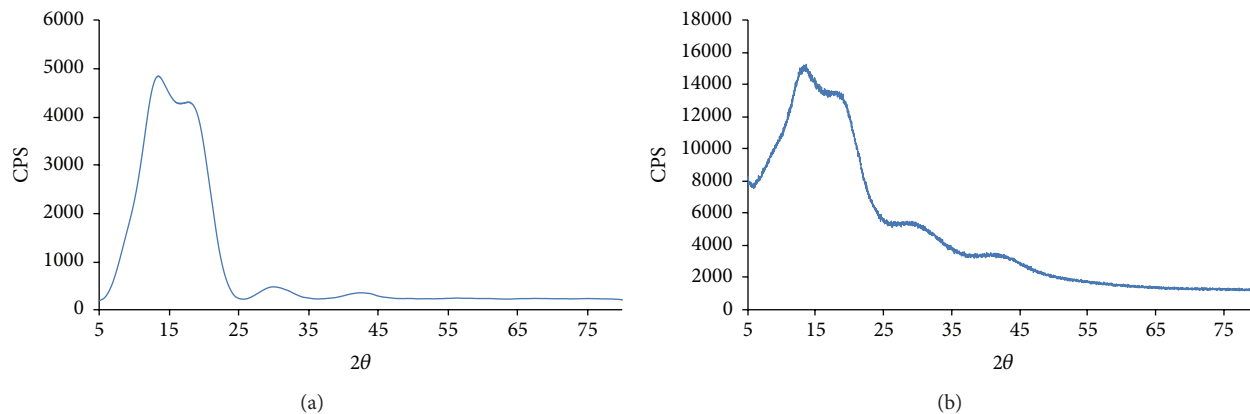


FIGURE 1: XRD pattern of PS (a) prepared film of AgNPs, PS nanocomposite (b).

	Diam. (nm)	Intensity (%)	Width (nm)
Z-average (r-nm): 98.43	Peak 1: 45.55	100.0	8.115
Pdl: 0.292	Peak 2: 0.000	0.0	0.000
Intercept: 0.971	Peak 3: 0.000	0.0	0.000

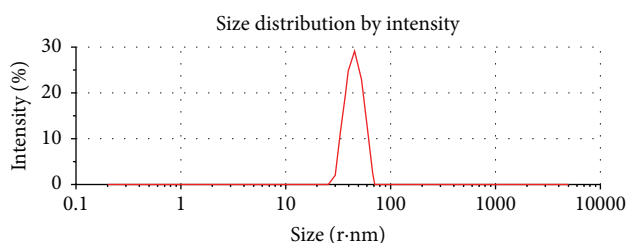


FIGURE 2: Particle size distribution of AgNPs.

is clearly observed from the appearance of one peak with an intensity 100% and width 8.115 nm as shown in Figure 2. This refers to monodispersity of nanoparticles which gives very high stability of nanoparticles for a long time. In addition, the (PDI), which is 0.292, indicates high stability and homogeneity of the resulting AgNPs.

3.3. TEM Analysis of Green Silver Nanoparticles and Green Nanocomposite. TEM technique was employed to visualize the shape and morphology of green nanoparticles produced. The electron micrograph (Figure 3) confirms data obtained from the DLS. TEM micrograph of AgNPs revealed that their average size ranged between 27 and 41 nm. Figure 3(b) shows distribution of AgNPs into the polystyrene matrix over the sample with spherical shape.

3.4. SEM and EDS Analysis of Green Silver Nanoparticles and Green Nanocomposite. Energy-dispersive spectroscopic (EDS) and SEM analysis investigated the presence of nanosilver in polystyrene matrix. The elemental analysis of AgNPs/PS nanocomposite film was studied by energy dispersive analysis of X-rays (EDS). Figure 4(b) shows EDS spectrum of AgNPs/PS nanocomposite. The peaks observed at the binding energies of 0.85, 1.0, and 3.4 keV correspond to the binding

energies of C, O, and Ag, respectively. The presence of carbon in the EDS spectrum is related to PS. The presence of oxygen could be due to the presence of residue of the extract of the orange peel such as fatty acid. The result corroborates the formation of AgNPs/PS nanocomposite film. The SEM image of silver nanoparticles exhibits that almost all the nanoparticles are of spherical shape dispersed in polystyrene matrix with no agglomeration.

3.5. FT-IR Analysis of Green Silver Nanoparticles and Green Nanocomposite. The interfacial interaction between AgNPs/PS nanocomposites was confirmed by FT-IR spectra (Figure 5). The infrared spectrum of PS features bands at 3066 cm^{-1} , 3025 cm^{-1} , 2922 cm^{-1} , and 2851 cm^{-1} due to the stretching of the (C-H) group. The peaks at $1666\text{--}1945$, $1491\text{--}1599$, $1188\text{--}1368$, and 1026 cm^{-1} could be attributed to the presence of aromatic C=C bonds stretching vibrations. The bands in the region $907\text{--}650\text{ cm}^{-1}$ can be assigned to the aromatic C-H bonds bending vibrations. The infrared of AgNPs/PS nanocomposites spectra showed all the characteristic bands of polystyrene (PS) in addition to bands at 441.8 and 422.5 cm^{-1} due to Ag. Also a slight shift in the band corresponding to PS was observed indicating the interaction between PS and AgNPs.

3.6. Antibacterial Efficacy of Green Silver Nanoparticles and Green Nanocomposite. The in vitro antibacterial screening of AgNPs/PS nanocomposite was tested against gram positive *Staphylococcus aureus* and gram negative bacteria *E. coli*, *Klebsiella pneumoniae*, and *Salmonella*. The inhibitory activity was measured based on the diameter of the clear inhibition zone. If there was no surrounding clear zone, it was assumed that there was no inhibitory zone. Contact area was used to evaluate growth inhibition underneath. The zones of inhibition around pieces of AgNPs, pure PS film, and AgNPs/PS nanocomposite film for bacterial culture are shown in Figure 6(a) while numerical values of diameter of inhibition zones were compiled in Figure 6(b). The results exhibited very high toxicity against gram negative bacteria *Escherichia coli* and *Salmonella*, low toxicity against *Klebsiella*

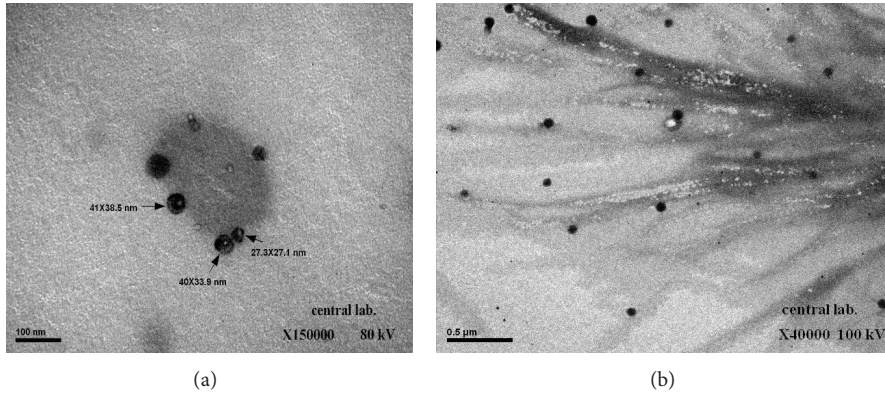


FIGURE 3: TEM image of AgNPs and AgNPs/PS nanocomposite from (a) to (b).

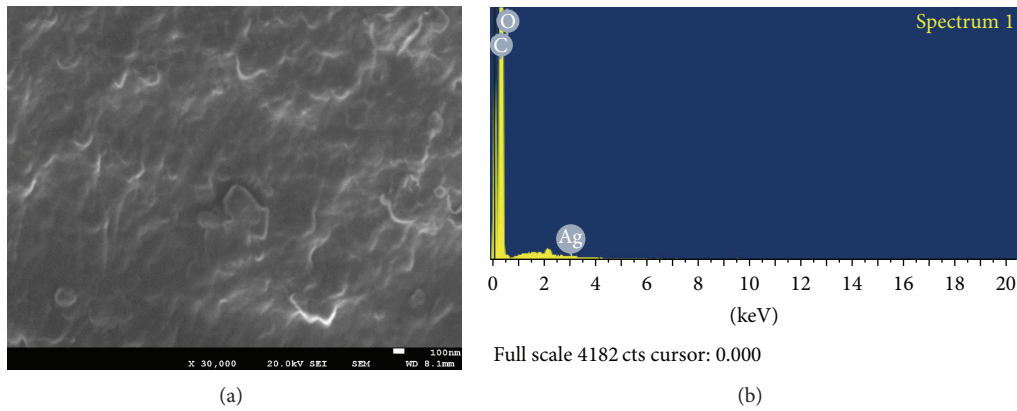


FIGURE 4: SEM and EDS analysis of AgNPs/SP nanocomposite film.

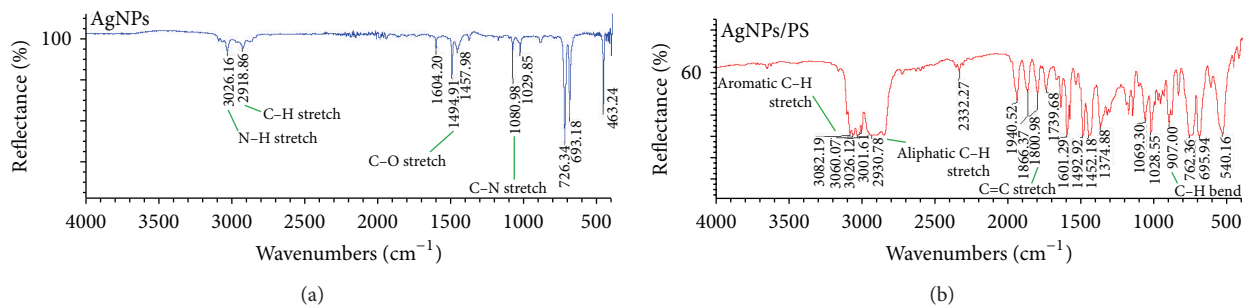


FIGURE 5: Fourier transform infrared spectra analysis for (a) AgNPs and (b) AgNPs/PS nanocomposite.

pneumoniae, and lower toxicity against gram positive bacteria *Staphylococcus aureus*. The presence of green AgNPs from the nanocomposite explains the antimicrobial properties found in the prepared nanocomposite. In addition to this, the antimicrobial properties that have been exhibited in our results are similar to Morones et al. [13] who reported that small size nanoparticles may pass through cell membranes generating cell malfunction [14]. It can be concluded that the nanocomposite (green AgNPs/PS) that has been prepared is an effective agent against Gram-negative and Gram-positive bacteria (which is our case), taking into account that

the nanoparticles are uniformly dispersed in the polyethylene matrix.

In general, the mechanism of the inhibitory effects of Ag ions on microorganisms is partially known. Some studies have reported that the positive charge on the Ag ion is crucial for its antimicrobial activity through the electrostatic attraction between the negative charge on the cell membrane of microorganism and positively charged nanoparticles [15–17]. In contrast, Dragieva et al. [18] reported that the antimicrobial activity of silver nanoparticles on Gram-negative bacteria was dependent on the concentration of Ag nanoparticle and

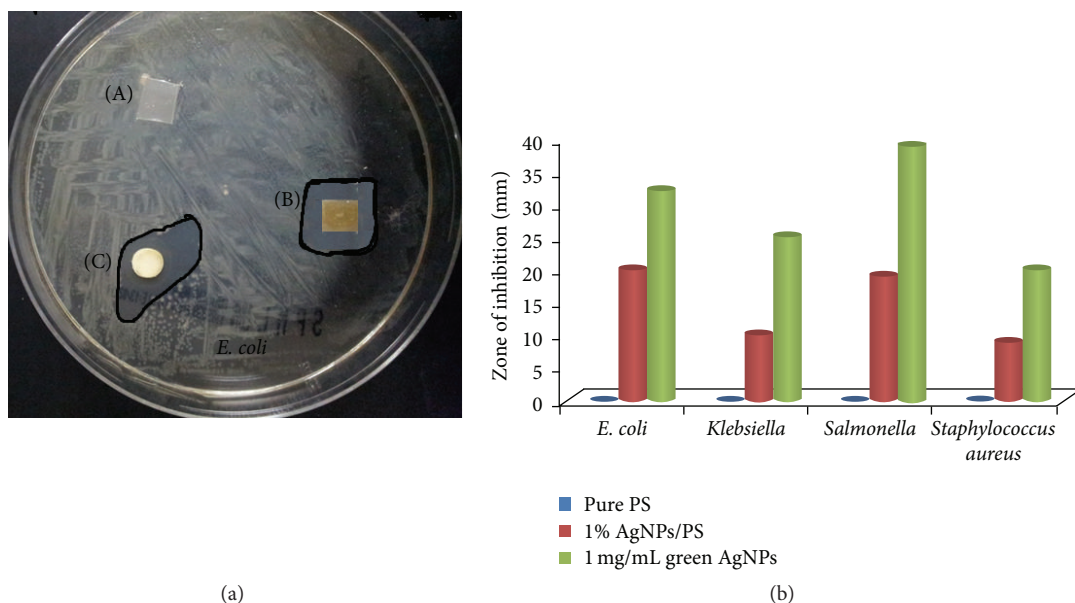


FIGURE 6: (a) Antibacterial activity assay of (A) pure PS film, (B) green AgNPs/PS nanocomposite film, and (C) green AgNPs and (b) diagram for the antibacterial activity.

was closely associated with the formation of the pits in the cell wall of bacteria. Ag nanoparticles accumulated in the bacterial membrane caused a change in the permeability, resulting in cell death. However, these studies included both positively charged Ag ions and negatively charged Ag nanoparticles; it does not explain the antimicrobial mechanism of only the positively charged Ag nanoparticles. Therefore, we expect that there is another possible mechanism. Amro et al., 2000, suggested that metal depletion may cause the formation of irregularly shaped pits in the outer membrane and change membrane permeability, which is caused by progressive release of lipopolysaccharide molecules and membrane proteins [19]. Also, Dragieva et al. speculate that a similar mechanism may cause the degradation of the membrane structure of *E. coli* during treatment with Ag nanoparticles [18]. Although the interference mechanism of AgNPs and bacteria involve some sort of binding mechanism, the level of that interaction between AgNPs and component(s) of the outer bacterial membrane is still not well understood.

Hence, this facile approach for synthesis of green AgNPs-PS nanocomposite film can be useful in a wide range of biomedical products, such as surgical gloves, antibacterial cloths and towels, anti-infectious urinary catheters, bandage, food packaging, water container, and industrial applications. The method has been distinguished as a method which allows the use of nontoxic, abundant ecofriendly bioavailable material which is energy saving and low cost.

4. Conclusion

The synthesis of nanocomposite film showed significant antibacterial activity on both Gram-positive and Gram-negative bacteria. This promises a potential use of the nanocomposite

in the pharmaceutical, biomedical, and industrial fields, such as bandages, wounds dressing, and dental tools. In addition, the applications include also food and water storage as well as wastewater treatment.

Highlights

- (i) Silver/polystyrene nanocomposite is a novel approach.
- (ii) *Orange peel* is extracted by toluene as a reducing agent.
- (iii) Ecofriendly silver/polystyrene nanocomposite showed highly effective antibacterial activity towards Gram-positive and Gram-negative bacteria.

Conflict of Interests

The authors declare that there is no conflict of interests regarding the publication of this paper.

Acknowledgment

The authors extend their appreciation to the Deanship of Scientific Research at King Saud University for funding this work through research group no. RGP-VPP-278.

References

- [1] E. Amato, Y. A. Diaz-Fernandez, A. Taglietti et al., "Synthesis, characterization and antibacterial activity against gram positive and gram negative bacteria of biomimetically coated silver nanoparticles," *Langmuir*, vol. 27, no. 15, pp. 9165–9173, 2011.

- [2] P. Pallavicini, A. Taglietti, G. Dacarro et al., "Self-assembled monolayers of silver nanoparticles firmly grafted on glass surfaces: low Ag^+ release for an efficient antibacterial activity," *Journal of Colloid and Interface Science*, vol. 350, no. 1, pp. 110–116, 2010.
- [3] P. Dallas, V. K. Sharma, and R. Zboril, "Silver polymeric nanocomposites as advanced antimicrobial agents: classification, synthetic paths, applications, and perspectives," *Advances in Colloid and Interface Science*, vol. 166, no. 1-2, pp. 119–135, 2011.
- [4] D. R. Deshmukh and R. J. Composto, "Surface segregation of silver nanoparticles in the in-situ synthesized Ag/PMMA nanocomposites," in *Proceedings of the Bulletin of the American Physical Society*, Baltimore, Md, USA, March 2006.
- [5] C. Damm and H. Münstedt, "Kinetic aspects of the silver ion release from antimicrobial polyamide/silver nanocomposites," *Applied Physics A*, vol. 91, no. 3, pp. 479–486, 2008.
- [6] M. Jokar, R. Abdul Rahman, N. A. Ibrahim, L. C. Abdullah, and C. P. Tan, "Melt production and antimicrobial efficiency of low-density polyethylene (LDPE)-silver nanocomposite film," *Food and Bioprocess Technology*, vol. 5, no. 2, pp. 719–728, 2012.
- [7] Y. M. Mohan, T. Premkumar, K. Lee, and K. E. Geckeler, "Fabrication of silver nanoparticles in hydrogel networks," *Macromolecular Rapid Communications*, vol. 27, no. 16, pp. 1346–1354, 2006.
- [8] T. B. Karchmer, E. T. Giannetta, C. A. Muto, B. A. Strain, and B. M. Farr, "A randomized crossover study of silver-coated urinary catheters in hospitalized patients," *Archives of Internal Medicine*, vol. 160, no. 21, pp. 3294–3298, 2000.
- [9] C. Marambio-Jones and E. M. V. Hoek, "A review of the antibacterial effects of silver nanomaterials and potential implications for human health and the environment," *Journal of Nanoparticle Research*, vol. 12, no. 5, pp. 1531–1551, 2010.
- [10] S. Tripathi, G. K. Mehrotra, and P. K. Dutta, "Chitosan-silver oxide nanocomposite film: preparation and antimicrobial activity," *Bulletin of Materials Science*, vol. 34, no. 1, pp. 29–35, 2011.
- [11] L. Timochenco, G. V. Grassi, M. Dal Pizzol et al., "Swelling of organoclays in styrene. Effect on flammability in polystyrene nanocomposites," *Express Polymer Letters*, vol. 4, no. 8, pp. 500–508, 2011.
- [12] R. P. Singh, A. Tiwari, and A. C. Pandey, "Silver/polyaniline nanocomposite for the electrocatalytic hydrazine oxidation," *Journal of Inorganic and Organometallic Polymers and Materials*, vol. 21, no. 4, pp. 788–792, 2011.
- [13] J. R. Morones, J. L. Elechiguerra, A. Camacho et al., "The bactericidal effect of silver nanoparticles," *Nanotechnology*, vol. 16, no. 10, pp. 2346–2353, 2005.
- [14] O. Choia, K. K. Deng, N.-J. Kim, L. Ross Jr., R. Y. Surampalli, and Z. Hu, "The inhibitory effects of silver nanoparticles, silver ions, and silver chloride colloids on microbial growth," *Water Research*, vol. 42, no. 12, pp. 3066–3074, 2008.
- [15] T. Hamouda, A. Myc, B. Donovan, A. Y. Shih, J. D. Reuter, and J. R. Baker Jr., "A novel surfactant nanoemulsion with a unique non-irritant topical antimicrobial activity against bacteria, enveloped viruses and fungi," *Microbiological Research*, vol. 156, no. 1, pp. 1–7, 2000.
- [16] I. Sondi, B. Salopek-Sondi, S. D. Škapin, S. Šegota, I. Jurina, and B. Vukelić, "Colloid-chemical processes in the growth and design of the bio-inorganic aragonite structure in the scleractinian coral *Cladocora caespitosa*," *Journal of Colloid and Interface Science*, vol. 354, no. 1, pp. 181–189, 2011.
- [17] P. Dibrov, J. Dzioba, K. K. Gosink, and C. C. Häse, "Chemiosmotic mechanism of antimicrobial activity of Ag^+ in *Vibrio cholerae*," *Antimicrobial Agents and Chemotherapy*, vol. 46, no. 8, pp. 2668–2670, 2002.
- [18] I. Dragieva, S. Stoeva, P. Stoimenov, E. Pavlikianov, and K. Klabunde, "Complex formation in solutions for chemical synthesis of nanoscaled particles prepared by borohydride reduction process," *Nanostructured Materials*, vol. 12, no. 1–4, pp. 267–270, 1999.
- [19] N. A. Amro, L. P. Kotra, K. Wadu-Mesthrige, A. Bulychev, S. Mobashery, and G. Liu, "High-resolution atomic force microscopy studies of the *Escherichia coli* outer membrane: structural basis for permeability," *Langmuir*, vol. 16, no. 6, pp. 2789–2796, 2000.

Research Article

Composite Scaffolds Based on Silver Nanoparticles for Biomedical Applications

Jenel Marian Patrascu,¹ Ioan Avram Nedelcu,² Maria Sonmez,³ Denisa Ficai,²
Anton Ficai,² Bogdan Stefan Vasile,² Camelia Ungureanu,² Madalina Georgiana Albu,³
Bogdan Andor,¹ Ecaterina Andronescu,² and Laura Cristina Rusu⁴

¹Department of Orthopaedics, Traumatology, Urology and Imaging, Faculty of Medicine, “Victor Babeş” University of Medicine and Pharmacy Timișoara, P-ța Eftimie Murgu, No. 2, 300041 Timișoara, Romania

²Faculty of Applied Chemistry and Material Science, Politehnica University of Bucharest, 1-7 Polizu Street, 011061 Bucharest, Romania

³Collagen Department, Leather and Footwear Research Institute, 93 Ion Minulescu, 031215 Bucharest, Romania

⁴Department of Technology of Materials and Devices in Dental Medicine, “Victor Babeş” University of Medicine and Pharmacy Timișoara, P-ța Eftimie Murgu, No. 2, 300041 Timișoara, Romania

Correspondence should be addressed to Madalina Georgiana Albu; albu_mada@yahoo.com

Received 12 January 2015; Revised 19 February 2015; Accepted 25 February 2015

Academic Editor: Bin Li

Copyright © 2015 Jenel Marian Patrascu et al. This is an open access article distributed under the Creative Commons Attribution License, which permits unrestricted use, distribution, and reproduction in any medium, provided the original work is properly cited.

This paper presents the synthesis, characterisation, and *in vitro* testing of homogenous and heterogeneous materials containing silver nanoparticles (nanoAg). Three types of antiseptic materials based on collagen (COLL), hydroxyapatite (HA), and collagen/hydroxyapatite (COLL/HA) composite materials were obtained. The synthesis of silver nanoparticles was realized by chemical reaction as well as plasma sputtering deposition. The use of chemical reduction allows the synthesis of homogenous materials while the plasma sputtering deposition can be easily used for the synthesis of homogeneous and heterogeneous support. Based on the *in vitro* assays clear antiseptic activity against *Escherichia coli* was relieved even at low content of nanoAg (10 ppm).

1. Introduction

Silver nanoparticles are of increasing interest for scientists due to their very good biological properties and limited side effects. Used since 1000 BC, silver proved its biocidal activity for a wide number of bacteria and recently it was also known to be active in the treatment of cancer [1]. As a consequence of silver multifunctionality (antiseptic [2], antitumoral [3, 4], and IR-sensitizing agent [5]) the number of published papers dealing with silver nanoparticles increases exponentially yearly, at present over 10 000 papers [6] being indexed on SCOPUS database. The distribution of the published papers, per year, can be visualized in Figure 1.

Silver nanoparticles are widely used for their biological activity as colloidal suspension [7–10] or in association with other materials [11–14]. Silver nanoparticles were associated

with different components such as manganite [15], carbon nanotubes [16], hydroxyapatite [17, 18], and chitosan [19]. Mostly, silver nanoparticles play antibacterial [17] and antitumoral [3] role.

Collagen is widely used for many biomedical applications [20–22]. Adding of calcium phosphates to collagen resulted in composite materials which proved to be remarkable bone grafts [23–31]. A common shortcoming of these grafts is related to the high incidence of infection [32]. Most surgical interventions involve antibiotic administration [33] which could be avoided by using silver nanoparticles [10, 34, 35].

In the case of bone cancer, many times surgical resection is necessary. In order to treat bone cancer the multifunctional COLL/HA-Fe₃O₄ composite materials were proposed. The composite support assures a faster healing of the bone defect while magnetite can assure the necessary hyperthermia to

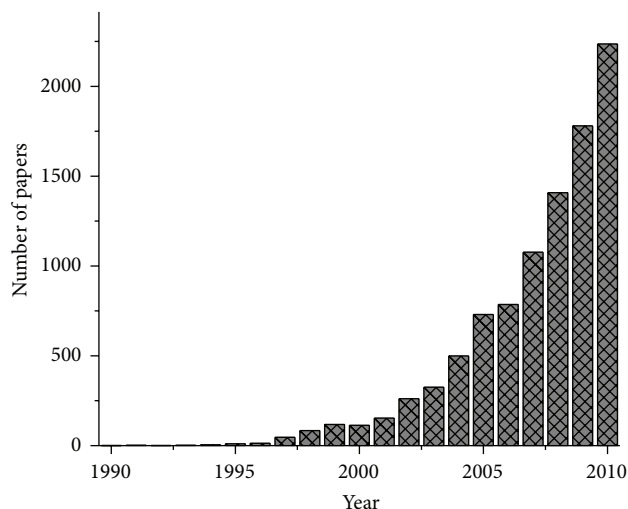


FIGURE 1: The evolution of the number of papers dealing with “silver nanoparticles.”

induce tumoral cells death. It is also important to mention that magnetite can be activated, any time, by applying a proper, external electromagnetic field [36].

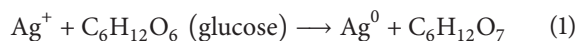
The current paper presents the synthesis and characterisation of new antiseptic materials based on silver nanoparticles embedded in collagen, hydroxyapatite, or collagen/hydroxyapatite composite material. Silver nanoparticles were synthesised by two different methods: chemical reduction and plasma sputtering. The obtained materials are intended to be used as bone grafts.

2. Materials and Methods

Type I fibrillar collagen (C) gel having about 300000 Da, concentration of 1.6% (w/w), and pH 7.4 was extracted from calf hide as previously described [20, 25].

Antiseptic collagen sponge was obtained by chemical reduction of Ag^+ in the presence of glucose and by plasma sputtering of Ag nanoparticles onto the collagen sponge. In both cases collagen sponge was obtained by cross-linking of the collagen gel with glutaraldehyde. For cross-linking 0.5% glutaraldehyde, reported to dry collagen, was used.

The reduction of Ag^+ occurs in the presence of glucose which undergoes an oxidation process as presented in the following reaction:



Antiseptic HA powder was also obtained by the same two methods starting from HA powder obtained by coprecipitation from $\text{Ca}(\text{OH})_2$ and NaH_2PO_4 [23].

The antiseptic composite materials were obtained by a similar way as antiseptic collagen sponge but starting from mineralized collagen gel and COLL/HA composite sponges, respectively.

The COLL/HA composite material was synthesised as we described in our previously published papers [25, 37]. Briefly, the collagen gel (when plasma sputtering method is used)

or silver containing collagen gel (when chemical method is used) was neutralized with $\text{Ca}(\text{OH})_2$ 24 h and then the proper amount of NaH_2PO_4 was added and let for other 24 h to interact. During these steps which lead to the HA nucleation on the collagen, the pH was set at 9. The final steps consist in cross-linking followed by freeze-drying.

Plasma sputtering of silver nanoparticles was realised using a BAL-TEC SCD005 Sputter Coater with nitrogen plasma and the deposition current was 59 mA while the deposition time was set at 60 s.

The obtained materials were investigated by X-ray diffraction, IR spectroscopy, scanning electron microscopy, transmission electron microscopy, and antimicrobial activity against *Escherichia coli*.

X-ray diffraction analysis was performed using a Shimadzu XRD 6000 diffractometer at room temperature. In all the cases, $\text{Cu K}\alpha$ radiation from a Cu X-ray tube was used. The samples were scanned in the Bragg angle, 2θ range of 10–70.

For IR spectroscopy (Shimadzu 8400 FTIR Spectrometer) measurements, the spectra were recorded in the wavenumber range of 400–4000 cm^{-1} , with a resolution of 2 cm^{-1} .

SEM analyses were performed on a HITACHI S2600N electron microscope on samples covered with silver layer.

The transmission electron images were obtained on finely powdered samples using a Tecnai G² F30 S-TWIN high resolution transmission electron microscope (HRTEM) equipped with STEM-HAADF detector, EDX, and EELS. The microscope was operated in transmission mode at 300 kV while TEM point resolution was 2 Å and line resolution was 1 Å.

The antibacterial activity was evaluated in triplicate against *Escherichia coli*. *Escherichia coli* (K 12-MG1655) were cultured in a tube containing Luria-Bertani (LB) medium [38] at 37°C (LB medium composition: peptone, 10 g/L; yeast extract 5 g/L, NaCl 5 g/L). Sterile samples were incubated for 18 hours in test tubes containing 5 mL culture of *Escherichia coli*. Culture was obtained from a volume of 100 mL sterile culture medium. The sterile medium was inoculated with 1 mL of *Escherichia coli* (1%). Once obtained 5 mL of culture was placed over the samples. Optical density was determined after 18 hours of incubation. Incubation was performed in the incubator Laboshake Gerhardt. The bacterial growth was determined by measuring optical density for the four samples and control (*Escherichia coli* culture without sample) at 600 nm using UV-VIS spectrophotometer (Jenway Spectrophotometer).

The antibacterial activities were determined by calculating the inhibition of growth using [39]

$$I\% = \frac{[(B_{18} - B_0) - (C_{18} - C_0)]}{(B_{18} - B_0)} \cdot 100, \quad (2)$$

where I is the inhibition of growth, %, B_{18} is the blank-compensated optical density at 600 nm ($\text{OD}_{600} = 3.36$ of the positive control of the organism at 18 h), B_0 is the blank-compensated OD_{600} of the positive control of the organism at 0 h ($\text{OD}_{600} = 0.049$), C_{18} is the negative control-compensated OD_{600} of the organism in the presence of test sample at 18 h, and C_0 is the negative control-compensated OD_{600} of the organism in the presence of test sample at 0 h.

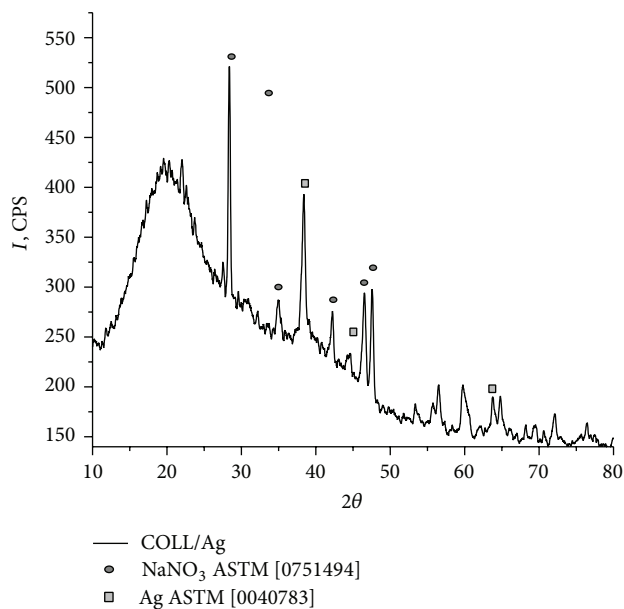


FIGURE 2: XRD pattern of COLL/Ag antiseptic composite materials.

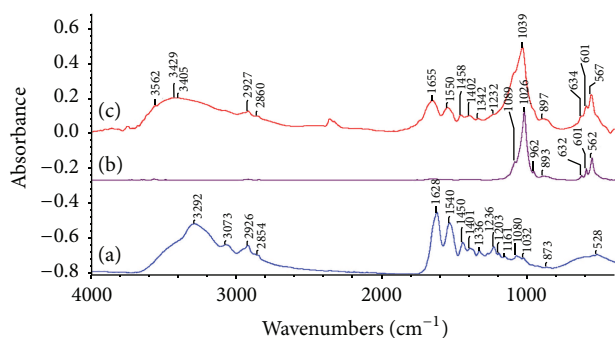


FIGURE 3: FTIR spectra of (a) COLL/Ag, (b) HA-Ag, and (c) COLL/HA-Ag antiseptic materials.

3. Results and Discussion

The antiseptic materials were characterized by appropriate methods.

3.1. X-Ray Diffraction. X-ray diffraction pattern was used to prove the formation of the AgNPs regardless of the synthesis method as we presented in Figure 2. Silver was identified based on the ASTM file number 0040783. Sodium nitrate was identified as a secondary crystalline phase, its presence being explained based on the collagen extraction technology.

3.2. Infrared Spectroscopy. The three FTIR spectra reveal the absorption bands of the components except the AgNPs which appear far below the lower limit of wavelength of the spectrophotometer as Figure 3 showed.

The main absorption band of HA appears as follows, a triple degenerate band associated with the O-P-O band at 560, 600, and 630 cm^{-1} ; a triple degenerate band at 1030, 1090, and 1110 cm^{-1} ; and a band associated with a symmetric stretch

of P-O band at 960 cm^{-1} , while the main absorption bands of collagen appear at 1628 (amide I), 1540 (amide II), 1236 (amide III), 2854 (CH_2 asymmetric stretching), 2926 (CH_2 symmetric stretching), and 2957 (CH_3 symmetric stretching). The wide band from 3000 to 3600 cm^{-1} corresponds to the associated hydroxyl groups from collagen, hydroxyapatite, and water.

3.3. Scanning Electron Microscopy. The silver particles cannot be identified by SEM images because of their low content and nanosize into the collagen composites (Figure 4). At 2000 and 3,500x magnification, the COLL/HA-Ag sample presents agglomerations which can be easily assigned to the inorganic, hydroxyapatite phase [24]. This observation is also supported by the comparison with the COLL/Ag sample (Figures 4(a')–4(c')) where no agglomerations can be identified. Silver visualization will be possible at higher magnification using TEM or HRTEM. That is why only in the case of COLL/HA-Ag composite material agglomerates can be visualised on the collagenic matrices, these agglomerates being clearly identified on the collagenic matrix at a magnification of 2000x while in the case of COLL/Ag material no agglomerations can be identified at this magnification.

Scanning electron microscopy was also used for the characterization of HA-Ag nanopowder (Figure 5). Based on the micrographs, it can be seen that nanometric particles were obtained. The size and shape are difficult to determine based on the SEM images and consequently TEM will be further used to evaluate the size and to determine the shape of these nanoparticles.

3.4. Transmission Electron Microscopy. TEM analysis was performed on pure silver nanoparticles obtained by plasma sputtering (Figure 6), COLL/Ag sample obtained by plasma sputtering (Figure 7), and HA-Ag nanopowder obtained by HA precipitation and chemical reduction of Ag^+ (Figure 8). In the case of pure silver nanoparticles obtained by plasma sputtering nanoAg agglomerates can be identified. From the point of view of particle size distribution very small particles with 1–2 nm as well as oversized particles with about 10–20 nm diameter can be visualized. The characteristic silver bands can be identified in SAED as well as silver oxide which means that during the deposition silver is partially oxidized to silver oxide.

In the case of COLL/Ag antiseptic sample, due to the collagen harsh matrix the silver is more uniformly deposited, the particles having generally 2–4 nm diameter.

Analyzing Figure 7, it can be seen that practically the particles are independent which means that collagen matrix acts as a dispersing agent and does not allow the silver nanoparticles to form agglomerates.

In the case of HA-Ag sample both HA and Ag can be identified based on their different contrast or based on their interplanar distances. At low magnification a severe agglomeration of the silver nanoparticles (darker nanoparticles) is noticed while, at high resolution characteristic planes of HA and Ag demonstrate their presence. Comparing with the COLL/Ag sample, the HA-Ag is less homogeneous because,

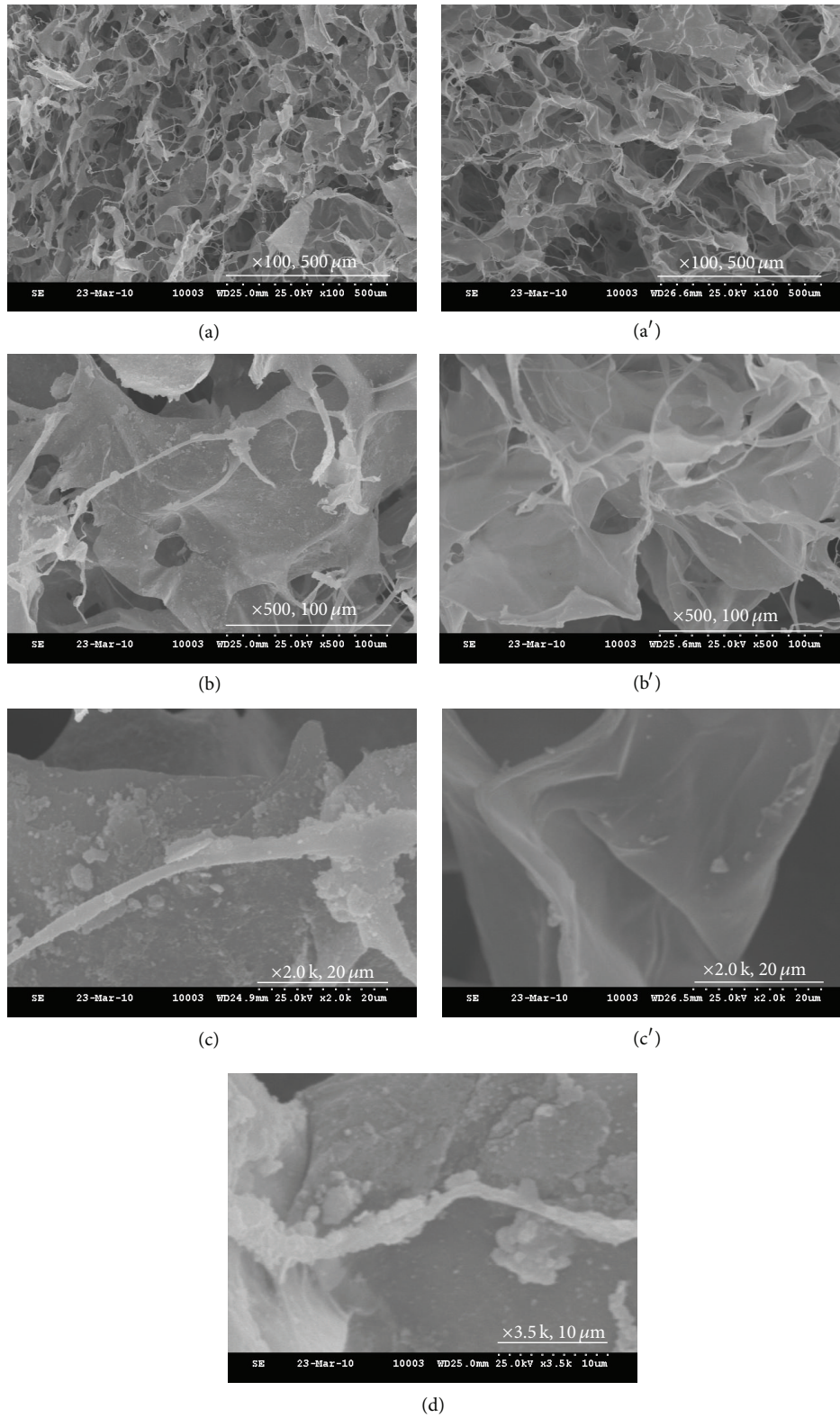


FIGURE 4: SEM images of (a)–(d) COLL/HA-Ag nanocomposite and (a')–(c') COLL/Ag.

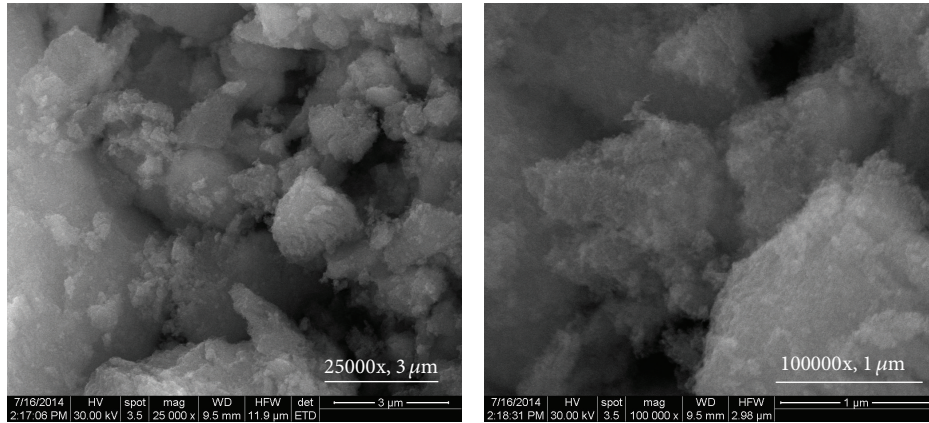


FIGURE 5: SEM image of HA-Ag nanopowder.

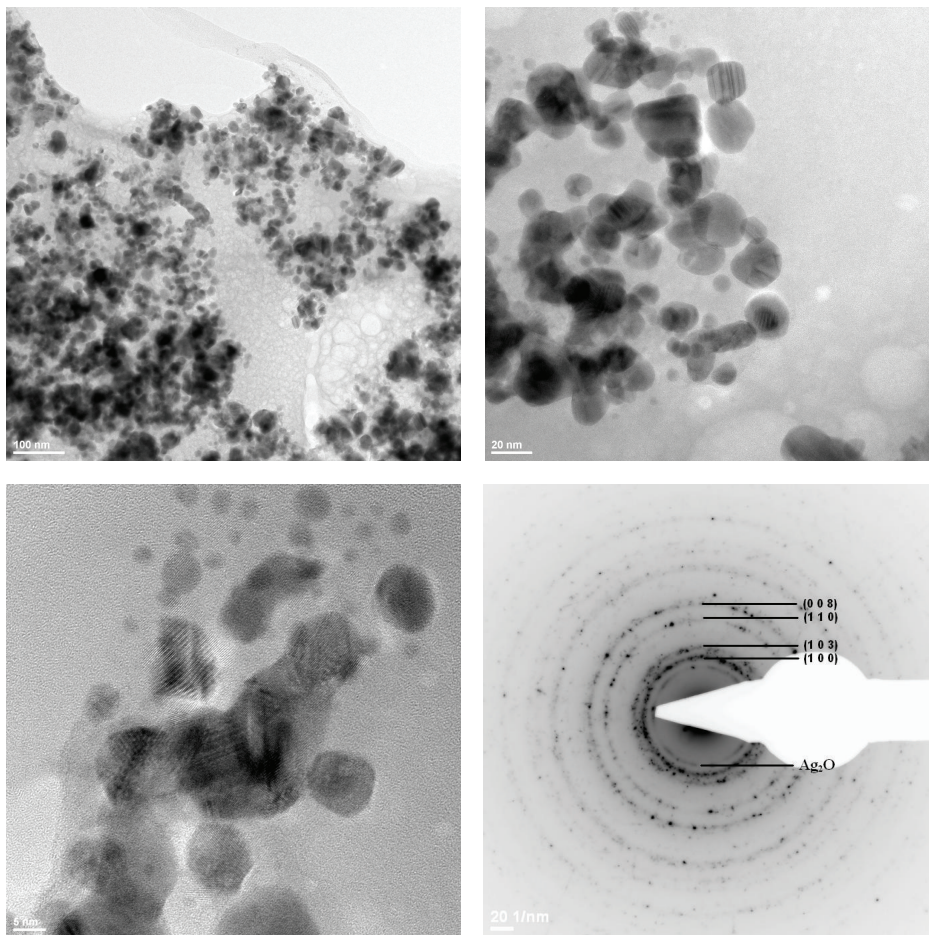


FIGURE 6: TEM images of plasma sputtered silver nanoparticles.

in the bulk nanopowder, it is possible to identify silver-rich areas (containing silver agglomerates) but also silver-free areas (pure HA). Based on TEM image, silver as well as HA can be considered monodisperse, silver having spherical form and a maximum diameter of less than 20 nm.

3.5. Antimicrobial Studies. As found in the literature data, the antimicrobial activity is dependent on concentration, silver size, and shape [40]. Because only for the HA-Ag sample different compositions were obtained, the antimicrobial studies will be presented only for HA/Ag samples obtained by

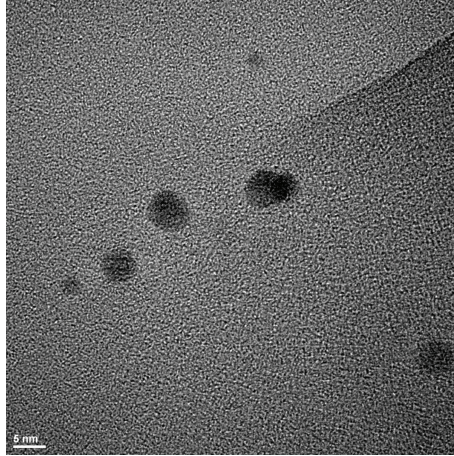


FIGURE 7: TEM image of the antiseptic COLL/Ag matrix.

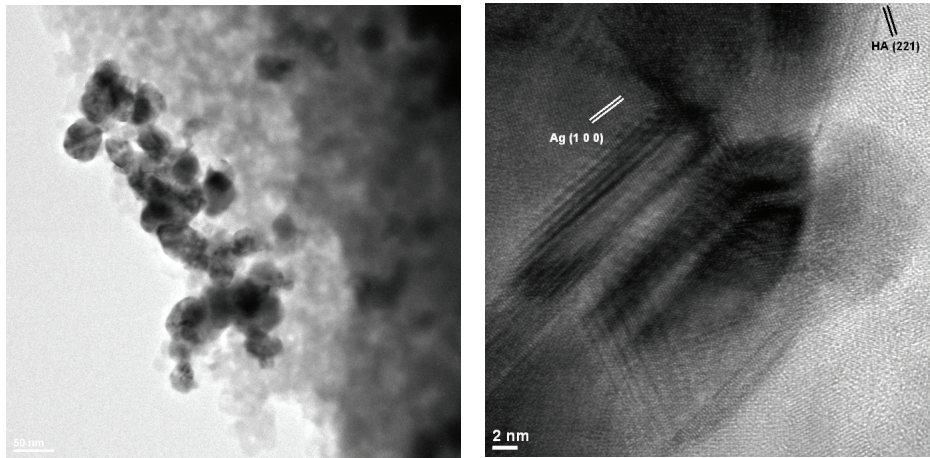


FIGURE 8: TEM images of HA-Ag powder.

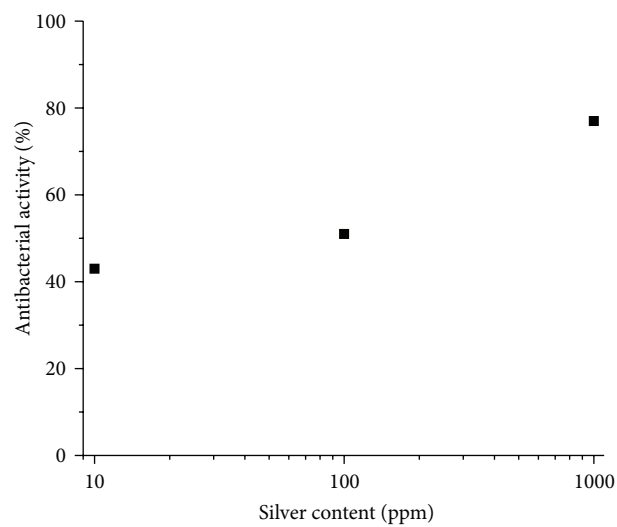


FIGURE 9: Antibacterial activity of the HA-Ag samples.

TABLE 1: Potential applications of the synthesized samples.

Materials	Synthesis method	Potential applications
Colloidal silver	Chemical reduction	Treatment of different infections (equivalent of antibiotics) or even cancer and so forth
	Chemical reduction	Skin cancer or burns (not recommended in the case of infections because glucose and its derivatives could serve as a growth medium)
COLL/Ag	PS symmetric	Skin cancer, infections associated with burns (can be used also for the people with diabetes)
	PS asymmetric	Skin cancer/infections (silver-rich face is in contact with the skin); burns (silver-rich face is not in contact with the skin; Ag nanoparticles are only for their antiseptic activity)
HA/Ag or COLL/HA-Ag	Chemical reduction	Treatment of bone defects and even for bone cancer (Ag nanoparticles have antitumoral activity and antiseptic activity, respectively)
	PS symmetric	
	PS asymmetric	Treatment of bone defects and bone cancer (silver-rich face has to be in contact with cancerous tissue due to its antitumoral and antiseptic activity)

plasma sputtering and containing 10, 100, and 1000 ppm silver nanoparticles. The bacteriological experiments performed *in vitro* demonstrated the effectiveness of these samples in inhibiting the growth of *Escherichia coli* (Figure 9), even at low silver content.

It can be concluded that even at low content of silver nanoparticles (10 ppm), the HA-Ag sample inhibits the growth of *E. coli* (43%) while increasing content of silver induces a higher level of antimicrobial activity (51% for 100 ppm and 77% for 1000 ppm of nanoAg, resp.).

Based on the presented results these materials are intended to be further tested for the following applications, as presented in Table 1.

4. Conclusions

Three types of antiseptic, multifunctional materials were obtained, each having different potential medical applications. COLL/nanoAg is potential material for skin repair and can be used especially for the injuries caused by burns or cancer. HA/nanoAg and COLL/HA-nanoAg are potential bone grafts antiseptic materials but can be also used in different kinds of bone cancer, where surgical resection is necessary. Besides the material, in the cases of infections or tumours the silver-rich face of the materials has to be in contact with these tissues. When only antiseptic activity is required both symmetric (homogenous) and asymmetric materials can be used. In the cases of skin injuries it is recommended to use asymmetric COLL/Ag scaffolds and the silver-rich face does not have to be in contact with the skin, having only protective role for potential infections.

Conflict of Interests

The authors declare no conflict of interests.

Acknowledgments

This paper was supported by the PN-II-PT-PCCA-2011-3.2-0284: "Novel Nanostructured Prosthetic Tubular Devices with Antibacterial and Antibiofilm Properties Induced by

Physicochemical and Morphological Changes," funded by the National University Research Council in Romania.

References

- [1] F. G. Rutberg, M. V. Dubina, V. A. Koliakov et al., "Effect of silver oxide nanoparticles on tumor growth *in vivo*," *Doklady Biochemistry and Biophysics*, vol. 421, no. 1, pp. 191–193, 2008.
- [2] S.-L. Peng, D.-X. Chen, G. Su, Z. Wang, Y. H. Xiao, and Z. L. Liu, "Application of nanometer silver antiseptic dressing for wound surface in children after urinary surgery," *Journal of Clinical Rehabilitative Tissue Engineering Research*, vol. 11, no. 40, pp. 8181–8183, 2007.
- [3] M. I. Sriram, S. B. M. Kanth, K. Kalishwaralal, and S. Gurunathan, "Antitumor activity of silver nanoparticles in Dalton's lymphoma ascites tumor model," *International Journal of Nanomedicine*, vol. 5, no. 1, pp. 753–762, 2010.
- [4] M. Rahban, A. Divsalar, A. A. Saboury, and A. Golestani, "Nanotoxicity and spectroscopy studies of silver nanoparticle: calf thymus DNA and K562 as targets," *Journal of Physical Chemistry C*, vol. 114, no. 13, pp. 5798–5803, 2010.
- [5] R. Xu, J. Ma, X. Sun et al., "Ag nanoparticles sensitize IR-induced killing of cancer cells," *Cell Research*, vol. 19, no. 8, pp. 1031–1034, 2009.
- [6] Scopus Database, <http://www.scopus.com>.
- [7] W. Zhang, X. Qiao, and J. Chen, "Synthesis of nanosilver colloidal particles in water/oil microemulsion," *Colloids and Surfaces A: Physicochemical and Engineering Aspects*, vol. 299, no. 1–3, pp. 22–28, 2007.
- [8] A. R. Shahverdi, A. Fakhimi, H. R. Shahverdi, and S. Minaian, "Synthesis and effect of silver nanoparticles on the antibacterial activity of different antibiotics against *Staphylococcus aureus* and *Escherichia coli*," *Nanomedicine: Nanotechnology, Biology, and Medicine*, vol. 3, no. 2, pp. 168–171, 2007.
- [9] W. Zhang, X. Qiao, J. Chen, and H. Wang, "Preparation of silver nanoparticles in water-in-oil aot reverse micelles," *Journal of Colloid and Interface Science*, vol. 302, no. 1, pp. 370–373, 2006.
- [10] V.-S. Manoiu and A. Aloman, "Obtaining silver nanoparticles by sonochemical methods," *UPB Scientific Bulletin, Series B: Chemistry and Materials Science*, vol. 72, no. 2, pp. 179–186, 2010.
- [11] H. V. Tran, L. D. Tran, C. T. Ba et al., "Synthesis, characterization, antibacterial and antiproliferative activities of monodisperse chitosan- based silver nanoparticles," *Colloids*

- and Surfaces A: Physicochemical and Engineering Aspects*, vol. 360, no. 1–3, pp. 32–40, 2010.
- [12] L.-H. Li, J.-C. Deng, H.-R. Deng, Z.-L. Liu, and X.-L. Li, “Preparation, characterization and antimicrobial activities of chitosan/Ag/ZnO blend films,” *Chemical Engineering Journal*, vol. 160, no. 1, pp. 378–382, 2010.
 - [13] C. Zhang, Q. Yang, N. Zhan et al., “Silver nanoparticles grown on the surface of PAN nanofiber: preparation, characterization and catalytic performance,” *Colloids and Surfaces A: Physicochemical and Engineering Aspects*, vol. 362, no. 1–3, pp. 58–64, 2010.
 - [14] F. Zeng, C. Hou, S. Wu, X. Liu, Z. Tong, and S. Yu, “Silver nanoparticles directly formed on natural macroporous matrix and their anti-microbial activities,” *Nanotechnology*, vol. 18, no. 5, Article ID 055605, 2007.
 - [15] O. V. Melnikov, O. Y. Gorbenko, M. N. Märkelova et al., “Ag-doped manganite nanoparticles: new materials for temperature-controlled medical hyperthermia,” *Journal of Biomedical Materials Research, Part A*, vol. 91, no. 4, pp. 1048–1055, 2009.
 - [16] C.-S. Wu, C.-Y. Lee, J.-K. Chen et al., “Microwave-assisted electrodeless deposition of silver nanoparticles onto multiwalled carbon nanotubes,” *International Journal of Electrochemical Science*, vol. 7, no. 5, pp. 4133–4142, 2012.
 - [17] C. S. Ciobanu, S. L. Iconaru, P. Le Coustumer, L. V. Constantin, and D. Predoi, “Antibacterial activity of silver-doped hydroxyapatite nanoparticles against gram-positive and gram-negative bacteria,” *Nanoscale Research Letters*, vol. 7, article 324, 2012.
 - [18] C. S. Ciobanu, S. L. Iconaru, P. le Coustumer, and D. Predoi, “Vibrational investigations of silver-doped hydroxyapatite with antibacterial properties,” *Journal of Spectroscopy*, vol. 2013, Article ID 471061, 5 pages, 2013.
 - [19] M. A. Hettiarachchi and P. A. S. R. Wickramarachchi, “Synthesis of chitosan stabilized silver nanoparticles using gamma ray irradiation and characterization,” *Journal of Science—University of Kelaniya*, vol. 6, pp. 65–75, 2011.
 - [20] M. G. Albu, *Collagen Gels and Matrices for Biomedical Applications*, edited by E. Alexei, Lambert Academic Publishing, Saarbrücken, Germany, 2011.
 - [21] M. G. Albu, I. Titorencu, and M. V. Ghica, “Collagen-based drug delivery systems for tissue engineering,” in *Biomaterials Applications for Nanomedicine*, P. Rosario, Ed., chapter 17, InTech, Rijeka, Croatia, 2011.
 - [22] M. G. Albu, V. Trandafir, D. M. Suflet, G. C. Chitanu, P. Budrugaec, and I. Titorencu, “Biomaterials based on collagen and phosphorylated dextran for bone regeneration,” *Journal of Materials Research*, vol. 27, no. 7, pp. 1086–1096, 2012.
 - [23] A. Ficai, E. Andronescu, V. Trandafir, C. Ghitulica, and G. Voicu, “Collagen/hydroxyapatite composite obtained by electric field orientation,” *Materials Letters*, vol. 64, no. 4, pp. 541–544, 2010.
 - [24] A. Ficai, E. Andronescu, G. Voicu, and D. Ficai, “Advances in collagen/hydroxyapatite composite materials,” in *Advances in Composite Materials for Medicine and Nanotechnology*, B. Attaf, Ed., InTech, 2011.
 - [25] A. Ficai, E. Andronescu, G. Voicu et al., “Self-assembled collagen/hydroxyapatite composite materials,” *Chemical Engineering Journal*, vol. 160, no. 2, pp. 794–800, 2010.
 - [26] A. Ficai, E. Andronescu, G. Voicu, D. Manzu, and M. Ficai, “Layer by layer deposition of hydroxyapatite onto the collagen matrix,” *Materials Science & Engineering C—Materials for Biological Applications*, vol. 29, no. 7, pp. 2217–2220, 2009.
 - [27] A. Ilie, E. Andronescu, D. Ficai et al., “New approaches in layer by layer synthesis of collagen/hydroxyapatite composite materials,” *Central European Journal of Chemistry*, vol. 9, no. 2, pp. 283–289, 2011.
 - [28] D. I. Ilan and A. L. Ladd, “Bone graft substitutes,” *Operative Techniques in Plastic and Reconstructive Surgery*, vol. 9, no. 4, pp. 151–160, 2002.
 - [29] R. Murugan and S. Ramakrishna, “Development of nanocomposites for bone grafting,” *Composites Science and Technology*, vol. 65, no. 15–16, pp. 2385–2406, 2005.
 - [30] S. Bandyopadhyay-Ghosh, “Bone as a collagen-hydroxyapatite composite and its repair,” *Trends in Biomaterials and Artificial Organs*, vol. 22, no. 2, pp. 112–120, 2008.
 - [31] S. N. Parikh, “Bone graft substitutes: past, present, future,” *Journal of Postgraduate Medicine*, vol. 48, no. 2, pp. 142–148, 2002.
 - [32] B. H. Ziran, W. R. Smith, and S. J. Morgan, “Use of calcium-based demineralized bone matrix/allograft for nonunions and posttraumatic reconstruction of the appendicular skeleton: preliminary results and complications,” *The Journal of Trauma*, vol. 63, no. 6, pp. 1324–1328, 2007.
 - [33] D.-J. Yang, C.-D. Xiong, T. Govender, and Y.-Z. Wang, “Preparation and drug-delivery potential of metronidazole-loaded PELA tri-block co-polymeric electrospun membranes,” *Journal of Biomaterials Science, Polymer Edition*, vol. 20, no. 9, pp. 1321–1334, 2009.
 - [34] D. Dorjnamjin, M. Ariunaa, and Y. K. Shim, “Synthesis of silver nanoparticles using hydroxyl functionalized ionic liquids and their antimicrobial activity,” *International Journal of Molecular Sciences*, vol. 9, no. 5, pp. 807–820, 2008.
 - [35] V. K. Sharma, R. A. Yngard, and Y. Lin, “Silver nanoparticles: green synthesis and their antimicrobial activities,” *Advances in Colloid and Interface Science*, vol. 145, no. 1–2, pp. 83–96, 2009.
 - [36] E. Andronescu, M. Ficai, G. Voicu, D. Ficai, M. Maganu, and A. Ficai, “Synthesis and characterization of collagen/hydroxyapatite: magnetite composite material for bone cancer treatment,” *Journal of Materials Science: Materials in Medicine*, vol. 21, no. 7, pp. 2237–2242, 2010.
 - [37] A. Ficai, E. Andronescu, G. Voicu, C. Ghitulica, and D. Ficai, “The influence of collagen support and ionic species on the morphology of collagen/hydroxyapatite composite materials,” *Materials Characterization*, vol. 61, no. 4, pp. 402–407, 2010.
 - [38] M. A. Ansari, H. M. Khan, A. A. Khan et al., “Evaluation of antibacterial activity of silver nanoparticles against MSSA and MRSA on isolates from skin infections,” *Biology and Medicine*, vol. 3, no. 2, pp. 141–146, 2011.
 - [39] S. Jaiswal, B. Duffy, A. K. Jaiswal, N. Stobie, and P. McHale, “Enhancement of the antibacterial properties of silver nanoparticles using β -cyclodextrin as a capping agent,” *International Journal of Antimicrobial Agents*, vol. 36, no. 3, pp. 280–283, 2010.
 - [40] I.-A. Nedelcu, A. Ficai, M. Sonmez, D. Ficai, O. Oprea, and E. Andronescu, “Silver based materials for biomedical applications,” *Current Organic Chemistry*, vol. 18, no. 2, pp. 173–184, 2014.

Research Article

Ultradrawing and Ultimate Tenacity Properties of Ultrahigh Molecular Weight Polyethylene Composite Fibers Filled with Nanosilica Particles with Varying Specific Surface Areas

Jen-taut Yeh,^{1,2,3} Chuen-Kai Wang,² Lu-Kai Huang,² Chih-Chen Tsai,² and Wei-Yu Lai³

¹Hubei Collaborative Innovation Center for Advanced Organic Chemical Materials, Ministry of Education, Key Laboratory for the Green Preparation and Application of Functional Materials, Faculty of Materials Science and Engineering, Hubei University, Wuhan 430062, China

²Graduate School of Material Science and Engineering, National Taiwan University of Science and Technology, Taipei 10607, Taiwan

³Department of Materials Engineering, Kun Shan University, Tainan 71070, Taiwan

Correspondence should be addressed to Jen-taut Yeh; jyeh@mail.ntust.edu.tw

Received 14 April 2015; Revised 20 July 2015; Accepted 29 July 2015

Academic Editor: Bin Li

Copyright © 2015 Jen-taut Yeh et al. This is an open access article distributed under the Creative Commons Attribution License, which permits unrestricted use, distribution, and reproduction in any medium, provided the original work is properly cited.

Original and/or functionalized nanosilica particles with a quoted specific surface area of 100, 300, and 600 m²/g, respectively, were used to investigate the influence of specific surface areas of nanosilica particles on ultradrawing and ultimate tensile properties of ultrahigh molecular weight polyethylene (UHMWPE), UHMWPE/nanosilica, and UHMWPE/functionalized nanosilica fibers. The specific surface areas of well-dispersed functionalized nanosilica particles in UHMWPE/functionalized nanosilica fibers can positively affect their ultradrawing, orientation, ultimate tensile properties, and “micro-fibrils” morphologies. Excellent orientation and ultimate tensile properties of UHMWPE/nanofiller fibers can be prepared by ultradrawing the UHMWPE/functionalized nanosilica as-prepared fibers with optimal contents of the best prepared functionalized nanosilica particles well dispersing in the as-prepared fibers. The ultimate tensile strength value of the best prepared UHMWPE/functionalized nanosilica drawn fiber reaches 7.6 GPa, which is about 2.3 times of those of the best prepared UHMWPE drawn fiber without addition of any nanofiller. Specific surface area, morphological and Fourier transform infrared analyses of original and functionalized nanosilica particles, and/or investigations of thermal, orientation factor, and ultimate tensile properties of as-prepared and/or drawn UHMWPE/functionalized nanosilica fibers were performed to understand the above improved ultradrawing and ultimate tensile properties of the UHMWPE/functionalized nanosilica as-prepared and/or drawn fibers.

1. Introduction

As a kind of extremely significant and strategic material, ultrahigh molecular weight polyethylene (UHMWPE) fibers have attracted much attention for the last three decades, since they exhibit significantly higher tenacity but lower density values than those of other high performance fibers, such as carbon and aramid fibers [1–5]. Polyethylene fibers [1, 6–31] are typical high performance fibers produced using the gel spinning processing method from flexible polymer chains. Remarkable progress has been made in the improvement of these high performance fibers since then; however, the highest tensile strengths and moduli achieved for UHMWPE

fibers are still well below the broad range of theoretical tensile strengths and moduli reported for the UHMWPE perfect crystals [1]. The highest tenacity of commercially available UHMWPE fibers reaches as high as 45 g/den [32]; however, this obtained strength is still far below the theoretical achievable strength, 372 g/den reported for the perfect polyethylene crystal [16]. The key element in obtaining high-strength UHMWPE fibers is to find a way to draw the as-prepared gel specimens to an ultrahigh draw ratio after the gel spinning process. The drawability of the as-prepared gel specimens was found to depend significantly on the compositions of solutions from which gels were made [6, 7, 33]. Several authors [12–15, 33] reported that the drawing temperature and rate

could markedly affect the maximal achievable draw ratio and tensile properties of solution-grown UHMWPE samples. In addition to the gel solution compositions and drawing conditions, it is generally recognized that the conditions used in the formation process after spinning and/or solution casting of gel solutions can also have a significant influence on the morphology, microstructure, and drawing properties of the specimens formed during the above-mentioned processes [7, 9, 14, 17–23].

Our recent investigations [24–27] found that the achievable draw ratios (achievable λ) of UHMWPE/nanofillers as-prepared fibers prepared near the optimal UHMWPE concentration improve to a maximal value as their nanofillers contents reach an optimal value, respectively, in which, the nanofillers (e.g., carbon nanotube (CNT) [24], attapulgite [25], nanosilica and/or their functionalized nanofillers [26], and functionalized bacterial cellulose [27]) with extremely high specific surface areas can serve as efficient nucleation sites and facilitate the crystallization of UHMWPE molecules into crystals but with lower melting temperatures (T_m) and/or evaluated smaller crystal thickness (l_c) values during their crystallization processes. Presumably, the crystals with lower T_m and/or evaluated smaller l_c values obtained at proper plain and/or modified nanofiller contents can be melted and pulled out of folded lamellar crystals relatively easily during ultradrawing processes and hence this results in higher drawability and orientation of the UHMWPE/nanofillers or UHMWPE/modified nanofillers fibers. The maximal achievable draw ratios of UHMWPE/nanofillers or UHMWPE/modified nanofillers as-prepared fiber specimens and the tensile strengths of the drawn UHMWPE/nanofillers or UHMWPE/modified nanofillers fiber specimens are significantly higher than those of the plain UHMWPE as-prepared and drawn fiber specimens prepared at the same draw ratios of UHMWPE concentrations but without addition of the nanofillers and/or modified nanofillers, respectively. The ultimate tensile strength values of UHMWPE/purified attapulgite, UHMWPE/functionalized CNT, UHMWPE/functionalized nanosilica, and UHMWPE/functionalized bacterial cellulose drawn fibers prepared using one-stage drawing process at 95°C can reach 4.7, 5.8, 7.0, and 7.1 GN m⁻², respectively, which is about 1.74, 2.15, 2.59, and 2.63 times of that of the corresponding plain UHMWPE drawn fibers prepared at the same optimal UHMWPE concentration, formation, and drawing condition but without incorporation of modified nanofillers.

The above results clearly suggested that nanofillers with high specific surface areas can serve as efficient nucleation sites for crystallization of UHMWPE molecules and improve the ultradrawing and ultimate tensile properties of UHMWPE/nanofiller fibers. Among these nanofillers, nanosilica particles are cheap and commercially available for a wide range of specific surface areas. In this study, the ultradrawing and ultimate tensile properties of the UHMWPE/nanosilica and UHMWPE/functionalized nanosilica fibers with a wide range of specific surface areas were systematically investigated. The maximal achievable λ and ultimate tensile strength values obtained for the best

prepared UHMWPE/functionalized nanosilica as-prepared fibers are even higher than those of the best prepared UHMWPE/modified attapulgite, UHMWPE/functionalized CNT, and UHMWPE/functionalized bacterial cellulose as-prepared fibers prepared at the optimal modified attapulgite, functionalized CNT, and functionalized bacterial cellulose contents, respectively [24–27]. Specific surface area, morphological and Fourier transform infrared analyses of the original and functionalized nanosilica specimens, and/or investigations of thermal, orientation factor, and ultimate tensile properties of the as-prepared and drawn UHMWPE/functionalized nanosilica fiber specimens were performed to understand the above improved ultradrawing and ultimate tensile properties of the UHMWPE/functionalized nanosilica as-prepared and/or drawn fibers.

2. Experimental

2.1. Materials and Sample Preparation. The UHMWPE GUR-4120 resin used in this study is associated with a weight average molecular weight (Mw) of 5.0×10^6 , which was kindly supplied by Celanese (Nanjing) Diversified Chemical Corporation, Nanjing, China. Three types of nanosilica particles (Merck SSA-100, SSA-300, and SSA-600) used in this study were purchased from Lu Ming Nanomaterials Corporation, Dalian, China. The specific surface areas of SSA-100, SSA-300, and SSA-600 nanosilica (NSI) particles were quoted as 90–105 m²/g, 285–305 m²/g, and 580–610 m²/g, respectively, by Lu Ming Nanomaterials Corporation. Functionalized nanosilica (FNSI) particles were prepared by grafting maleic anhydride grafted polyethylene (PE_{g-MAH}) molecules onto NSI particles in ultrasonicated mixtures of decalin, NSI, and PE_{g-MAH} at 170°C for 1 hour, in which, PE_{g-MAH} resin was purchased from Langfang Plastic Corporation, Langfang, China. The nanosilica and functionalized nanosilica particles prepared above are referred to as NSI^x and FNSI^x_{my}, respectively, in the following discussion, in which, the superscript x denotes the quoted specific surface areas of virgin NSI nanosilica particles and the subscript y denotes the weight ratio of PE_{g-MAH} to NSI^x used in the preparation processes of FNSI^x_{my} functionalized nanosilica particles. Table 1 summarized designations and compositions of typical nanosilica and functionalized nanosilica particles prepared in this study.

Varying contents of NSI^x and FNSI^x_{my} particles together with UHMWPE resin were dispersed and dissolved in decalin at 135°C for 1.5 hours, in which 0.1% di-*t*-butyl-*p*-cresol was added as an antioxidant. The UHMWPE, UHMWPE/NSI^x, and UHMWPE/FNSI^x_{my} gel solutions prepared above were then fed into a temperature-controlled hopper and kept as hot homogenized gel solutions before spinning. The hot homogenized gel solutions were then gel-spun using a conical die with an exit diameter of 1 mm at an extrusion rate of 1000 mm/min and an extrusion temperature of 170°C. A water bath and a winder with 70 mm in diameter were placed at a distance of 520 mm and 810 mm from the spinneret exit, respectively. The extruded gel fibers were cooled in a temperature-conditioned atmosphere and then quenched into a water bath for about 1 minute, where the temperature

TABLE 1: Designations, compositions, and specific surface areas of nanosilica particles (NSI^x) and functionalized nanosilica particles (FNSI^x_{my}) prepared in this study.

NSI ^x and FNSI ^x _{my} specimens	Mass ratios of PE _{g-MAH} to NSI ^x	Specific surface areas (m ² /g)
NSI ¹⁰⁰	0.0	102.3
FNSI ¹⁰⁰ _{m1}	1.0	109.7
FNSI ¹⁰⁰ _{m2}	2.0	114.8
FNSI ¹⁰⁰ _{m3}	3.0	129.8
FNSI ¹⁰⁰ _{m6}	6.0	122.4
FNSI ¹⁰⁰ _{m12}	12.0	109.6
NSI ³⁰⁰	0.0	303.9
FNSI ³⁰⁰ _{m2}	2.0	314.5
FNSI ³⁰⁰ _{m3}	3.0	325.5
FNSI ³⁰⁰ _{m6}	6.0	335.8
FNSI ³⁰⁰ _{m9}	9.0	330.8
FNSI ³⁰⁰ _{m12}	12.0	315.3
NSI ⁶⁰⁰	0.0	601.7
FNSI ⁶⁰⁰ _{m2}	2.0	617.4
FNSI ⁶⁰⁰ _{m3}	3.0	621.4
FNSI ⁶⁰⁰ _{m6}	6.0	625.3
FNSI ⁶⁰⁰ _{m9}	9.0	630.7
FNSI ⁶⁰⁰ _{m12}	12.0	621.4

of the air atmosphere and water bath was controlled at 5°C. The quenched fibers were then extracted in n-hexane bath for 5 minutes to remove the residual decalin solvent. The extracted fiber specimens were then dried in air for 30 minutes to remove the remaining n-hexane solvent before any drawing run. The UHMWPE, UHMWPE/NSI^x, and UHMWPE/FNSI^x_{my} as-prepared fiber specimens prepared above are referred to as F₁₀₀, F₁₀₀NSI^x_z, and F₁₀₀FNSI^x_{my-z} as-prepared fiber specimens, respectively, in the following discussion, in which, the superscript *x* denotes the quoted specific surface areas of varying NSI^x particles used to prepare NSI^x and FNSI^x_{my} particles in F₁₀₀NSI^x_z and F₁₀₀FNSI^x_{my-z} as-prepared fiber specimens, respectively; the subscript 100 denotes one hundred parts of UHMWPE resins used in the as-prepared fibers; *y* denotes the weight ratio of PE_{g-MAH} to NSI^x used in the preparation processes of FNSI^x_{my} fillers, while the subscript *z* denotes parts of NSI^x or FNSI^x_{my} fillers used in per hundred parts of UHMWPE resins in the as-prepared fibers. Table 2 summarized designations of typical UHMWPE, UHMWPE/nanosilica, and UHMWPE/functionalized nanosilica as-prepared fiber specimens and the corresponding compositions of gel solutions used in the gel spinning processes.

2.2. *Fourier Transform Infrared Spectroscopy.* Fourier transform infrared (FTIR) spectroscopic measurements of NSI^x or FNSI^x_{my} specimens with varying specific surface areas were recorded on a Nicolet Avatar 360 FTIR spectrophotometer at 25°C, wherein 32 scans with a spectral resolution 1 cm⁻¹ were

collected during each spectroscopic measurement. Infrared spectra of NSI^x or FNSI^x_{my} film specimens were determined using the conventional KBr disk method. Alcohol and decalin solutions containing NSI^x or FNSI^x_{my} particles, respectively, were cast onto KBr disk and dried at 60°C for 30 minutes. The cast films used in this study were prepared sufficiently thin enough to obey the Beer-Lambert law.

2.3. *Morphological Analyses.* In order to understand the morphology on the surfaces of NSI^x or FNSI^x_{my} particles with varying specific surface areas prepared in Materials and Sample Preparation, NSI^x particles were dispersed in alcohol, while FNSI^x_{my} particles were dispersed in decalin to have a better dispersed morphology before examination. Before morphological analyses, ten micrograms of NSI^x or FNSI^x_{my} particles was added and ultrasonicated in 10 mL alcohol and decalin at 25°C for 5 minutes, respectively. The dispersed particles were then dried onto a carbon-coated copper grid under ambient conditions prior to morphological analyses. The cast NSI^x or FNSI^x_{my} particles were then examined using a Philip transmission electron microscope (TEM) model Tecnai G20 operated at 200 kV.

2.4. *Specific Surface Area Analyses.* A Laser Particle Size Analyzer model BT-9300H (Dandong Bettersize Instruments Corporation, Dandong, China) was used to study the specific surface areas of NSI^x or FNSI^x_{my} particles with varying specific surface areas. Before analyses, ten micrograms of NSI^x or FNSI^x_{my} particles was added and ultrasonicated in 10 mL alcohol and decalin at 25°C for 5 minutes, respectively. The specific surface areas of NSI^x or FNSI^x_{my} particles were then measured by placing the ultrasonicated solutions prepared above in the curette of the Laser Particle Size Analyzer at 25°C.

2.5. *Thermal and Orientation Factor Analyses.* Thermal properties of all as-prepared fiber specimens were performed on a Du Pont differential scanning calorimeter (DSC) model 2000. All scans were carried out at a heating rate of 20°C/min under flowing nitrogen at a flow rate of 25 mL/min. Samples weighing 0.5 mg and 15 mg were placed in the standard aluminum sample pans for determination of their melting temperature (*T_m*) and percentage crystallinity (*X_c*) values, respectively. The percentage crystallinity values of the as-prepared fiber specimens were estimated using baselines drawn from 40 to 200°C and a perfect heat of fusion of polyethylene of 293 J/g [28].

In order to understand the ultradrawing properties of UHMWPE, UHMWPE/NSI^x, and UHMWPE/FNSI^x_{my} as-prepared fiber specimens, the lamellar thickness (*l_c*) values of the above as-prepared fibers were evaluated from their *T_m* values using Hoffman and Weeks' equation [28, 29] given in (1) as follows, in which, an equilibrium melting temperature (*T_m⁰*) of 145.5°C, a perfect heat of fusion (ΔH_f^0) of 293 J/g, and a folded surface free energy (σ_e) of 9×10^{-6} J/cm² of polyethylene crystals [28] were used for evaluation of *l_c* values

TABLE 2: Designations, melting temperatures (T_m), percentage crystallinity (X_c), and evaluated lamellar thickness (l_c) values of UHMWPE, typical UHMWPE/nanosilica, and UHMWPE/functionalized nanosilica as-prepared fiber specimens and corresponding compositions of gel solutions used in the gel spinning processes.

As-prepared fiber specimens	Original nanosilica (g/phr)	Functionalized nanosilica (g/phr)	UHMWPE (g/phr)	Volumes of decalin in gel solutions (mL)	T_m ($^{\circ}$ C)	X_c (%)	l_c (nm)
F ₁₀₀	0	—	2/100	100	142.7	65.1	30.7
F ₁₀₀ NSI ¹⁰⁰ _{0.05}	0.001/0.05	—	2/100	100	141.1	67.8	25.6
F ₁₀₀ NSI ¹⁰⁰ _{0.1}	0.002/0.1	—	2/100	100	140.2	70.1	17.5
F ₁₀₀ NSI ¹⁰⁰ _{0.125}	0.0025/0.125	—	2/100	100	141.9	66.0	18.2
F ₁₀₀ NSI ³⁰⁰ _{0.0375}	0.00075/0.0375	—	2/100	100	140.9	68.3	22.5
F ₁₀₀ NSI ³⁰⁰ _{0.0625}	0.00125/0.0625	—	2/100	100	140.2	70.8	17.5
F ₁₀₀ NSI ³⁰⁰ _{0.1}	0.002/0.1	—	2/100	100	141.1	67.8	22.5
F ₁₀₀ NSI ⁶⁰⁰ _{0.0375}	0.00075/0.0375	—	2/100	100	140.7	69.1	19.3
F ₁₀₀ NSI ⁶⁰⁰ _{0.05}	0.001/0.05	—	2/100	100	139.9	71.5	15.7
F ₁₀₀ NSI ⁶⁰⁰ _{0.1}	0.002/0.1	—	2/100	100	140.8	67.8	22.1
F ₁₀₀ FNSI ¹⁰⁰ _{m2-0.0375}	—	0.00075/0.0375	2/100	100	141.6	66.2	25.8
F ₁₀₀ FNSI ¹⁰⁰ _{m2-0.075}	—	0.0015/0.075	2/100	100	139.3	70.3	15.1
F ₁₀₀ FNSI ¹⁰⁰ _{m2-0.1}	—	0.002/0.1	2/100	100	139.5	69.0	15.4
F ₁₀₀ FNSI ¹⁰⁰ _{m3-0.0375}	—	0.00075/0.0375	2/100	100	140.7	69.1	17.5
F ₁₀₀ FNSI ¹⁰⁰ _{m3-0.075}	—	0.0015/0.075	2/100	100	138.3	75.4	12.4
F ₁₀₀ FNSI ¹⁰⁰ _{m3-0.1}	—	0.002/0.1	2/100	100	138.9	75.1	13.5
F ₁₀₀ FNSI ¹⁰⁰ _{m6-0.0375}	—	0.00075/0.0375	2/100	100	140.9	68.9	22.5
F ₁₀₀ FNSI ¹⁰⁰ _{m6-0.075}	—	0.0015/0.075	2/100	100	139.2	72.4	14.1
F ₁₀₀ FNSI ¹⁰⁰ _{m6-0.1}	—	0.002/0.1	2/100	100	139.6	71.3	14.7
F ₁₀₀ FNSI ³⁰⁰ _{m3-0.025}	—	0.0005/0.025	2/100	100	139.5	73.2	14.6
F ₁₀₀ FNSI ³⁰⁰ _{m3-0.05}	—	0.001/0.05	2/100	100	138.6	74.0	13.1
F ₁₀₀ FNSI ³⁰⁰ _{m3-0.075}	—	0.0015/0.075	2/100	100	139.3	73.4	14.2
F ₁₀₀ FNSI ³⁰⁰ _{m6-0.025}	—	0.0005/0.025	2/100	100	138.5	75.2	12.7
F ₁₀₀ FNSI ³⁰⁰ _{m6-0.05}	—	0.001/0.05	2/100	100	137.6	76.0	11.3
F ₁₀₀ FNSI ³⁰⁰ _{m6-0.075}	—	0.0015/0.075	2/100	100	138.3	75.4	12.4
F ₁₀₀ FNSI ³⁰⁰ _{m9-0.025}	—	0.0005/0.025	2/100	100	139.0	74.1	13.6
F ₁₀₀ FNSI ³⁰⁰ _{m9-0.05}	—	0.001/0.05	2/100	100	138.1	75.0	12.0
F ₁₀₀ FNSI ³⁰⁰ _{m9-0.075}	—	0.0015/0.075	2/100	100	138.8	73.9	13.5
F ₁₀₀ FNSI ⁶⁰⁰ _{m3-0.025}	—	0.0005/0.025	2/100	100	137.8	74.2	11.6
F ₁₀₀ FNSI ⁶⁰⁰ _{m3-0.0375}	—	0.00075/0.0375	2/100	100	137.2	74.8	10.7
F ₁₀₀ FNSI ⁶⁰⁰ _{m3-0.075}	—	0.0015/0.075	2/100	100	138.3	73.7	12.4
F ₁₀₀ FNSI ⁶⁰⁰ _{m9-0.025}	—	0.0005/0.025	2/100	100	136.5	76.2	10.7
F ₁₀₀ FNSI ⁶⁰⁰ _{m9-0.0375}	—	0.00075/0.0375	2/100	100	136.1	76.8	9.5
F ₁₀₀ FNSI ⁶⁰⁰ _{m9-0.075}	—	0.0015/0.075	2/100	100	137.0	75.9	10.1
F ₁₀₀ FNSI ⁶⁰⁰ _{m12-0.025}	—	0.0005/0.025	2/100	100	137.3	74.7	11.1
F ₁₀₀ FNSI ⁶⁰⁰ _{m12-0.0375}	—	0.00075/0.0375	2/100	100	136.7	75.3	9.8
F ₁₀₀ FNSI ⁶⁰⁰ _{m12-0.075}	—	0.0015/0.075	2/100	100	137.8	74.3	11.6

of UHMWPE, UHMWPE/NSI, and UHMWPE/FNSI as-prepared fiber specimens:

$$T_m = T_m^o \left[1 - \frac{2\sigma_e}{l_c \Delta H_f^0} \right]. \quad (1)$$

The orientation factor (f_0) values of UHMWPE, UHMWPE/NSI^x, and UHMWPE/FNSI^x_{my} as-prepared and drawn fiber specimens were measured using a sonic velocity orientation instrument model SCY-III, which was purchased from Donghuakaili Chemicals and Fiber Technology Corporation, Shanghai, China. Before testing, the fiber

specimen with 60 cm in length was wound and clamped on a testing device with a span of 40 cm. f_0 values of the as-spun and drawn fiber specimens were then measured at 25°C. A minimum of five samples of each specimen were tested and averaged during f_0 measurements. f_0 values were evaluated using (2) as suggested by Xiao and coauthors [30]:

$$f_s = 1 - \left(\frac{C_u}{C} \right)^2, \quad (2)$$

where C is the sonic velocity of the as-prepared or drawn UHMWPE fiber specimen and C_u is the sonic velocity of the fully unoriented sample, taken as 1.65 km/s [30].

2.6. Drawing and Tensile Properties of Fiber Specimens. The UHMWPE, UHMWPE/NSI^x, and UHMWPE/FNSI^x_{my} fiber specimens used in the drawing experiments were cut from the dried as-prepared fibers and then stretched on a Gotech tension testing machine model GT-TFS-2000 equipped with a temperature-controlled oven. The fibers are 150 mm in length, which were wound and clamped in a stretching device and then stretched at a crosshead speed of 20 mm/min and a constant temperature of 95°C. The draw ratio of each fiber specimen was determined as the ratio of the marked displacement after and before drawing. The marked displacement before drawing was 27 mm. The tensile properties of the as-prepared and drawn fibers were determined using a Hung Ta tension testing machine model HT-9112 at a crosshead speed of 20 mm/min. A minimum of five samples of each specimen were tested and averaged during the tensile experiments.

3. Results and Discussion

3.1. Fourier Transform Infrared Spectroscopy. Figure 1 illustrates typical Fourier transform infrared (FTIR) spectra of nanosilica (NSI^x), functionalized nanosilica (FNSI^x_{my}), and maleic anhydride grafted polyethylene (PE_{g-MAH}) specimens. PE_{g-MAH} specimen exhibited two distinctive absorption bands centered at 1711 and 1791 cm⁻¹, which were generally attributed to the motion of O=C=O and C=O stretching vibrations of maleic anhydride [31] (see Figure 1(a)). As shown in Figures 1(b), 1(f), and 1(j), there are three distinguished absorption bands centered at 1097, 1635, and 3442 cm⁻¹ corresponding to the motions of Si-O-Si stretching, H-O-H bending, and Si-OH stretching vibrations [31], respectively, which were found in the spectra of NSI¹⁰⁰, NSI³⁰⁰, and NSI⁶⁰⁰ specimens. It is interesting to note that the peak magnitudes of Si-O-Si stretching, H-O-H bending, and Si-OH stretching bands of NSI^x specimens increased significantly as their quoted specific surface areas increased from 100 to 300 and 600 m²/g (see Figures 1(b), 1(f), and 1(j)). The significant increase in the magnitude of Si-O-Si stretching, H-O-H bending, and Si-OH stretching bands of NSI^x specimens is attributed to the increased amounts of Si-O-Si, H-O-H, and Si-OH groups exposed on NSI^x particles with higher specific surface areas.

After grafting PE_{g-MAH} to NSI¹⁰⁰, NSI³⁰⁰, and NSI⁶⁰⁰ particles, the peak magnitudes corresponding to H-O-H

bending and Si-OH stretching bands of FNSI^x_{my} specimens reduced significantly as the weight ratios of PE_{g-MAH} to NSI^x increased (see Figures 1(b) to 1(e), 1(f) to 1(i), and 1(j) to 1(m)). In fact, as shown in Figures 1(d) to 1(e), 1(h) to 1(i), and 1(l) to 1(m), H-O-H bending and Si-OH stretching bands originally present in NSI^x specimens disappeared almost completely as the weight ratios of PE_{g-MAH} to NSI¹⁰⁰, NSI³⁰⁰, and NSI⁶⁰⁰ of FNSI¹⁰⁰_{my}, FNSI³⁰⁰_{my}, and FNSI⁶⁰⁰_{my} specimens were equal to or more than 3, 6, and 9, respectively. In the meantime, a new absorption band centered at around 1228 cm⁻¹ corresponding to the motion of ester C-O stretching vibration [31] was found in the spectra of FNSI¹⁰⁰_{my}, FNSI³⁰⁰_{my}, and FNSI⁶⁰⁰_{my} specimens (see Figures 1(c) to 1(e), 1(g) to 1(i), and 1(k) to 1(m)). In contrast, the absorption bands centered at 1711 and 1791 cm⁻¹ corresponding to the motion of C=O and O-C=O stretching vibrations of maleic anhydride gradually reappeared as the weight ratios of PE_{g-MAH} to NSI¹⁰⁰, NSI³⁰⁰, and NSI⁶⁰⁰ of FNSI¹⁰⁰_{my}, FNSI³⁰⁰_{my}, and FNSI⁶⁰⁰_{my} specimens, respectively, were equal to 6, 9, and 12. Presumably, the gradually disappearing H-O-H bending and Si-OH stretching bands and newly developed ester C-O stretching bands of FNSI¹⁰⁰_{my}, FNSI³⁰⁰_{my}, and FNSI⁶⁰⁰_{my} specimens are attributed to the reaction of the hydroxyl groups of NSI¹⁰⁰, NSI³⁰⁰, and NSI⁶⁰⁰ particles with the maleic anhydride groups of PE_{g-MAH} molecules during their functionalized processes. The reappearance of O-C=O and C=O stretching bands of maleic anhydride groups is most likely due to the overdose of PE_{g-MAH} during the functionalized processes of FNSI¹⁰⁰_{my}, FNSI³⁰⁰_{my}, and FNSI⁶⁰⁰_{my} particles.

3.2. Morphological Analyses of NSI^x and FNSI^x_{my} Particles.

Figure 2 exhibits typical TEM micrographs of NSI^x and FNSI^x_{my} particles. Typical irregular particle feature with dimensions of 250–350, 150–200, and 50–80 nm in diameter was observed for NSI¹⁰⁰, NSI³⁰⁰, and NSI⁶⁰⁰ particles (see Figures 2(a), 2(d), and 2(g)). After modification by PE_{g-MAH}, some translucent resins were found attaching on the surfaces of NSI¹⁰⁰, NSI³⁰⁰, and NSI⁶⁰⁰ particles, wherein the amounts of attached translucent resins increased gradually as the weight ratios of PE_{g-MAH} to NSI¹⁰⁰, NSI³⁰⁰, and NSI⁶⁰⁰ increased, respectively (see Figures 2(b) to 2(c), 2(e) to 2(g), and 2(h) to 2(i)). As evidenced by FTIR analyses in the previous section, the attached translucent resins were most likely the grafted PE_{g-MAH} molecules, which were firmly bonded to NSI¹⁰⁰, NSI³⁰⁰, and NSI⁶⁰⁰ particles by the reaction of the maleic anhydride groups of PE_{g-MAH} resins with the hydroxyl groups of NSI¹⁰⁰, NSI³⁰⁰, and NSI⁶⁰⁰ particles, respectively. In fact, the translucent resins were found fully surrounding and overwrapping on NSI¹⁰⁰, NSI³⁰⁰, and NSI⁶⁰⁰ particles, as the weight ratios of PE_{g-MAH} to NSI¹⁰⁰, NSI³⁰⁰, and NSI⁶⁰⁰ were greater than 3, 6, and 12, respectively (see Figures 2(c), 2(f), and 2(i)).

3.3. Specific Surface Area Analyses of NSI^x and FNSI^x_{my} Particles. The values of specific surface areas of NSI^x and FNSI^x_{my} particles are summarized in Figure 3 and Table 1. The specific

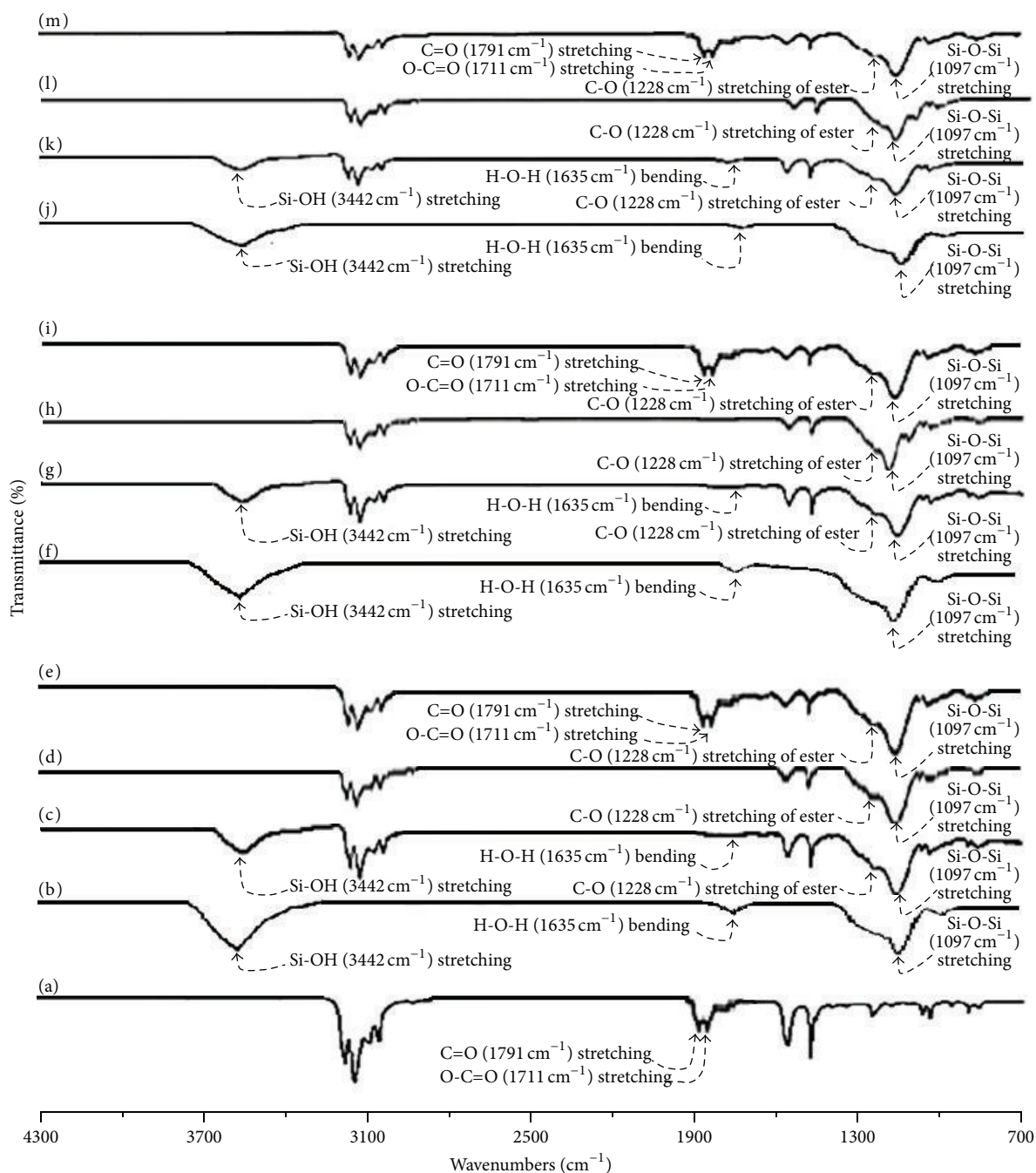


FIGURE 1: FTIR spectra of (a) PE_{g-MAH}, (b) NSI⁶⁰⁰, (c) FNSI⁶⁰⁰_{m3}, (d) FNSI⁶⁰⁰_{m9}, (e) FNSI⁶⁰⁰_{m12}, (f) NSI³⁰⁰, (g) FNSI³⁰⁰_{m3}, (h) FNSI³⁰⁰_{m6}, (i) FNSI³⁰⁰_{m9}, (j) NSI¹⁰⁰, (k) FNSI¹⁰⁰_{m2}, (l) FNSI¹⁰⁰_{m3}, and (m) FNSI¹⁰⁰_{m6} specimens (the superscript x denotes the quoted specific surface areas of virgin NSI ^{x} nanosilica particles; y denotes the weight ratio of PE_{g-MAH} to NSI ^{x} used in the preparation processes of FNSI ^{x} _{y} functionalized nanosilica particles).

surface areas of NSI¹⁰⁰, NSI³⁰⁰, and NSI⁶⁰⁰ particles were evaluated at around 100, 300, and 600 m²/g (i.e., 102.3, 303.9, and 601.7 m²/g), respectively. After modification by PE_{g-MAH}, the specific surface areas of FNSI¹⁰⁰ _{y} , FNSI³⁰⁰ _{y} , and FNSI⁶⁰⁰ _{y} particles reached a maximal value at 129.8, 335.8, and 630.7 m²/g, respectively, as the weight ratios of PE_{g-MAH}

to NSI¹⁰⁰, NSI³⁰⁰, and NSI⁶⁰⁰ approached an optimal value at 3, 6, and 9, respectively. Presumably, the beneficial effect of PE_{g-MAH} contents on specific surface areas of FNSI ^{x} _{y} particles is attributed to the increase in grafted amounts and specific surface areas of PE_{g-MAH} on NSI ^{x} particles during their functionalized processes. However, PE_{g-MAH} molecules may agglomerate, bundle, entangle together, and overwrap NSI ^{x}

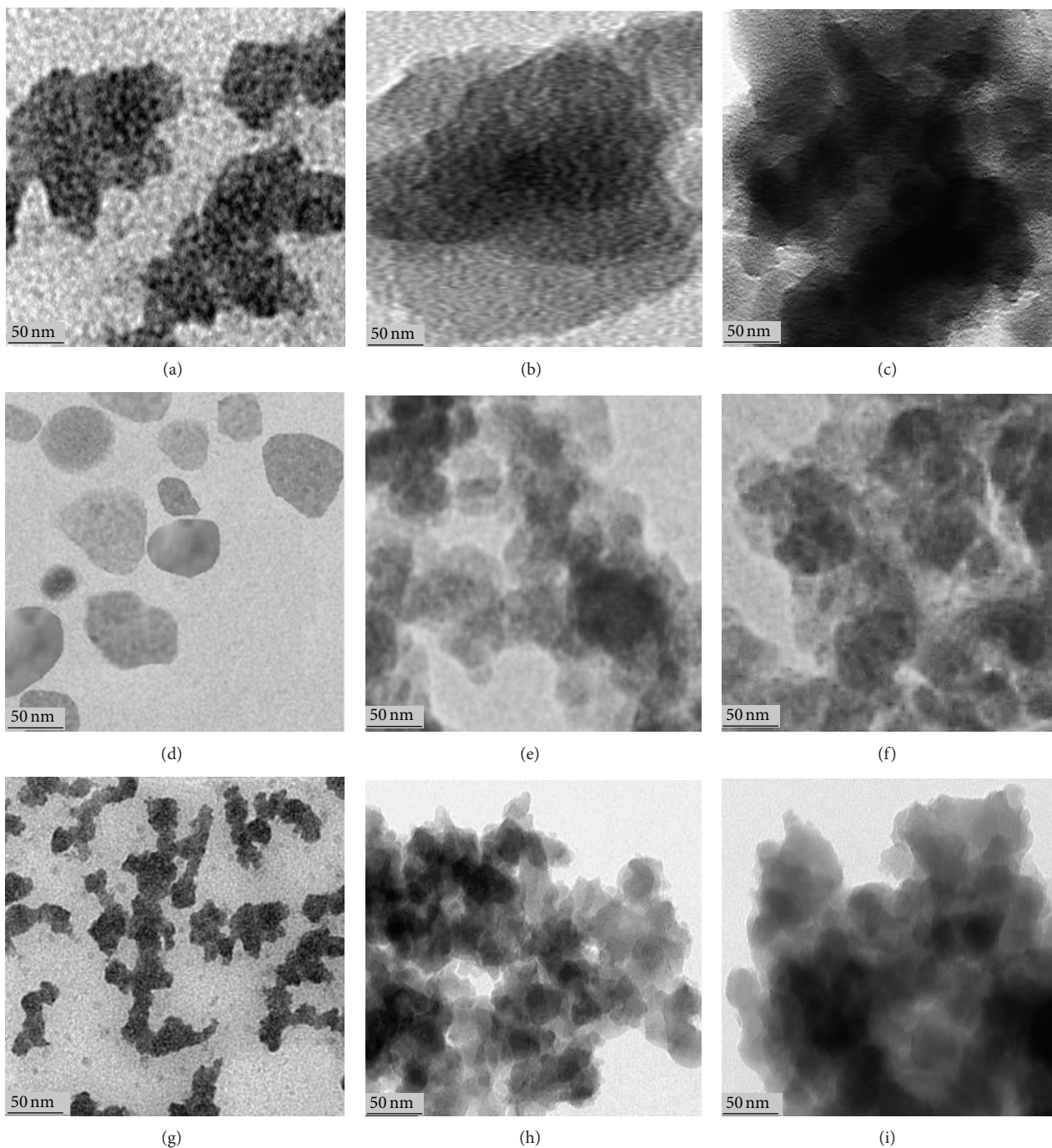


FIGURE 2: TEM micrographs of (a) NSI¹⁰⁰, (b) FNSI¹⁰⁰_{m3}, (c) FNSI¹⁰⁰_{m6}, (d) NSI³⁰⁰, (e) FNSI³⁰⁰_{m6}, (f) FNSI³⁰⁰_{m9}, (g) NSI⁶⁰⁰, (h) FNSI⁶⁰⁰_{m9}, and (i) FNSI⁶⁰⁰_{m12} specimens.

particles, as PE_g-MAH molecules are superfluous and can no longer graft onto NSI^x particles. As evidenced by morphology analyses in the previous section, some translucent resins were found fully surrounding and overwrapping on NSI^x particles (see Figures 2(c), 2(g), and 2(i)), as the weight ratios of PE_g-MAH to NSI¹⁰⁰, NSI³⁰⁰, and NSI⁶⁰⁰ were more than 3, 6, and 9, respectively. Based on this premise, it is reasonable to infer that the overwrapped FNSI^x_{my} particles

exhibit relatively lower specific surface areas than those FNSI¹⁰⁰_{m3}, FNSI³⁰⁰_{m6}, and FNSI⁶⁰⁰_{m9} particles grafted with proper amounts of PE_g-MAH resins.

3.4. Thermal Properties of the As-Prepared Fibers. Typical DSC thermograms, melting temperature (T_m), percentage crystallinity (X_c), and evaluated lamellar thickness (l_c) values of UHMWPE (F₁₀₀), UHMWPE/NSI (F₁₀₀NSI^x_z),

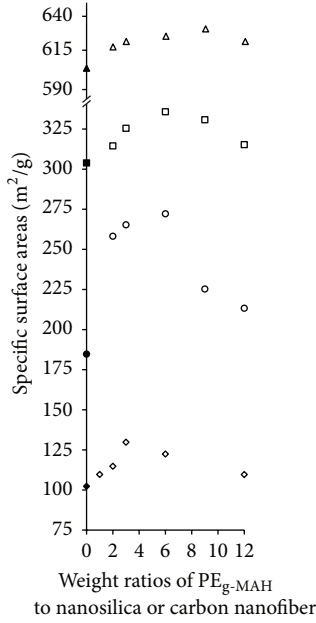


FIGURE 3: Specific surface areas of carbon nanofiber (•), NSI¹⁰⁰ (◆), NSI³⁰⁰ (■), NSI⁶⁰⁰ (▲), FNSI¹⁰⁰_{my} (◇), FNSI³⁰⁰_{my} (□), FNSI⁶⁰⁰_{my} (△), and modified carbon nanofiber (◊) specimens.

and UHMWPE/FNSI ($F_{100}\text{FNSI}^x_{my-z}$) as-prepared fiber series specimens are summarized in Figure 4 and Table 2. A main melting endotherm with T_m and X_c at 142.7°C and 65.1%, respectively, was found for F_{100} specimen. After incorporation of NSI^x and/or FNSI^x_{my} particles in UHMWPE, T_m (or evaluated l_c) values of $F_{100}\text{NSI}^x_z$ (i.e., $F_{100}\text{NSI}^{100}_z$, $F_{100}\text{NSI}^{300}_z$, and $F_{100}\text{NSI}^{600}_z$) and/or $F_{100}\text{FNSI}^x_{my-z}$ (i.e., $F_{100}\text{FNSI}^{100}_{my-z}$, $F_{100}\text{FNSI}^{300}_{my-z}$, and $F_{100}\text{FNSI}^{600}_{my-z}$) as-prepared fibers reduced to a minimal value, as their NSI^x and/or FNSI^x_{my} contents reached an optimal value, respectively, in which T_m and l_c values of $F_{100}\text{FNSI}^{100}_{my-0.075}$, $F_{100}\text{FNSI}^{300}_{my-0.05}$, and $F_{100}\text{FNSI}^{600}_{my-0.0375}$ as-prepared fibers prepared at the optimal FNSI^x_{my} contents at 0.075, 0.05, and 0.0375 phr, respectively, were significantly lower than those of the corresponding $F_{100}\text{NSI}^{100}_{0.1}$, $F_{100}\text{NSI}^{300}_{0.0625}$, and $F_{100}\text{NSI}^{600}_{0.05}$ as-prepared fibers with an optimal NSI^x content at 0.1, 0.0625, and 0.05 phr, respectively. However, X_c values of $F_{100}\text{NSI}^x_z$ and/or $F_{100}\text{FNSI}^x_{my-z}$ as-prepared fibers increased to a maximal value, as NSI^x and/or FNSI^x_{my} contents reached their corresponding optimal values, respectively, wherein X_c values of $F_{100}\text{FNSI}^{100}_{my-0.075}$, $F_{100}\text{FNSI}^{300}_{my-0.05}$, and $F_{100}\text{FNSI}^{600}_{my-0.0375}$ as-prepared fibers prepared at their optimal FNSI^x_{my} contents, respectively, were significantly higher than those of the corresponding $F_{100}\text{NSI}^{100}_{0.1}$, $F_{100}\text{NSI}^{300}_{0.0625}$, and $F_{100}\text{NSI}^{600}_{0.05}$ as-prepared fibers prepared at their optimal NSI^x contents, respectively. Moreover, it is worth noting that $F_{100}\text{FNSI}^{100}_{my-0.075}$, $F_{100}\text{FNSI}^{300}_{my-0.05}$, and

$F_{100}\text{FNSI}^{600}_{my-0.0375}$ as-prepared fibers prepared at the optimal FNSI^x_{my} contents exhibited another minimal T_m (or evaluated l_c) but other maximal X_c values as their FNSI¹⁰⁰_{my}, FNSI³⁰⁰_{my}, and FNSI⁶⁰⁰_{my} were modified using an optimal weight ratio of PE_{g-MAH} to NSI¹⁰⁰, NSI³⁰⁰, and NSI⁶⁰⁰ at 3, 6, and 9, respectively (see Figures 5(j), 6(i), and 7(h)). Finally, it is interesting to note that the lowest T_m (or evaluated l_c) values obtained for $F_{100}\text{FNSI}^{100}_{m3-0.075}$, $F_{100}\text{FNSI}^{300}_{m6-0.05}$, and $F_{100}\text{FNSI}^{600}_{m9-0.0375}$ as-prepared fibers prepared at the optimal FNSI^x_{my} contents and weight ratio of PE_{g-MAH} to NSI^x reduced significantly as the specific surface areas of FNSI^x_{my} particles increased, while the highest X_c values obtained for $F_{100}\text{FNSI}^{100}_{m3-0.075}$, $F_{100}\text{FNSI}^{300}_{m6-0.05}$, and $F_{100}\text{FNSI}^{600}_{m9-0.0375}$ as-prepared fibers increased consistently as the specific surface areas of their FNSI^x_{my} particles increased. For instance, T_m values of $F_{100}\text{FNSI}^{100}_{m3-0.075}$, $F_{100}\text{FNSI}^{300}_{m6-0.05}$, and $F_{100}\text{FNSI}^{600}_{m9-0.0375}$ as-prepared fibers reduced from 138.3°C to 137.6°C and to 136.1°C, as the specific surface areas of FNSI¹⁰⁰_{m3}, FNSI³⁰⁰_{m6}, and FNSI⁶⁰⁰_{m9} present in $F_{100}\text{FNSI}^{100}_{m3-0.075}$, $F_{100}\text{FNSI}^{300}_{m6-0.05}$, and $F_{100}\text{FNSI}^{600}_{m9-0.0375}$ as-prepared fibers increased from 129.8 to 335.8 and 630.7 m²/g, respectively, while their X_c values increased from 75.4% to 76.0% and 76.8%, as the specific surface areas of FNSI¹⁰⁰_{m3}, FNSI³⁰⁰_{m6}, and FNSI⁶⁰⁰_{m9} present in $F_{100}\text{FNSI}^{100}_{m3-0.075}$, $F_{100}\text{FNSI}^{300}_{m6-0.05}$, and $F_{100}\text{FNSI}^{600}_{m9-0.0375}$ as-prepared fibers increased from 129.8 to 335.8 and 630.7 m²/g, respectively.

As evidenced by specific surface area and TEM analyses in the previous sections, NSI^x and/or FNSI^x_{my} particles are with a wide range of relatively large surface areas per volume, which make them in close proximity to a large fraction of the UHMWPE matrix. Apparently, even very small contents of dispersed NSI^x and/or FNSI^x_{my} particles can serve as efficient nucleation sites for UHMWPE molecules during their gel spinning processes. These efficient nucleation sites of NSI^x and/or FNSI^x_{my} particles then facilitate the crystallization of UHMWPE molecules into crystals with thinner lamellar thickness and/or lower T_m values during their crystallization processes. After grafting PE_{g-MAH} to NSI¹⁰⁰, NSI³⁰⁰, and NSI⁶⁰⁰ particles, the properly modified FNSI^x_{my} particles with even higher specific surface areas are likely to disperse better in UHMWPE and serve as more effective sites for nucleation of UHMWPE molecules during their gel spinning processes than NSI^x particles. As a consequence, $F_{100}\text{FNSI}^{100}_{my-z}$, $F_{100}\text{FNSI}^{300}_{my-z}$, and $F_{100}\text{FNSI}^{600}_{my-z}$ as-prepared fiber specimens exhibit significantly higher X_c but lower T_m (or evaluated l_c) values than the corresponding $F_{100}\text{NSI}^{100}_z$, $F_{100}\text{NSI}^{300}_z$, and $F_{100}\text{NSI}^{600}_z$ as-prepared fiber specimens prepared with the same NSI^x contents but without modification by PE_{g-MAH}, respectively. Moreover, the minimal T_m (or evaluated l_c) values obtained for $F_{100}\text{FNSI}^{100}_{m3-0.075}$, $F_{100}\text{FNSI}^{300}_{m6-0.05}$, and $F_{100}\text{FNSI}^{600}_{m9-0.0375}$ as-prepared fibers prepared at the optimal FNSI^x_{my} contents and weight ratio of PE_{g-MAH} to NSI^x, respectively, reduced significantly as the specific surface

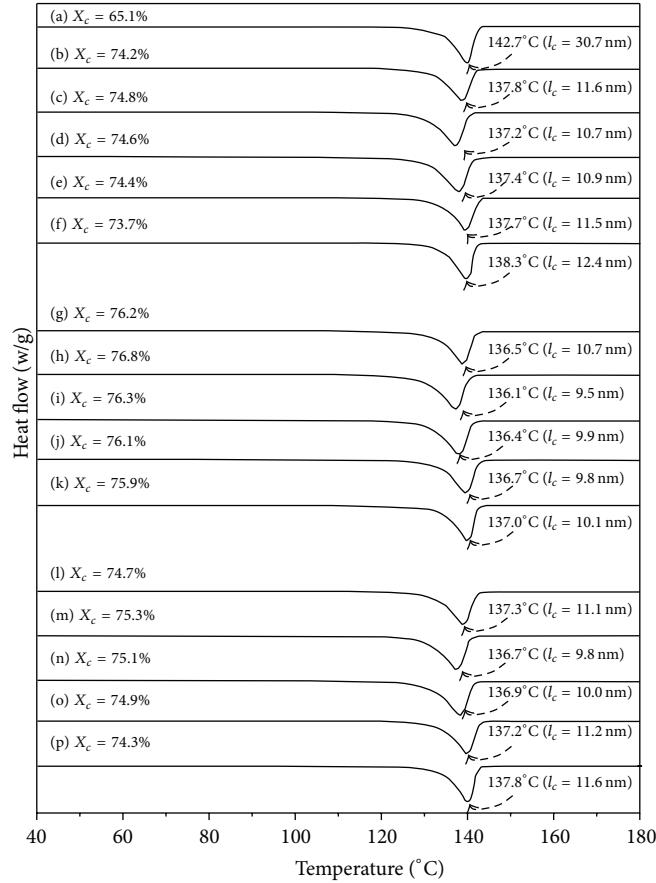


FIGURE 4: DSC thermograms of (a) F_{100} , (b) $F_{100}FNSI_{m3-0.025}^{600}$, (c) $F_{100}FNSI_{m3-0.0375}^{600}$, (d) $F_{100}FNSI_{m3-0.05}^{600}$, (e) $F_{100}FNSI_{m3-0.0625}^{600}$, (f) $F_{100}FNSI_{m3-0.075}^{600}$, (g) $F_{100}FNSI_{m9-0.025}^{600}$, (h) $F_{100}FNSI_{m9-0.0375}^{600}$, (i) $F_{100}FNSI_{m9-0.05}^{600}$, (j) $F_{100}FNSI_{m9-0.0625}^{600}$, (k) $F_{100}FNSI_{m9-0.075}^{600}$, (l) $F_{100}FNSI_{m12-0.025}^{600}$, (m) $F_{100}FNSI_{m12-0.0375}^{600}$, (n) $F_{100}FNSI_{m12-0.05}^{600}$, (o) $F_{100}FNSI_{m12-0.0625}^{600}$, and (p) $F_{100}FNSI_{m12-0.075}^{600}$ as-prepared fibers.

areas of $FNSI_{my}^x$ particles increased, while the highest X_c values obtained for $F_{100}FNSI_{m3-0.075}^{100}$, $F_{100}FNSI_{m6-0.05}^{300}$, and $F_{100}FNSI_{m9-0.0375}^{600}$ as-prepared fibers increased consistently as the specific surface areas of their $FNSI_{my}^x$ particles increased.

3.5. Achievable Draw Ratios of the As-Prepared Fibers.

Figure 5 summarized the achievable draw ratio (achievable λ) values of F_{100} , $F_{100}NSI_z^x$, and $F_{100}FNSI_{my-z}^x$ as-prepared fiber specimens prepared at varying NSI_z^x and/or $FNSI_{my}^x$ contents, respectively. For comparison purposes, achievable λ values of the best prepared UHMWPE/functionalized carbon nanotube (FCNT) as-prepared fibers (i.e., $F_{100}C_{f2-0.1}$ specimens) obtained in our previous investigations [24] were also summarized in Figure 5, in which, functionalized carbon nanotubes are with relatively high (i.e., $272.7 \text{ m}^2/\text{g}$) but significantly lower specific surface areas than those of $FNSI_{my}^{300}$ and $FNSI_{my}^{600}$ particles prepared in this study. After addition with NSI_z^x and/or $FNSI_{my}^x$ particles in UHMWPE, the achievable λ values of $F_{100}NSI_z^x$ and/or $F_{100}FNSI_{my-z}^x$ as-prepared fibers increased initially and reached a maximal value as their NSI_z^x and/or $FNSI_{my}^x$ contents approached an optimal value, respectively, in which the

achievable λ values of $F_{100}FNSI_{my-0.075}^{100}$, $F_{100}FNSI_{my-0.05}^{300}$, and $F_{100}FNSI_{my-0.0375}^{600}$ as-prepared fibers prepared at the optimal $FNSI_{my}^x$ contents at 0.075, 0.05, and 0.0375 phr, respectively, were significantly higher than those of the corresponding $F_{100}NSI_{0.1}^{100}$, $F_{100}NSI_{0.0625}^{300}$, and $F_{100}NSI_{0.05}^{600}$ as-prepared fibers prepared at the optimal NSI_z^x contents at 0.1, 0.0625, and 0.05 phr, respectively. Moreover, it is worth noting that $F_{100}FNSI_{my-0.075}^{100}$, $F_{100}FNSI_{my-0.05}^{300}$, and $F_{100}FNSI_{my-0.0375}^{600}$ as-prepared fibers prepared at the optimal $FNSI_{my}^x$ contents exhibited other maximal achievable λ values at 176, 289, and 361, respectively, as their $FNSI_{my}^{100}$, $FNSI_{my}^{300}$, and $FNSI_{my}^{600}$ particles were modified using an optimal weight ratio of PE_{g-MAH} to NSI^{100} , NSI^{300} , and NSI^{600} at 3, 6, and 9, respectively. It is further interesting to note that the highest achievable λ values obtained for the best prepared $F_{100}FNSI_{m3-0.075}^{100}$, $F_{100}FNSI_{m6-0.05}^{300}$, and $F_{100}FNSI_{m9-0.0375}^{600}$ as-prepared fibers prepared at the optimal $FNSI_{my}^x$ contents and weight ratios of PE_{g-MAH} to NSI_z^x improved significantly as the specific surface areas of their $FNSI_{my}^x$ particles increased. In fact, the maximal achievable λ value (i.e., 361) obtained for $F_{100}FNSI_{m9-0.0375}^{600}$

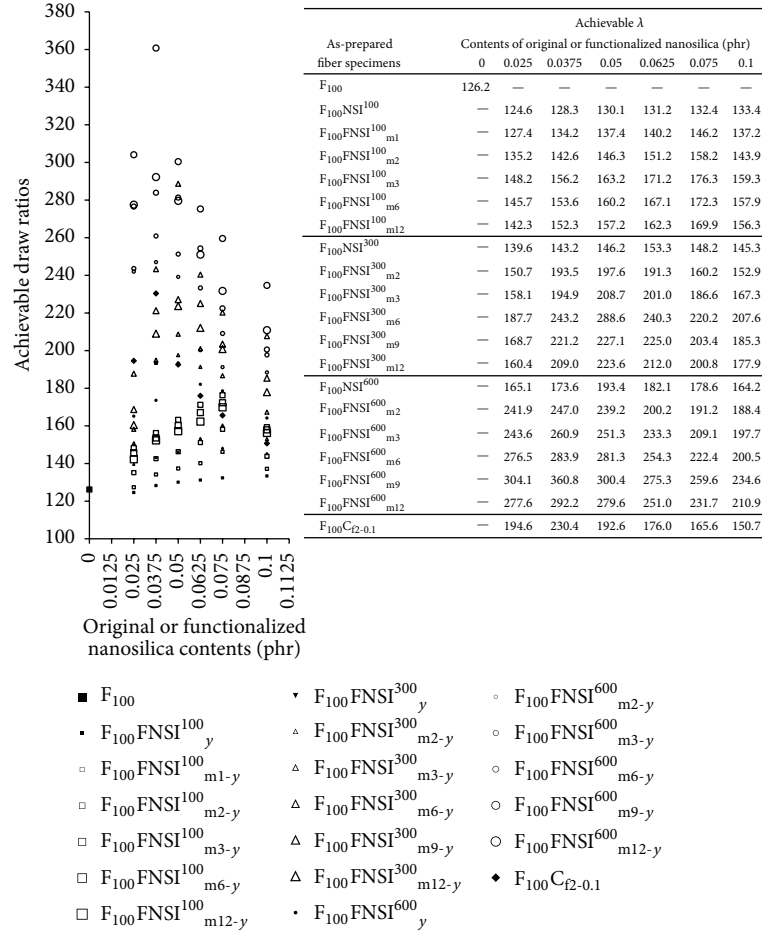


FIGURE 5: Achievable draw ratios as-prepared fibers.

as-prepared fiber is about 2.05 and 1.25 times of those of F₁₀₀FNSI¹⁰⁰_{m3-0.075} and the best prepared UHMWPE/FCNT as-prepared fibers and is 2.85 times of that of F₁₀₀ as-prepared fiber without addition of original and/or modified nanosilica particles.

3.6. Orientation Factor Analyses of the As-Prepared and Drawn Fiber Specimens. Typical orientation factor (f_0) values of F₁₀₀, F₁₀₀NSI^x_z, and F₁₀₀FNSI^x_{my-z} as-prepared and drawn fibers are summarized in Figure 6. No significant difference in f_0 values was found for F₁₀₀, F₁₀₀NSI^x_z, and F₁₀₀FNSI^x_{my-z} as-prepared fibers. As expected, f_0 values of F₁₀₀, F₁₀₀NSI^x_z, and F₁₀₀FNSI^x_{my-z} fibers increased consistently as their draw ratios increased. After addition of NSI^x_z and/or FNSI^x_{my-z} particles, f_0 values of drawn F₁₀₀NSI^x_z and/or F₁₀₀FNSI^x_{my-z} fibers were significantly higher than those of drawn F₁₀₀ fibers with the same draw ratios. f_0 values of drawn F₁₀₀NSI^x_z fibers with a fixed draw ratio reached a maximal value as their NSI¹⁰⁰, NSI³⁰⁰, and NSI⁶⁰⁰ contents approached the optimal values at 0.1, 0.0625, and 0.05 phr, respectively. Similarly, f_0 values of each drawn F₁₀₀FNSI^x_{my-z} fiber series specimen reached a maximal value as their FNSI¹⁰⁰_{my}, FNSI³⁰⁰_{my},

and FNSI⁶⁰⁰_{my} contents approached an optimal value at 0.075, 0.05, and 0.0375 phr, respectively, in which, f_0 values of drawn F₁₀₀FNSI¹⁰⁰_{my-0.075}, F₁₀₀FNSI³⁰⁰_{my-0.05}, and F₁₀₀FNSI⁶⁰⁰_{my-0.0375} fibers prepared at the optimal FNSI^x_{my} contents were significantly higher than those of the corresponding drawn F₁₀₀NSI¹⁰⁰_{0.1}, F₁₀₀NSI³⁰⁰_{0.0625}, and F₁₀₀NSI⁶⁰⁰_{0.05} fibers prepared with the same draw ratios and at an optimal NSI^x content, respectively. Moreover, it is worth noting that F₁₀₀FNSI¹⁰⁰_{my-0.075}, F₁₀₀FNSI³⁰⁰_{my-0.05}, and F₁₀₀FNSI⁶⁰⁰_{my-0.0375} drawn fibers prepared at the optimal FNSI^x_{my} contents exhibited other maximal f_0 values as their FNSI¹⁰⁰_{my}, FNSI³⁰⁰_{my}, and FNSI⁶⁰⁰_{my} particles were modified using an optimal weight ratio of PE_{g-MAH} to NSI¹⁰⁰, NSI³⁰⁰, and NSI⁶⁰⁰ at 3, 6, and 9, respectively. It is further interesting to note that the maximal f_0 values obtained for the best prepared F₁₀₀FNSI¹⁰⁰_{m3-0.075}, F₁₀₀FNSI³⁰⁰_{m6-0.05}, and F₁₀₀FNSI⁶⁰⁰_{m9-0.0375} as-prepared fibers prepared at the optimal FNSI^x_{my} contents and weight ratios of PE_{g-MAH} to NSI^x improved significantly as the specific surface areas of their FNSI^x_{my} particles increased.

As evidenced by thermal and lamellar thickness analyses, T_m (or evaluated l_c) values of F₁₀₀NSI^x_z and/or

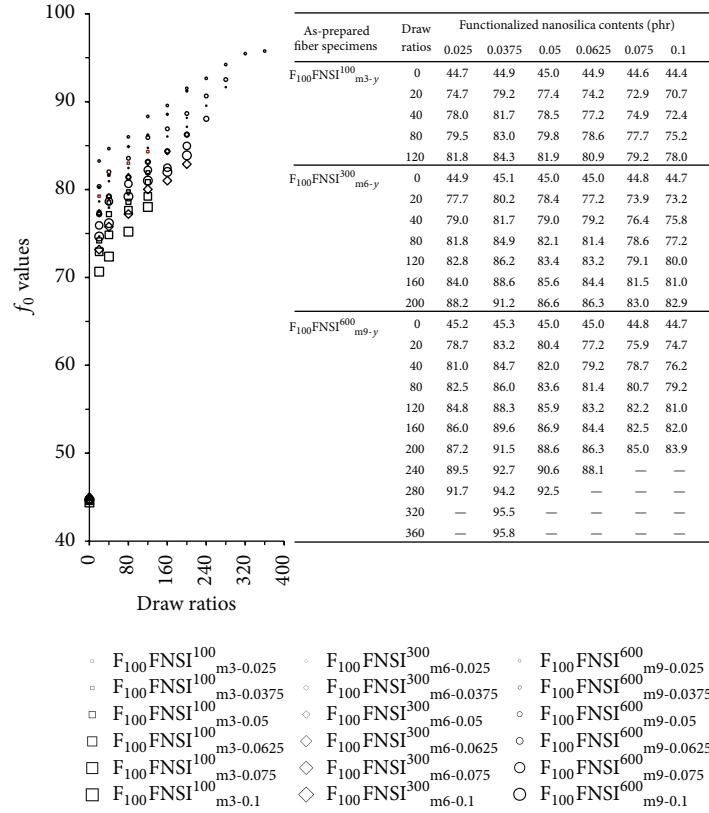


FIGURE 6: The orientation factor (f_0) values as-prepared and drawn fibers with varying draw ratios.

F₁₀₀FNSI^x_{my-z} as-prepared fibers reduced to a minimal value, as their NSI^x and/or FNSI^x_{my} contents reached an optimal value, respectively. Moreover, the lowest T_m (or evaluated l_c) values obtained for the best prepared F₁₀₀FNSI¹⁰⁰_{m3-0.075}, F₁₀₀FNSI³⁰⁰_{m6-0.05}, and F₁₀₀FNSI⁶⁰⁰_{m9-0.0375} as-prepared fibers prepared at the optimal FNSI^x_{my} contents and weight ratio of PE_{g-MAH} to NSI^x reduced significantly as the specific surface areas of their FNSI^x_{my} particles increased. Presumably, these crystals with lower T_m and/or evaluated l_c values can be melted and pulled out of folded lamellar crystals relatively easily during the ultradrawing processes, and hence this results in higher drawability and orientation of the best prepared F₁₀₀FNSI¹⁰⁰_{m3-0.075}, F₁₀₀FNSI³⁰⁰_{m6-0.05}, and F₁₀₀FNSI⁶⁰⁰_{m9-0.0375} fibers, in which, the drawability and orientation of the best prepared fibers improved significantly as the specific surface areas of FNSI¹⁰⁰_{m3}, FNSI³⁰⁰_{m6}, and FNSI⁶⁰⁰_{m9} present in F₁₀₀FNSI¹⁰⁰_{m3-0.075}, F₁₀₀FNSI³⁰⁰_{m6-0.05}, and F₁₀₀FNSI⁶⁰⁰_{m9-0.0375} as-prepared and/or drawn fibers increased. However, the amounts of coagulated NSI^x and/or FNSI^x_{my} particles are likely to increase significantly when their NSI^x and/or FNSI^x_{my} contents are higher than certain values, respectively. These coagulated NSI^x and/or FNSI^x_{my} particles can slide against each other and serve as the defects for stress concentration during the drawing processes of F₁₀₀NSI^x_z and F₁₀₀FNSI^x_{my-z} as-prepared fibers and hence lead to an early breakage and/or significant reduction in achievable λ and f_0 values of the resulting drawn fibers.

Based on these premises, it is reasonable to understand that the achievable λ values of F₁₀₀NSI^x_z and F₁₀₀FNSI^x_{my-z} as-prepared fibers and f_0 values of the drawn F₁₀₀NSI^x_z and F₁₀₀FNSI^x_{my-z} fibers with a fixed draw ratio reduce significantly when their NSI^x and/or FNSI^x_{my} contents are higher than the specific optimal value, respectively.

3.7. Morphological Analyses of the As-Prepared and Drawn Fibers. Figure 7 exhibits typical SEM micrographs of the as-prepared and drawn F₁₀₀, F₁₀₀FNSI¹⁰⁰_{m3-0.075}, F₁₀₀FNSI³⁰⁰_{m6-0.05}, and F₁₀₀FNSI⁶⁰⁰_{m9-0.0375} fibers with various draw ratios. Many demarcated drawn “micro-fibrils” were found paralleling the drawing direction of the drawn F₁₀₀, F₁₀₀FNSI¹⁰⁰_{m3-0.075}, F₁₀₀FNSI³⁰⁰_{m6-0.05}, and F₁₀₀FNSI⁶⁰⁰_{m9-0.0375} fibers as their draw ratios increased, wherein the thicknesses of these drawn micro-fibrils reduced significantly as the draw ratios increased. Moreover, more and thinner “micro-fibrils” were found on the surfaces of F₁₀₀FNSI¹⁰⁰_{m3-0.075}, F₁₀₀FNSI³⁰⁰_{m6-0.05}, and F₁₀₀FNSI⁶⁰⁰_{m9-0.0375} as-prepared and/or drawn fibers with the same draw ratio as the specific surface areas of their FNSI¹⁰⁰_{m3}, FNSI³⁰⁰_{m6}, and FNSI⁶⁰⁰_{m9} particles increased.

It is not completely clear what accounts for the interesting demarcated “micro-fibril” morphology found on the surfaces of F₁₀₀, F₁₀₀FNSI¹⁰⁰_{m3-0.075}, F₁₀₀FNSI³⁰⁰_{m6-0.05}, and F₁₀₀FNSI⁶⁰⁰_{m9-0.0375} as-prepared and drawn fibers. Presumably, during the ultradrawing processes, many of

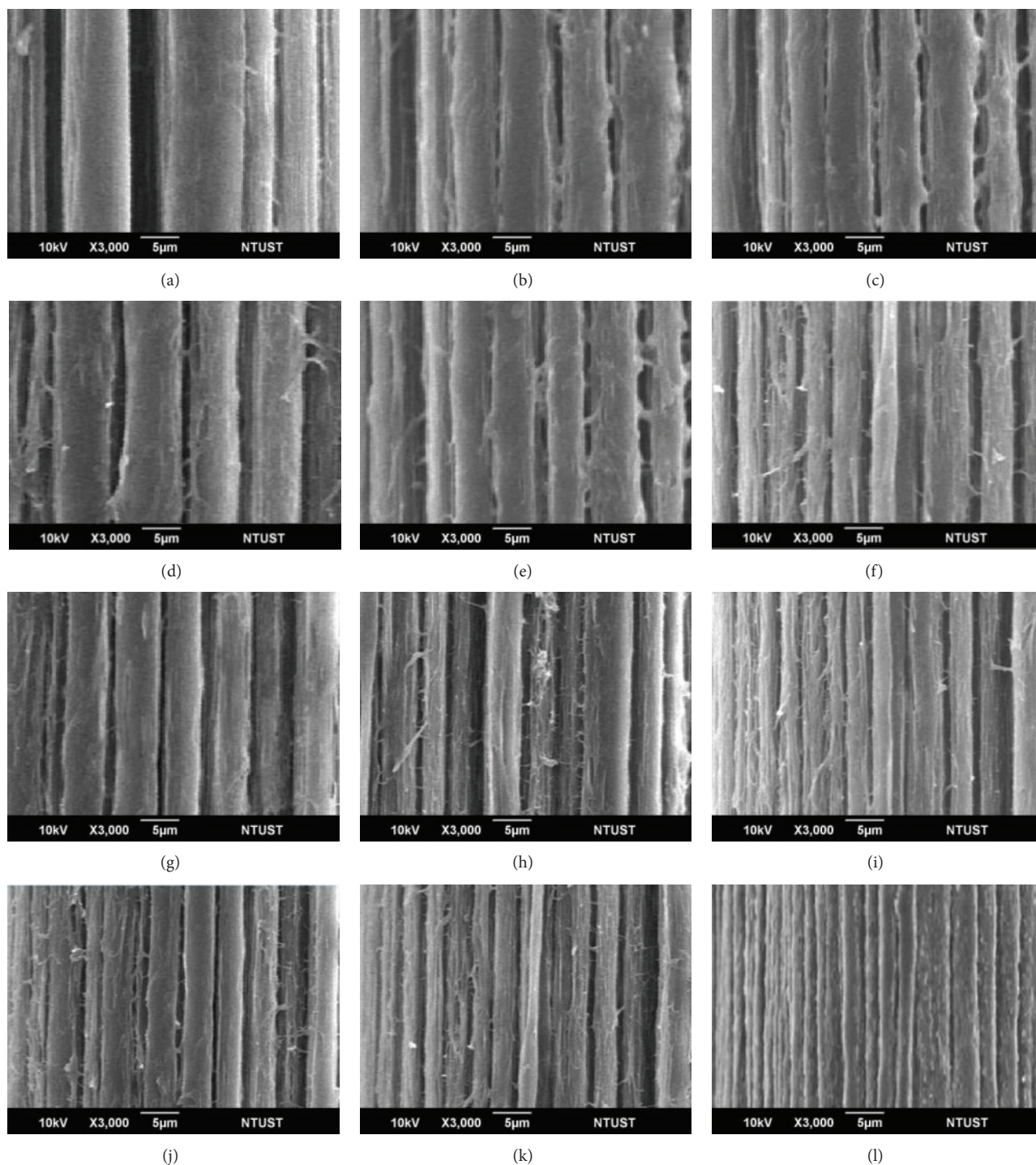


FIGURE 7: SEM micrographs of F_{100} fibers with a draw ratio of (a) 1, (b) 50, and (c) 100; $F_{100}FNSI^{100}$ fibers with a draw ratio of (d) 1, (e) 50, and (f) 100; $F_{100}FNSI^{300}$ fibers with a draw ratio of (g) 1, (h) 50, and (i) 100; and $F_{100}FNSI^{600}$ fibers with a draw ratio of (j) 1, (k) 50, and (l) 100.

the UHMWPE kebab crystals with relatively thinner lamellar thickness values can be unfolded and pulled out of the crystal lamellae in an easier way than those kebab crystals with thicker lamellar thickness values. The unfolded UHMWPE molecules pulled out from the kebab lamellae can then gradually transform into the oriented “micro-fibrils” during

their ultradrawing processes. As evidenced by DSC analyses in the previous section, T_m (or evaluated l_c) values of $F_{100}NSI^x_z$ and/or $F_{100}FNSI^x_{my-z}$ as-prepared fibers were significantly lower than that of F_{100} as-prepared fiber and reached a minimal value, as their NSI^x and/or $FNSI^x_{my}$ contents approached an optimal value, respectively, in

which, the lowest T_m (or evaluated l_c) values obtained for the best prepared $F_{100}FNSI^{100}_{m3-0.075}$, $F_{100}FNSI^{300}_{m6-0.05}$, and $F_{100}FNSI^{600}_{m9-0.0375}$ as-prepared fibers prepared at the optimal $FNSI^x_{my}$ contents and weight ratio of PE_{g-MAH} to NSI^x reduced significantly as the specific surface areas of their $FNSI^x_{my}$ particles increased. Based on these premises, it is reasonable to infer that the “micro-fibrils” found on the surfaces of as-prepared and/or drawn $F_{100}FNSI^{100}_{m3-0.075}$, $F_{100}FNSI^{300}_{m6-0.05}$, and $F_{100}FNSI^{600}_{m9-0.0375}$ fibers are more and thinner than those of the corresponding as-prepared and/or drawn F_{100} fibers with the same draw ratios but without addition of any “nuclear” nanofillers. By the same analogy, more and thinner “micro-fibrils” are expected to be found on the surfaces of $F_{100}FNSI^{100}_{m3-0.075}$, $F_{100}FNSI^{300}_{m6-0.05}$, and $F_{100}FNSI^{600}_{m9-0.0375}$ as-prepared and/or drawn fibers as the specific surface areas of their $FNSI^x_{my}$ particles increased.

3.8. Tensile Properties. Tensile strength (σ_f) and modulus (E) values of F_{100} , $F_{100}NSI^x_z$, and $F_{100}FNSI^x_{my-z}$ as-prepared fibers prepared at varying draw ratios are illustrated in Table 3. For comparison purposes, σ_f and E values of the best prepared UHMWPE/FCNT (i.e., $F_{100}C_{f2-0.1}$) as-prepared fiber obtained in our previous investigation [24] were also summarized in Table 3. As expected, σ_f and E values of the drawn F_{100} , $F_{100}NSI^x_z$, and $F_{100}FNSI^x_{my-z}$ fibers improve consistently as their draw ratios increase. It is worth noting that σ_f and E values of drawn $F_{100}NSI^x_z$ and $F_{100}FNSI^x_{my-z}$ fibers are significantly higher than those of the corresponding drawn F_{100} fibers with the same draw ratio but without addition of NSI^x and/or $FNSI^x_{my}$ particles. Similar to those found for their f_0 values, σ_f and E values of drawn $F_{100}NSI^x_z$ and $F_{100}FNSI^x_{my-z}$ fibers reach a maximal value as their NSI^x and/or $FNSI^x_{my}$ contents approach the optimal values at 0.075, 0.05, and 0.0375 phr, respectively, in which σ_f and E values of drawn $F_{100}FNSI^{100}_{my-0.075}$, $F_{100}FNSI^{300}_{my-0.05}$, and $F_{100}FNSI^{600}_{my-0.0375}$ fibers prepared at their optimal $FNSI^x_{my}$ contents are significantly higher than those of the corresponding drawn $F_{100}NSI^{100}_{0.1}$, $F_{100}NSI^{300}_{0.0625}$, and $F_{100}NSI^{600}_{0.05}$ fibers with the same draw ratio and an optimal NSI^x content at 0.1, 0.0625, and 0.05 phr, respectively. Moreover, at a fixed draw ratio, drawn $F_{100}FNSI^{100}_{my-0.075}$, $F_{100}FNSI^{300}_{my-0.05}$, and $F_{100}FNSI^{600}_{my-0.0375}$ fibers prepared at the optimal $FNSI^x_{my}$ contents exhibited other maximal σ_f and E values, as their $FNSI^{100}_{my}$, $FNSI^{300}_{my}$, and $FNSI^{600}_{my}$ particles were modified using an optimal weight ratio of PE_{g-MAH} to NSI^{100} , NSI^{300} , and NSI^{600} at 3, 6, and 9, respectively. It is interesting to note that the maximal σ_f and E values obtained for the best prepared $F_{100}FNSI^{100}_{m3-0.075}$, $F_{100}FNSI^{300}_{m6-0.05}$, and $F_{100}FNSI^{600}_{m9-0.0375}$ drawn fibers prepared at the optimal $FNSI^x_{my}$ contents and weight ratio of PE_{g-MAH} to NSI^x increased significantly as the specific surface areas of $FNSI^x_{my}$ particles increased. For instance, the ultimate σ_f values of best prepared $F_{100}FNSI^{100}_{m3-0.075}$,

$F_{100}C_{f2-0.1}$, $F_{100}FNSI^{300}_{m6-0.05}$, and $F_{100}FNSI^{600}_{m9-0.0375}$ fibers reached 4.4, 5.1, 7.1, and 7.6 GPa, respectively, as the specific surface areas of $FNSI^{100}_{m3}$, FCNT, $FNSI^{300}_{my6}$, and $FNSI^{600}_{m9}$ particles increased from 129.8 to 272.7, 335.8 and to 630.7 m^2/g , respectively. The ultimate σ_f value of the best prepared $F_{100}FNSI^{600}_{m9-0.0375}$ drawn fiber is about 1.7 and 1.5 times of those of the $F_{100}FNSI^{100}_{m3-0.075}$ and the best prepared UHMWPE/FCNT drawn fiber specimens, respectively, and is about 2.3 times of that of the best prepared UHMWPE drawn fibers prepared at the same optimal UHMWPE concentration and drawing condition but without addition of any nanofiller.

The mechanical properties of the drawn specimens are generally believed to depend mainly on the degree of orientation of the drawn specimens, as their molecular weights are constant [16, 34]. As evidenced by orientation analyses in the previous section, at a fixed draw ratio, f_0 values of drawn $F_{100}FNSI^{100}_{my-0.075}$, $F_{100}FNSI^{300}_{my-0.05}$, and $F_{100}FNSI^{600}_{my-0.0375}$ fibers prepared at the optimal $FNSI^x_{my}$ contents were significantly higher than those of the corresponding $F_{100}NSI^{100}_{0.1}$, $F_{100}NSI^{300}_{0.0625}$, and $F_{100}NSI^{600}_{0.05}$ fibers prepared at an optimal NSI^x content, respectively. Moreover, f_0 values of $F_{100}FNSI^{100}_{m3-0.075}$, $F_{100}FNSI^{300}_{m6-0.05}$, and $F_{100}FNSI^{600}_{m9-0.0375}$ drawn fibers were always higher than those of other $F_{100}FNSI^{100}_{my-0.075}$, $F_{100}FNSI^{300}_{my-0.05}$, and $F_{100}FNSI^{600}_{my-0.0375}$ fibers prepared with the same draw ratios and $FNSI$ contents but modified using an optimal weight ratio of PE_{g-MAH} to NSI^{100} , NSI^{300} , and NSI^{600} other than 3, 6, and 9, respectively. In fact, the maximal f_0 values obtained for the best prepared $F_{100}FNSI^{100}_{m3-0.075}$, $F_{100}FNSI^{300}_{m6-0.05}$, and $F_{100}FNSI^{600}_{m9-0.0375}$ drawn fibers improved significantly as the specific surface areas of their $FNSI^x_{my}$ particles increased. These results clearly suggest that a good orientation of UHMWPE molecules along the drawing direction positively affects the tensile properties of F_{100} , $F_{100}NSI^x_z$, and $F_{100}FNSI^x_{my-z}$ fibers. Excellent orientation and ultimate tensile properties of UHMWPE/nanofiller fibers can be prepared by the ultradrawing of $F_{100}FNSI^x_{my-z}$ as-prepared fibers with optimal contents of the best prepared $FNSI^{100}_{m3}$, $FNSI^{300}_{m6}$, and $FNSI^{600}_{m9}$ particles well dispersing in their as-prepared fibers. Moreover, the specific surface areas of well-dispersed functionalized nanofillers in UHMWPE/functionalized nanofiller fibers can positively affect their ultradrawing, orientation, ultimate tensile properties, and “micro-fibrils” morphologies.

4. Conclusions

As evidenced by FTIR and TEM analyses, PE_{g-MAH} molecules were successfully grafted onto nanosilica particles with varying specific surface areas through the reaction of the hydroxyl groups of nanosilica particles with the maleic anhydride groups of PE_{g-MAH} molecules during their functionalized processes. The specific surface areas of $FNSI^{100}_{my}$, $FNSI^{300}_{my}$, and $FNSI^{600}_{my}$ functionalized nanosilica particles reached a maximal value at 129.8, 335.8,

TABLE 3: Tensile strength (σ_f) and modulus values (E) of UHMWPE (F_{100}), UHMWPE/functionalized nanosilica ($F_{100}\text{FNSI}^x_{my-z}$), and UHMWPE/carbon nanotube ($F_{100}\text{C}_{f2-0.1}$) fiber specimens with varying draw ratios.

Draw ratio	Specimen									
	F_{100}		$F_{100}\text{C}_{f2-0.1}$		$F_{100}\text{FNSI}^{100}_{m2-0.625}$		$F_{100}\text{FNSI}^{100}_{m2-0.075}$		$F_{100}\text{FNSI}^{100}_{m2-0.1}$	
	σ_f (GPa)	E (GPa)	σ_f (GPa)	E (GPa)	σ_f (GPa)	E (GPa)	σ_f (GPa)	E (GPa)	σ_f (GPa)	E (GPa)
20	1.6	58.0	2.7	106.3	2.1	61.1	2.2	69.0	2.1	59.0
40	1.9	71.2	3.5	140.5	2.6	80.7	2.8	90.3	2.8	77.8
60	2.6	92.9	4.2	169.8	3.4	105.2	3.6	119.0	3.5	101.4
120	3.4	112.5	4.9	194.5	4.0	118.5	4.2	130.2	4.0	115.9
160	—	—	5.1	204.6	4.4	163.3	4.8	184.3	4.5	152.3
Draw ratio	Specimen									
	$F_{100}\text{FNSI}^{100}_{m3-0.625}$		$F_{100}\text{FNSI}^{100}_{m3-0.075}$		$F_{100}\text{FNSI}^{100}_{m3-0.1}$		$F_{100}\text{FNSI}^{100}_{m6-0.625}$		$F_{100}\text{FNSI}^{100}_{m6-0.075}$	
	σ_f (GPa)	E (GPa)	σ_f (GPa)	E (GPa)	σ_f (GPa)	E (GPa)	σ_f (GPa)	E (GPa)	σ_f (GPa)	E (GPa)
20	2.4	73.1	2.5	81.0	2.4	71.0	2.2	67.1	2.3	75.0
40	2.9	92.7	3.1	102.3	3.1	89.8	2.7	86.7	2.9	96.3
60	3.7	117.2	3.9	131.0	3.8	113.4	3.5	111.2	3.7	125.0
120	4.3	130.5	4.5	142.2	4.3	127.9	4.1	124.5	4.3	136.2
160	4.6	175.3	5.0	196.3	4.8	164.3	4.4	169.3	4.8	190.3
Draw ratio	Specimen									
	$F_{100}\text{FNSI}^{100}_{m6-0.1}$		$F_{100}\text{FNSI}^{300}_{m3-0.375}$		$F_{100}\text{FNSI}^{300}_{m3-0.5}$		$F_{100}\text{FNSI}^{300}_{m3-0.075}$		$F_{100}\text{FNSI}^{300}_{m6-0.375}$	
	σ_f (GPa)	E (GPa)	σ_f (GPa)	E (GPa)	σ_f (GPa)	E (GPa)	σ_f (GPa)	E (GPa)	σ_f (GPa)	E (GPa)
20	2.2	65.0	2.5	79.3	2.6	84.2	2.3	75.9	2.9	93.3
40	2.9	83.8	3.2	108.3	3.3	112.9	2.8	102.9	3.6	122.3
60	3.6	107.4	4.1	151.7	4.2	156.7	3.9	147.0	4.5	165.7
120	4.1	121.9	4.7	172.7	4.9	176.9	4.4	167.6	5.1	186.7
160	4.6	158.3	5.7	184.9	5.8	187.9	5.5	183.9	6.1	198.9
200	—	—	6.0	188.1	6.1	192.6	5.9	189.2	6.4	202.1
Draw ratio	Specimen									
	$F_{100}\text{FNSI}^{300}_{m6-0.5}$		$F_{100}\text{FNSI}^{300}_{m6-0.075}$		$F_{100}\text{FNSI}^{300}_{m9-0.375}$		$F_{100}\text{FNSI}^{300}_{m9-0.5}$		$F_{100}\text{FNSI}^{300}_{m9-0.075}$	
	σ_f (GPa)	E (GPa)	σ_f (GPa)	E (GPa)	σ_f (GPa)	E (GPa)	σ_f (GPa)	E (GPa)	σ_f (GPa)	E (GPa)
20	3.0	98.2	2.7	89.9	2.6	86.3	2.7	91.2	2.4	82.9
40	3.7	126.9	3.2	116.9	3.3	115.3	3.4	119.9	2.9	109.9
60	4.6	170.7	4.3	161.0	4.2	158.7	4.3	163.7	4.0	154.0
120	5.3	190.9	4.8	181.6	4.8	179.7	5.0	183.9	4.5	174.6
160	6.2	201.9	5.9	197.9	5.8	191.9	5.9	194.9	5.6	190.9
200	6.5	206.6	6.3	203.2	6.1	195.1	6.2	199.6	6.0	196.2
Draw ratio	Specimen									
	$F_{100}\text{FNSI}^{600}_{m6-0.025}$		$F_{100}\text{FNSI}^{600}_{m6-0.0375}$		$F_{100}\text{FNSI}^{600}_{m6-0.05}$		$F_{100}\text{FNSI}^{600}_{m9-0.025}$		$F_{100}\text{FNSI}^{600}_{m9-0.0375}$	
	σ_f (GPa)	E (GPa)	σ_f (GPa)	E (GPa)	σ_f (GPa)	E (GPa)	σ_f (GPa)	E (GPa)	σ_f (GPa)	E (GPa)
20	2.5	93.5	2.8	101.2	2.6	96.5	2.9	109.5	3.2	117.2
40	3.2	116.7	3.5	128.1	3.3	126.1	3.6	132.7	3.9	144.1
60	4.3	156.8	4.4	163.4	4.3	158.8	4.7	172.8	4.8	179.4
120	4.9	181.5	5.2	190.8	5.0	184.1	5.3	197.5	5.6	206.8
160	6.0	221.2	6.2	227.4	6.1	223.9	6.4	237.2	6.6	243.4
200	6.2	230.5	6.4	236.4	6.4	234.8	6.6	246.5	6.8	252.4
240	6.5	239.7	6.6	245.7	6.5	241.4	6.9	255.7	7.0	261.7
280	6.6	244.9	6.8	247.2	6.6	245.0	7.0	260.9	7.1	263.2
320	—	—	—	—	—	—	—	—	7.2	266.0
360	—	—	—	—	—	—	—	—	7.4	273.7

TABLE 3: Continued.

Draw ratio	Specimen								—
	$F_{100}\text{FNSI}^{600}_{m9-0.05}$		$F_{100}\text{FNSI}^{600}_{m12-0.025}$		$F_{100}\text{FNSI}^{600}_{m12-0.0375}$		$F_{100}\text{FNSI}^{600}_{m12-0.05}$		
	σ_f (GPa)	E (GPa)	σ_f (GPa)	E (GPa)	σ_f (GPa)	E (GPa)	σ_f (GPa)	E (GPa)	—
20	3.0	112.5	2.4	100.5	3.0	108.2	2.8	103.5	—
40	3.8	142.1	3.4	123.7	3.7	135.1	3.6	133.1	—
60	4.7	174.8	4.5	163.8	4.6	170.4	4.5	165.8	—
120	5.4	200.1	5.1	188.5	5.4	197.8	5.2	191.1	—
160	6.5	239.9	6.2	228.2	6.4	234.4	6.3	230.9	—
200	6.8	250.8	6.4	237.5	6.6	243.4	6.6	241.8	—
240	6.9	257.4	6.7	246.7	6.8	252.7	6.7	248.4	—
280	7.0	261.0	6.8	251.9	6.9	254.2	6.8	252.0	—
320	—	—	—	—	7.0	257.0	—	—	—

and $630.7 \text{ m}^2/\text{g}$, respectively, as the weight ratios of $\text{PE}_{g\text{-MAH}}$ to NSI^{100} , NSI^{300} , and NSI^{600} nanosilica particles of FNSI^{100}_{my} , FNSI^{300}_{my} , and FNSI^{600}_{my} functionalized nanosilica particles approached an optimal value at 3, 6, and 9, respectively. The specific surface areas of well-dispersed functionalized nanosilica particles in UHMWPE/functionalized nanosilica fibers were found to affect positively on the achievable λ , percentage crystallinity, ultimate tensile strength values, and “micro-fibrils” morphologies of the UHMWPE/functionalized nanosilica as-prepared fibers. The achievable λ values of the best prepared UHMWPE/functionalized nanosilica as-prepared fibers (i.e., $F_{100}\text{FNSI}^{100}_{m3-0.075}$, $F_{100}\text{FNSI}^{300}_{m6-0.05}$, and $F_{100}\text{FNSI}^{600}_{m9-0.0375}$) improved consistently from 176 to 289 and 361, as the specific surface areas of the incorporated functionalized nanosilica particles increased from 129.8 to 335.8 and $630.7 \text{ m}^2/\text{g}$, respectively. Similar to those found for the achievable drawing properties of the best prepared UHMWPE/functionalized nanosilica as-prepared fibers, the orientation factor, ultimate σ_f and E values of the best prepared UHMWPE/functionalized nanosilica drawn fibers (i.e., $F_{100}\text{FNSI}^{100}_{m3-0.075}$, $F_{100}\text{FNSI}^{300}_{m6-0.05}$, and $F_{100}\text{FNSI}^{600}_{m9-0.0375}$) with a fixed draw improved positively, as the specific surface areas of added functionalized nanosilica particles increased from 129.8 to 335.8 and $630.7 \text{ m}^2/\text{g}$. For instance, the ultimate σ_f values of the best prepared UHMWPE/functionalized nanosilica drawn fibers improved significantly from 4.4 to 7.1 and 7.6 GPa, respectively, as the specific surface areas of functionalized nanosilica particles increased from 129.8 to 335.8 and $630.7 \text{ m}^2/\text{g}$, respectively. The maximal ultimate σ_f value (i.e., 7.6 GPa) of the best prepared UHMWPE/functionalized nanosilica drawn fiber with the highest specific surface area of functionalized nanosilica is about 2.3 times of that of the best prepared UHMWPE drawn fiber prepared at the same optimal UHMWPE concentration and drawing condition but without addition of any nanofiller. The “micro-fibrils” found on the surfaces of UHMWPE/functionalized nanosilica drawn fibers with the same draw ratio became more and thinner as the specific surface areas of their functionalized nanosilica particles increased. Possible reasons accounting

for the above interesting properties were reported in this study.

Conflict of Interests

The authors declare that there is no conflict of interests regarding the publication of this paper.

Acknowledgments

The authors would like to express their appreciation to the Department of Industrial Technology, Ministry of Economic Affairs (99-EC-17-A-11-SI-155, 100-EC-17-A-11-SI-155, and 101-EC-17-A-11-SI-155), and National Science Council (NSC 99-2221-E-011-010-MY3 and NSC 102-2221-E-168-038-MY3) for support of this work.

References

- [1] K. Kajiwara and J. E. McIntyre, *Advanced Fibre Spinning Technology*, Woodhead Publishing, Cambridge, UK, 1994.
- [2] C. Xiao, Y. Zhang, S. An, and G. Jia, “Investigation on the thermal behaviors and mechanical properties of ultrahigh molecular weight polyethylene (UHMW-PE) fibers,” *Journal of Applied Polymer Science*, vol. 59, no. 6, pp. 931–935, 1996.
- [3] M. I. Abo El-Maaty, R. H. Olley, and D. C. Bassett, “On the internal morphologies of high-modulus polyethylene and polypropylene fibres,” *Journal of Materials Science*, vol. 34, no. 9, pp. 1975–1989, 1999.
- [4] K. Yamaura, M. Suzuki, M. Yamamoto, R. Shimada, and T. Tanigami, “Gelation of poly(vinyl alcohol)/phenol/water solutions and gel spinning,” *Journal of Applied Polymer Science*, vol. 58, no. 10, pp. 1787–1791, 1995.
- [5] X. Zhang, T. Liu, T. V. Sreekumar, S. Kumar, X. Hu, and K. Smith, “Gel spinning of PVA/SWNT composite fiber,” *Polymer*, vol. 45, no. 26, pp. 8801–8807, 2004.
- [6] O. Darras, R. Seguela, and F. Rietsch, “Dried gels from linear low-density polyethylene: morphology, thermal behavior, and mechanical properties,” *Journal of Polymer Science Part B: Polymer Physics*, vol. 30, no. 4, pp. 349–359, 1992.
- [7] J. Yeh and S. Chang, “Ultradrawing behavior of gel films of ultrahigh molecular weight polyethylene and low molecular

- weight polyethylene blends at varying drawing conditions,” *Polymer Engineering & Science*, vol. 42, no. 7, pp. 1558–1567, 2002.
- [8] J.-T. Yeh, Y.-T. Lin, and H.-B. Jiang, “Drawing properties of ultrahigh molecular weight polyethylene fibers prepared at varying formation temperatures,” *Journal of Applied Polymer Science*, vol. 91, no. 3, pp. 1559–1570, 2004.
- [9] J. T. Yeh, Y. T. Lin, and K. N. Chen, “Ultradrawing properties of gel films of ultrahigh-molecular-weight polyethylene and low-molecular-weight polyethylene blends prepared at various formation temperatures,” *Journal of Applied Polymer Science*, vol. 89, no. 14, pp. 3728–3738, 2003.
- [10] P. Smith, H. D. Chanzy, and B. P. Rotzinger, “Drawing of virgin ultrahigh molecular weight polyethylene: an alternative route to high strength/high modulus materials,” *Journal of Materials Science*, vol. 22, no. 2, pp. 523–531, 1987.
- [11] P. Smith, H. D. Chanzy, and B. P. Rotzinger, “Drawing of virgin UHMW polyethylene: an alternative route to high strength/high modulus materials,” *Journal of Materials Science*, vol. 22, pp. 523–531, 1987.
- [12] M. Matsuo, C. Sawatari, M. Iida, and M. Yoneda, “Ultradrawing of high molecular weight polyethylene films produced by gelation/crystallization from solution: effect of the number of entanglements,” *Polymer Journal*, vol. 17, no. 11, pp. 1197–1208, 1985.
- [13] T. Kanamoto, A. Tsurta, K. Tanana, M. Takeda, and R. S. Porter, “Super-drawing of ultrahigh molecular weight polyethylene. 1. Effect of techniques on drawing of single crystal mats,” *Macromolecules*, vol. 21, no. 2, pp. 470–477, 1988.
- [14] J. Smook and A. J. Pennings, “The effect of temperature and deformation rate on the hot-drawing behavior of porous high-molecular-weight polyethylene fibers,” *Journal of Applied Polymer Science*, vol. 27, no. 6, pp. 2209–2228, 1982.
- [15] T. Jian, W.-D. Shyu, Y.-T. Lin, K.-N. Chen, and J.-T. Yeh, “Spinning and drawing properties of ultrahigh-molecular-weight polyethylene fibers prepared at varying concentrations and temperatures,” *Polymer Engineering and Science*, vol. 43, no. 11, pp. 1765–1777, 2003.
- [16] T. Ohta, “Review on processing ultra high tenacity fibers from flexible polymer,” *Polymer Engineering and Science*, vol. 23, no. 13, pp. 697–703, 1983.
- [17] D. C. Prevorsek, *Polymer Liquid Crystals*, Academic Press, London, UK, 1982.
- [18] B. Kalb and A. J. Pennings, “Hot drawing of porous high molecular weight polyethylene,” *Polymer*, vol. 21, no. 1, pp. 3–4, 1980.
- [19] M. A. Wilding and I. M. Ward, “Tensile creep and recovery in ultra-high modulus linear polyethylenes,” *Polymer*, vol. 19, no. 8, pp. 969–976, 1978.
- [20] P. Smith and P. J. Lemstra, “Ultra-high strength polyethylene filaments by solution spinning/drawing. 3. Influence of drawing temperature,” *Polymer*, vol. 21, no. 11, pp. 1341–1343, 1980.
- [21] S. Kavesh and D. C. Prevorsek, US Patent 4536536, 1985.
- [22] S. Kavesh and D. C. Prevorsek, “Producing high tenacity, high modulus crystalline article such as fiber or film,” US Patent 4551296, 1985.
- [23] S. Kavesh and D. C. Prevorsek, “High tenacity, high modulus polyethylene and polypropylene fibers and intermediates therefor,” US Patent 4413110, 1983.
- [24] J.-T. Yeh, T.-W. Wu, Y.-C. Lai et al., “Ultradrawing properties of ultra-high molecular weight polyethylene/functionalized carbon nanotube fibers,” *Polymer Engineering & Science*, vol. 51, no. 4, pp. 687–696, 2011.
- [25] J.-T. Yeh, C.-K. Wang, P. Hu, Y.-C. Lai, L.-K. Huang, and F.-C. Tsai, “Ultradrawing properties of ultrahigh-molecular-weight polyethylene/attapulgite fibers,” *Polymer International*, vol. 61, no. 6, pp. 982–989, 2012.
- [26] J.-T. Yeh, C.-K. Wang, A. Yeh et al., “Preparation and characterization of novel ultra-high molecular weight polyethylene composite fibers filled with nanosilica particles,” *Polymer International*, vol. 62, no. 4, pp. 591–600, 2013.
- [27] J. T. Yeh, C. C. Tsai, C. K. Wang, J. W. Shao, M. Z. Xiao, and S. C. Chen, “Ultradrawing novel ultra-high molecular weight polyethylene fibers filled with bacterial cellulose nanofibers,” *Carbohydrate Polymers*, vol. 101, pp. 1–10, 2014.
- [28] J. D. Hoffman and R. L. Miller, “Kinetic of crystallization from the melt and chain folding in polyethylene fractions revisited: theory and experiment,” *Polymer*, vol. 38, no. 13, pp. 3151–3212, 1997.
- [29] J. D. Hoffman and J. J. Weeks, “Rate of spherulitic crystallization with chain folds in polychlorotrifluoroethylene,” *Journal of Research of the National Bureau of Standards*, vol. 66, p. 13, 1962.
- [30] H. Xiao, Y. Zhang, S. An, and G. Jia, “Investigation on the thermal behaviors and mechanical properties of ultrahigh molecular weight polyethylene (UHMW-PE) fibers,” *Journal of Applied Polymer Science*, vol. 59, no. 6, pp. 931–935, 1997.
- [31] D. A. Skoog and J. J. Leary, *Principles of Instrumental Analysis*, Saunders College Publishing, 6th edition, 2006.
- [32] *Technical Textiles International*, vol. 4, Knitting International, 1996.
- [33] P. Smith and P. J. Lemstra, “Ultra-high-strength polyethylene filaments by solution spinning/drawing,” *Journal of Materials Science*, vol. 15, no. 2, pp. 505–514, 1980.
- [34] W. Hoogsteen, G. T. Brinke, and A. J. Pennings, “DSC experiments on gel-spun polyethylene fibers,” *Colloid and Polymer Science*, vol. 266, no. 11, pp. 1003–1013, 1988.